UC Berkeley

Title

Understanding Propene (Amm)oxidation over Mixed Metal Oxide Catalysts

Permalink

https://escholarship.org/uc/item/4nz8z8k5

Author

Licht, Rachel Blackburn

Publication Date

2016

Peer reviewed|Thesis/dissertation

Understanding Propene (Amm)oxidation over Mixed Metal Oxide Catalysts

By

Rachel Blackburn Licht

A dissertation submitted in partial satisfaction of the

requirements for the degree of

Doctor of Philosophy

in

Chemical Engineering

in the

Graduate Division

of the

University of California, Berkeley

Committee in charge:

Professor Alexis T. Bell, Chair
Professor Enrique Iglesia
Professor Martin P. Head-Gordon

Fall 2016

Understanding Propene (Amm)oxidation over Mixed Metal Oxide Catalysts

by

Rachel Blackburn Licht

Understanding Propene (Amm)oxidation over Mixed Metal Oxide Catalysts

By

Rachel Blackburn Licht

Doctor of Philosophy in Chemical Engineering

University of California, Berkeley

Professor Alexis T. Bell, Chair

Worldwide, approximately 10 billion pounds of acrylonitrile are produced each year by the ammoxidation of propene over multi-phase, multi-component bismuth-molybdate-based catalysts. This ammoxidation process is a six-electron redox reaction requiring co-feeds of ammonia and oxygen to reoxidize the catalyst and release water (stoichiometry $1C_3H_6:1NH_3:1.5O_2$). The mechanism for this reaction is thought to be similar to that of the oxidation of propene to acrolein over the same catalysts, which has been more extensively studied in the literature. However, there are still many open questions regarding the influence of ammonia, the nature of the active site, and the mechanism for acrylonitrile formation. In this work, we investigate the properties of propene ammoxidation over alpha-bismuth molybdate, a single-phase, distorted-scheelite material similar to the active phase in the commercial catalyst.

In Chapter 1, the kinetics of propene ammoxidation over $Bi_2Mo_3O_{12}$ are presented to elucidate product (acrylonitrile, acetonitrile, HCN, acrolein, N_2, etc.) formation pathways. Propene consumption rate is first order in propene and zero order in ammonia (for $NH_3/C_3H_6 = 0-2$) and oxygen (for $O_2/C_3H_6 \geq 1.5$) partial pressures, with an activation energy based on propene consumption ($E_a = 22$ kcal/mol) comparable to that for propene oxidation, suggesting the same rate-limiting step for both reactions. We propose two N-containing species are relevant at ammoxidation conditions: adsorbed NH_3 on surface Bi^{3+} ions that reacts with a propene derivative to form products with C-N bonds, and a few metastable $M-NH_x$ (M=Mo, Bi; x=1, 2) groups that are very sensitive to destruction by water, but that are responsible for NH_3 oxidation to N_2. A proposed reaction mechanism and model that captures the experimental trends in product distribution as a function of partial pressures and temperature is presented.

1

In Chapter 2, the mechanisms and energetics for the propene oxidation and ammoxidation occurring on the (010) surface of $Bi_2Mo_3O_{12}$ were investigated using density functional theory (DFT). An energetically-feasible sequence of elementary steps for propene oxidation to acrolein, propene ammoxidation to acrylonitrile, acetonitrile and HCN, and acrolein ammoxidation to acrylonitrile are proposed. Consistent with experimental findings, the rate limiting step for both propene oxidation and ammoxidation is the initial hydrogen abstraction from the methyl group of propene, which has a calculated apparent activation energy of 27.3 kcal/mol. The allyl species produced in this reaction are stabilized as allyl alkoxide, which can then undergo hydrogen abstraction to form acrolein or react with ammonia adsorbed on under-coordinated surface Bi^{3+} cations to form allylamine. Dehydrogenation of allylamine is shown to produce acrylonitrile, whereas reaction with additional adsorbed ammonia leads to the formation of acetonitrile and hydrogen cyanide. The dehydrogenation of the allyl alkoxide species has a significantly higher activation barrier than the reaction with adsorbed ammonia, consistent with the observation that very little acrolein is produced when ammonia is present. Rapid reoxidation of the catalyst surface to release water is found to be the driving force for reaction, since nearly all reactant conversion steps are endothermic.

In Chapter 3, the propene activation ability of four molybdenum-based mixed metal oxides – $Bi_2Mo_3O_{12}$, $PbMoO_4$, $Bi_2Pb_5Mo_8O_{32}$, and MoO_3 – was investigated using DFT in order to understand the remarkable activity of $Bi_2Mo_3O_{12}$ for selective oxidation and ammoxidation of propene. Propene activation is considered to occur via abstraction of a hydrogen atom from the methyl group of physisorbed propene by lattice oxygen. For each material, the apparent activation energy was estimated by summing the heat of adsorption of propene, the C-H bond dissociation energy, and the hydrogen attachment energy (HAE) for hydrogen addition to lattice oxygen; this sum provides a lower bound for the apparent activation energy. It was found that two structural features of oxide surfaces are essential to achieve low activation barriers: under-coordinated surface cation sites enable strong propene adsorption, and suitable 5- or 6-coordinate geometry at molybdenum result in favorable HAEs. The impact of molybdenum coordination on HAE was elucidated by carrying out a molecular orbital analysis using a cluster model of the molybdate unit. This effort revealed that in 5- and 6-coordinate molybdates, oxygen donor atoms *trans* to molybdenyl oxo atoms destabilize the molybdate prior to H addition but stabilize the molybdate after H addition, thereby providing an HAE ~15 kcal/mol more favorable than on 4-coordinate molybdate oxo atoms. Bi^{3+} cations in $Bi_2Mo_3O_{12}$ thus promote catalytic activity by providing both strong adsorption sites for propene, and by forcing molybdate into 5-coordinate geometries that lead to particularly favorable values of the HAE.

To my father, William Robert Licht,

for his constant inspiration, support and love.

Understanding Propene (Amm)oxidation over Mixed Metal Oxide Catalysts

Table of Contents

Introduction

Approximately one quarter of the most important chemicals used to manufacture industrial products and consumer goods are produced via the heterogeneous selective oxidation of organic molecules.[1] In particular, the partial oxidation of propene to acrolein and the partial ammoxidation of propene to acrylonitrile are each performed on the scale of approximately 10 billion pounds per year.[2,3] The overall stoichiometries of these two related reactions are:

$$CH_2=CH-CH_3 + \frac{1}{2} O_2 \rightarrow CH_2=CH-CHO + H_2O$$

$$CH_2=CH-CH_3 + \frac{3}{2} O_2 + NH_3 \rightarrow CH_2=CH-CN + 3H_2O$$

Approximately 90% of the acrolein produced industrially is actually an intermediate in a sequential two-reactor process to convert propene and oxygen to acrylic acid, which is the basis for acrylic paints, adhesives and coatings. The remaining 10% of produced acrolein is isolated and is mostly converted to D,L-methionine, an important animal feed additive, though some is directly used as a biocide or further reacted to other specialty chemicals (ex. 1,3-propanediol, glutaraldehyde, substituted pyridines). The same reaction with isobutene as the reactant produces methacrolein $CH_2=C(CH_3)-CHO$. Methacrolein is used in the synthesis of a variety of polymers, such as poly methyl methacrylate (PMMA), which is also known as acrylic or Plexiglass.[2]

Acrylonitrile is an important monomer used in the production of a variety of plastics and rubbers. Some of the materials synthesized via co-polymerization of acrylonitrile are Acrylonitrile Butadiene Styrene (ABS) plastic, Styrene Acrylonitrile (SAN) resin, and Nitrile Butadiene Rubber (NBR). Acrylonitrile is also self-polymerized to make polyacrylonitrile, which is the acrylic fiber used in textiles. The small molecule adiponitrile, one of the main components of Nylon, is also synthesized on large scale from acrylonitrile. Additionally, two other important chemicals are co-products of acrylonitrile synthesis: acetonitrile (CH_3-CN), an industrial solvent, and hydrogen cyanide (HCN), used to make alkali cyanide salts and a variety of useful small organic compounds.[3]

Given the commercial importance of all of these molecules, their synthesis has been extensively investigated in industry. In the 1950s, Sohio patented their discovery of a bismuth-molybdenum-based mixed metal oxide capable of performing both propene oxidation and propene ammoxidation with high activity and selectivity.[4] This material has such a high product

yield that it quickly supplanted the previous cuprous oxide catalyst for propene oxidation to acrolein and the acetylene-HCN process for acrylonitrile formation.[5] Over the last 60 years, additional elements have been incorporated to generate multi-component multi-phase mixed metal oxides with improved product yield and lifetime, however bismuth and molybdenum are still the primary components of the catalysts used in industry for the selective oxidation and ammoxidation of propene.[1] For this work, we have focused on a single-phase bismuth molybdate material, α-$Bi_2Mo_3O_{12}$, that is very active for propene (amm)oxidation and that can be easily synthesized.[6] The distorted scheelite crystal structure of $Bi_2Mo_3O_{12}$ is similar to that of a wide variety of other mixed metal oxides, but with some unique features that lead to its remarkable performance for these reactions.

Since the discovery of bismuth molybdate catalysts, researchers have observed that there are many similarities between the propene oxidation and ammoxidation reactions.[7] Specifically, the two reactions are known to have the same initial, rate-limiting propene activation step.[8] Since the overall rate of reaction is governed by this common step, most of the available literature in this field is focused on using the simpler propene oxidation to acrolein reaction as a probe to test the activity of potential new catalyst formulations. In the course of this work, researchers have developed a reasonable understanding of the mechanism for propene oxidation to acrolein, as will be discussed in more detail in the following chapters.

However, the propene ammoxidation reaction remains poorly understood, despite its similar or greater industrial importance and its scientific relevance. When ammonia is co-fed with propene and oxygen, additional products are produced and the formation of the propene oxidation products is suppressed.[9] Therefore, ammonia clearly has a significant influence on the chemistry, however there is no understanding of interaction between ammonia and the hydrocarbon or the catalyst that results in these changes. Specifically, there is essentially no significant information in the literature regarding the mechanisms for propene ammoxidation to acrylonitrile, acetonitrile or hydrogen cyanide. A greater understanding of this propene ammoxidation chemistry not only could allow for further developments in this area, but has potential for broader implications in the area of carbon-nitrogen bond formation chemistry.

The general goal of this work is to understand the propene oxidation and ammoxidation reactions over the α-$Bi_2Mo_3O_{12}$ mixed metal oxide. In the following chapters, we exploit a variety of experimental and quantum chemical modeling techniques in order to address three key questions relevant to this goal: (1) what are the kinetics of propene ammoxidation and how do the reaction conditions affect the distribution of products, (2) what are likely primary mechanisms by which different products are produced during propene ammoxidation, and (3) what is unique about α-$Bi_2Mo_3O_{12}$ that makes it particularly active for propene oxidation and ammoxidation.

In Chapter 1, we present data for the influence of parameters such as reactor temperature, reactant partial pressures, propene conversion, and fraction of added water vapor on the production of over ten individual species observed during propene ammoxidation. We also test the reaction of a number of organic compounds in order to reveal the role of secondary reactions

and test for potential intermediate molecules. From this information, we developed a kinetic model for how all the different products form from the reactant molecules. In particular, we identified a likely step for reaction of ammonia and a hydrocarbon intermediate to form a carbon-nitrogen bond. In doing so, we show that the hypothesized mechanism for propene ammoxidation to acrylonitrile that has been accepted in literature for the past 35 years is unlikely to be the primary route for carbon-nitrogen bond formation.

In Chapter 2, we expand upon our kinetic model by employing density functional theory (DFT) on a 68-atom periodic model of the (010) surface of α-$Bi_2Mo_3O_{12}$ to explore the energetics of potential individual steps for the predominant reactions that occur during propene ammoxidation. To do this, we report calculated energies of over 40 different structures that we propose may be intermediates in the product formation pathways. We also present reaction barrier calculations for three key reaction steps. The combined results lend additional support to the route for carbon-nitrogen bond formation that we propose in Chapter 1. From this work, we also find that the continuous catalyst reoxidation to release water propels the reactions forward, as the hydrogen abstraction steps that convert the reactants to products are almost universally significantly uphill in energy. We note that this is first instance of DFT calculations of this magnitude and scope being reported for the propene ammoxidation reactions.

In Chapter 3, we expand our application of DFT to investigate other mixed metal molybdenum oxides. In this work, we consider only the energetics for the propene activation step, which, as mentioned above, is the rate-limiting step for both propene oxidation and ammoxidation. However, we expand the scope to include surface models of additional molybdenum-based metal oxides in order to understand why seemingly similar materials are significantly less active than bismuth molybdate. We explore the role of crystal geometry, specifically surface molybdenum coordination, on the ability of a catalyst to activate propene with a low energy. From a careful analysis of both the surface models and representative cluster models, which can be used to directly probe the effects of geometry on the individual molecular orbitals, we discover that high energy highly coordinated surface molybdenum atoms generate more active surface sites for propene activation. The role of bismuth is both to force molybdenum into this energetically unfavorable state, and to provide a favorable propene adsorption site near the active molybdate surface sites so that the reaction can occur.

Overall, this work adds significant new insights to the field of partial (amm)oxidation catalysis in general and to propene ammoxidation over bismuth molybdate in particular. From the findings discussed in Chapter 1 from experimental observations and further expanded in Chapter 2 from DFT calculations, we propose new mechanisms for the reactions of propene ammoxidation, specifically with regards to the key interaction between ammonia and a hydrocarbon to form a C-N bond. These findings may lead to new developments in the field of carbon-nitrogen chemistry. Additionally, our exploration the key characteristics of an active molybdate material for propene activation in Chapter 3 may guide the development of new catalysts for related reactions.

Acknowledgements

Chapter 1

The Mechanism and Kinetics of Propene Ammoxidation over α-Bismuth Molybdate[0]

1. Introduction

Bismuth molybdate-based catalysts have been used extensively since their discovery in the 1950s by Sohio to perform important oxidation and ammoxidation reactions of light olefins[1]. The most industrially-relevant of these processes is the ammoxidation of propene to acrylonitrile, which had a worldwide demand of over 10 billion pounds per year in 2012[2]. Almost half of the acrylonitrile produced is used to make acrylic fibers for textiles, with the rest either polymerized to make plastics or further reacted to small molecules such as acrylamide or adiponitrile. Two commercially-important byproducts are also produced and recovered from propene ammoxidation, namely acetonitrile and hydrogen cyanide (HCN). Since the primary product desired from propene ammoxidation is acrylonitrile, catalyst development efforts have led to a steady rise in acrylonitrile yield from ~55% for bismuth molybdate to >80% for current industrial catalysts that contain approximately ten metal elements, including bismuth and molybdenum[3].

Given the importance of propene ammoxidation, considerable effort has been devoted to understanding this reaction and the related oxidation of propene to acrolein. Much of this work has been conducted with the distorted scheelite α-$Bi_2Mo_3O_{12}$ phase[4] because of its good catalytic activity and its structural similarity to ternary metal oxides such as $Bi_{1-x/3}V_{1-x}Mo_xO_4$, $Bi_3FeMo_2O_{12}$, $Bi_2Mo_{2.5}W_{0.5}O_{12}$ and $Bi_{2-x}Ce_xMo_3O_{12}$ that have been reported to have higher catalytic activity[5,6,7]. Research has shown that both Bi and Mo are needed to catalyze these reactions; for example, MoO_3 will not react propene, but will form acrolein or acrylonitrile from allyl radicals generated *in situ*[8,9]. By contrast, Bi_2O_3 will slowly activate propene, but will only form hexadiene[10]. Since the initial steps of propene ammoxidation are thought to be similar to those of propene oxidation to acrolein, and acrolein is also observed during propene ammoxidation, it is useful to first summarize what is known about propene oxidation over bismuth molybdate.

Studies of propene oxidation over bismuth molybdate using deuterated propene reveal that the rate-limiting step is hydrogen abstraction from the methyl group of propene[11,12]. Historically, this step has been thought to occur on an oxygen atom associated with bismuth[13,14,15]. However, our recent theoretical work comparing the reaction barriers for hydrogen abstraction from propene by the different oxygen atoms on the (010) surface of $Bi_2Mo_3O_{12}$ shows that molybdenyl oxygen perturbed by a neighboring bismuth atom is the most likely site for propene activation[16]. Further experiments with isotopically-labeled carbon demonstrate that this first step generates a physisorbed, symmetric allyl[17,18], most likely with radical character[19]. $^{18}O_2$ labeling studies have shown that the O in the product acrolein comes from the catalyst surface via a Mars-van Krevelen mechanism[20,21]. It has been hypothesized that acrolein is formed by addition of the allyl radical to a surface molybdenyl oxo (Mo=O) group to form a Mo-bound allyl alkoxide, which then undergoes hydrogen abstraction to produce acrolein[22]. The catalytic cycle is closed when surface hydrogen atoms are released as water during reoxidation by gas phase oxygen. Molecular O_2 is not directly involved in the formation of acrolein and that propene oxidation can occur for a period of time in the absence of gas-phase O_2 by reaction of propene with surface oxygen atoms, which are replaced by oxygen atom diffusion from the bulk[11,23].

The steady-state kinetics of propene oxidation, measured in the presence of at least a stoichiometric pressure of oxygen, are reported to be first order in propene and zero order in oxygen. Acrolein formation is generally observed to have an activation energy of ~20 kcal/mol, though values between 17 and 31 kcal/mol have been reported[5,21,24,25,26]. The primary byproducts of propene oxidation are CO, CO_2, and acetaldehyde, though trace amounts of acetic acid, acetone, acrylic acid and ethene have also been observed.

Propene ammoxidation to acrylonitrile (CH_3-CH=CH_2 + NH_3 + $^3/_2 O_2$ → CH_2=CH-CN + $3H_2O$) is a more complex reaction than propene oxidation (CH_3-CH=CH_2 + O_2 → CH_2=CH-CHO + H_2O), and is accompanied by the formation of acetonitrile, hydrogen cyanide, propionitrile and N_2, in addition to CO_x, acrolein and H_2O. Nevertheless, several features of these two reactions are similar. First of all, the apparent activation energy for acrylonitrile formation is the same as for acrolein formation (~20 kcal/mol), as are the partial pressure dependencies (first order in propene pressure and zero order in oxygen and ammonia, as long as ammonia and oxygen are supplied in at least stoichiometric quantities)[27,28,29]. Second, kinetic isotope effect experiments indicate that the rate-limiting step for propene ammoxidation also involves the initial abstraction of a hydrogen atom from the methyl group of propene[30]. These observations suggest that propene activation occurs at the same catalyst surface site for both reactions. Third, in the absence of gas-phase oxygen, the catalyst will temporarily convert propene to acrylonitrile if ammonia is present, indicating that, again, activation of propene and subsequent hydrogen removal steps involve oxygen atoms that are part of the catalyst structure[31,32].

Details of the mechanism of propene ammoxidation after the initial activation of propene activation are poorly understood. In particular, the mechanism by which the acrylonitrile C-N

bond is formed remains a topic of speculation. Interestingly, it has been observed that there is very little C-O bond formation to make acrolein when ammonia is fed, despite all other conditions being favorable for propene oxidation[27,28]. While the reaction of acrolein and ammonia to form acrylonitrile is extremely facile (E_a = ~7 kcal/mol), multiple researchers have concluded from experiments at short contact times that most of the acrylonitrile is not produced from free acrolein[27,28]. Therefore, the direct reaction of propene to acrylonitrile must be favored kinetically, as well as thermodynamically, over the reaction of propene to acrolein.

The most prevalent hypothesis for C-N bond formation involves reaction of allyl species with surface Mo=NH groups, followed by three hydrogen abstractions of the resulting surface species. This mechanism, proposed by Burrington et $al.$[14], is tempting because it parallels the mechanism generally accepted for propene oxidation in which allyl reacts with Mo=O to produce acrolein (see above). These authors also observed that the ratio of acrylonitrile to acrolein for conditions where NH_3/C_3H_6 < 1 increases linearly with $(NH_3)^2/C_3H_6$ for most reaction conditions[33]. From this, they concluded that a surface NH=Mo=NH species, which requires 2 NH_3 molecules to form, is the primary C-N bond formation site. However, no experimental evidence for Mo=NH groups on the surface of $Bi_2Mo_3O_{12}$ has been reported in the literature.

Recent DFT calculations carried out on MoO_2Cl_2 clusters show that the Gibbs free energy of reaction at 673 K of O=Mo^{6+}=O species and NH_3 to produce H_2O and O=Mo^{6+}=NH species is +12.4 kcal/mol, and that the formation of HN=Mo^{6+}=NH species is even more energy intensive (+27.8 kcal/mol from the fully oxidized site)[34]. These very unfavorable thermodynamics for formation of Mo=NH groups suggests that in the presence of water, produced as a byproduct of propene ammoxidation (> 3 mol H_2O produced / mol C_3H_6 consumed), the surface concentration of Mo=NH groups should be very small. The instability of Mo^{6+}=NR groups in organometallic complexes to hydrolytic decomposition in air at room temperature has also been reported[35,36,37]. Additional theoretical calculations of the transition state enthalpy change for the reaction of an allyl species with a Mo_3O_9 cluster to produce bound acrolein is +10.9 kcal/mol, and the transition state enthalpy change for the reaction of allyl species with a Mo_3O_8NH cluster to produce bound acrylonitrile is very similar at +11.4 kcal/mol[39]. Together, this evidence suggests that the surface concentration of Mo=NH groups relative to Mo=O groups on the surface of $Bi_2Mo_3O_{12}$ should be quite low, and therefore the former groups are unlikely to be responsible for the observed high selectivity to acrylonitrile during propene ammoxidation.

Several alternatives to Mo=NH groups have been investigated as possibly catalytically-relevant species. Wragg et $al.$[28] found no experimental evidence to support involvement of NO or N_2O intermediates during propene ammoxidation. In an investigation of NH_3 adsorption and decomposition over Bi_2MoO_6, Matsuura observed two modes of adsorption: a weak σ-bonding interaction with a metal cation (ΔH_{ads} = -6.2 kcal/mol) and a strong chemisorption (ΔH_{ads} = -24 kcal/mol)[40]. He proposed that the latter mode of adsorption would result in the formation of Bi=NH groups that might combine to form N_2 (E_a = 37 kcal/mol) or react with coordinated allyl species to form acrylonitrile.

The aim of the present study is to explore the mechanism and kinetics of propene ammoxidation, with the particular goal of shedding new light on the processes involved in the formation of the C-N bond in acrylonitrile and in the nitrogen-containing byproducts (acetonitrile and HCN). A further aim was to identify the extent to which acrolein, the product of propene oxidation, and allylamine might act as intermediates to acrylonitrile. It will be shown that the results of this investigation provide new insights into all of the propene ammoxidation reaction pathways and the factors affecting the utilization of ammonia to form products containing –CN groups instead of N_2. Our work also leads to a comprehensive model for the kinetics of propene ammoxidation over $Bi_2Mo_3O_{12}$ that properly simulates the effects of reactant and product partial pressures and temperature.

2. Experimental and theoretical methods

2.1 Catalyst preparation and characterization

$Bi_2Mo_3O_{12}$ was prepared by the method of complexation with citric acid, which produces a solid product with a more uniform distribution of metal atoms and a higher surface area than can be achieved by the method of co-precipitation[41]. Ammonium molybdate tetrahydrate, $(NH_4)_6Mo_7O_{24} \cdot 4H_2O$, (99.98% from Sigma-Aldrich) was dissolved in 0.3M citric acid solution with the ratio 1 citrate: 1 Mo. Bismuth(III) nitrate pentahydrate, $Bi(NO_3)_3 \cdot 5H_2O$, (99.98% from Sigma-Aldrich) was dissolved in a solution of 2M HNO_3 and 0.2M citric acid with the ratio 1 citrate: 1 Bi. The Mo solution was added slowly to the Bi solution and the resultant mixture was boiled while stirring to remove most of the water. The concentrated solution was dried overnight in air at 333 K to produce a foam, then calcined in air at 873 K for 6 h. The as-prepared catalyst was analyzed by powder XRD to confirm the distorted scheelite crystal structure as reported in literature[42]. The surface area of the catalysts was determined to be approximately 1 m^2/g from the BET isotherm measured by N_2 adsorption at its boiling point.

2.2 Catalyst performance

Measurements of reaction rates were performed in a packed-bed quartz tubular reactor with 10-mm diameter. $Bi_2Mo_3O_{12}$ powder was physically mixed with fumed silica and loaded into the reactor, with a thermocouple placed at the center of the catalyst bed. The catalyst was heated to reaction temperature (603-753 K) at 3 K/min under a 20 mL/min flow rate of 20% oxygen diluted in helium, and left overnight at these conditions. All reactions were carried out at atmospheric pressure with 0-12% propene (Praxair), 0-22% ammonia (Praxair), 8-19% oxygen (20% in helium, Praxair) and balance helium (Praxair). Gas flow rates were controlled by Bronkhorst Mass Flow Controllers (MFCs). A reactor loaded with only fumed silica and treated in the same way as the catalyst did not produce significant quantities of any product, and changing the ratio of diluent to catalyst did not affect the active-surface-area-scaled rates.

Catalyst loading, reactant partial pressures, and total space velocity were chosen to maintain propene conversion <5% so that intrinsic kinetics could be measured under conditions of differential conversion. The catalyst was always stabilized for at least 2 days under ammoxidation conditions (693 K, 7.6 kPa C_3H_6, 7.9 kPa NH_3, 15.6 kPa O_2) before performing measurements of the reaction kinetics.

Products were analyzed by an Agilent 6890 Gas Chromatograph (GC) equipped with a 30-m HP-PLOT Q column attached to a flame ionization detector (FID) and an Alltech Hayesep DB packed column attached to a thermal conductivity detector (TCD). Acetaldehyde, acetone, acetonitrile, acrolein, acrylonitrile, ammonia, ethene, hydrogen cyanide (HCN), propene and propionitrile were analyzed on the FID, while carbon dioxide, carbon monoxide, nitrogen, nitrous oxide and oxygen were analyzed on the TCD. Details of how the GC was calibrated are given in Appendix !. Except for the selectivity versus conversion plot, all reported data points are averages of more than three sample injections in the GC. The lines downstream of the reactor were maintained at ~390 K to prevent water condensation and resulting product polymerization before being introduced to the GC.

Since the reactor was operated under differential conversion conditions, propene conversion was calculated on the basis of products formed by dividing the moles of carbon in all the products by the moles of carbon in the propene reactant feed. Carbon product selectivities were scaled based on the number of carbon atoms in each species according to Eqn. 1.1, where a_i is the number of carbon atoms in product i and n_i is the number of moles of product i.

$$C\ Selectivity_i(\%) = \frac{a_i n_i}{\sum_i a_i n_i} * 100 \tag{1.1}$$

Ammonia conversion was similarly calculated by dividing the moles of nitrogen in all the products by the moles of nitrogen in the ammonia reactant feed. Nitrogen product selectivities were calculated based on the number of nitrogen atoms in each species according to Eqn. 1.2, where b_i is the number of nitrogen atoms in product i.

$$N\ Selectivity_i(\%) = \frac{b_i n_i}{\sum_i b_i n_i} * 100 \tag{1.2}$$

For experiments in which a liquid feed was used, the desired compound was loaded into a syringe and added to the gas feed mixture via syringe pump set at a constant volumetric flow rate. The combined feed with the vaporized compound was then sent to the reactor and analyzed in the same way described above. In the case of acrolein, this compound was diluted 1:1 in hexane in order to prevent acrolein polymerization in the syringe needle. Hexane was verified to not affect the rate of reaction.

2.3 Theoretical calculations

Quantum chemical calculations were performed using density functional theory (DFT) in the Q-Chem program. The 6-31G* basis set was used for geometry optimizations and the triple zeta 6-311G++G(3df,3pd) basis set for the final energies, both in conjunction with the ωB97X-D exchange-correlation functional to model all gas phase species. Bond Dissociation Energies (BDEs) were calculated by subtracting the energy of the optimized parent structure from the sum of the energies of each of the two separately optimized structure fragments resulting from breaking the desired bond. Enthalpy and entropy corrections for the gas phase reaction energies were calculated at 673 K and 1 atm using the 6-31G* basis set and the ωB97X-D exchange-correlation functional.

For the $(O=Mo=O)_2Bi_2O_{10}H_{10}$ model of the proposed active site, the Def2-SVP (Bi & Mo) basis set and effective core potential plus the 6-31G* (O, N, & H) basis set were used for geometry optimizations, and the Def2-TZVPD (Bi & Mo) plus the 6-311++G(3df, 3pd) (O, N, & H) for the final energies, both in conjunction with the B97-D exchange-correlation functional. The parameters for Bi & Mo were obtained from the EMSL basis set exchange. The enthalpy and entropy corrections were calculated using the Grimme Rigid Rotor Harmonic Oscillator method[43] at 673 K and 1 atm. The entropy loss upon adsorption was calculated with the assumptions of De Moor *et al.* [44] that weakly adsorbed molecules can still rotate in 3-D and translate in 2-D. The $(O=Mo=O)_2Bi_2O_{10}H_{10}$ active site model was built using the optimized (010) surface of $Bi_2Mo_3O_{12}$ as a reference[45]. See Appendix A for more calculation details about the $(O=Mo=O)_2Bi_2O_{10}H_{10}$ model.

3. Results

3.1 Reaction kinetics

3.1.1 Propene and ammonia consumption

Figure 1.1 shows the dependence of the rate of propene consumption on the partial pressures of propene, ammonia and oxygen at low conversion. The rate of propene consumption is first-order in propene pressure, whether or not ammonia is present. For O_2 pressures above stoichiometric ratios ($O_2/C_3H_6 > 1.5$, vertical dashed line in Fig. 1.1), the rate of propene consumption is zero order in oxygen. This is consistent with the Mars-van Krevelen mechanism proposed in the literature[21] in which propene is activated by the catalyst in a reaction that is significantly slower than the catalyst re-oxidation by gas phase oxygen. However, for a fixed propene pressure, as the oxygen pressure decreases below approximately stoichiometric ($O_2/C_3H_6 = 1.5$), the rate of propene consumption begins to decrease. Therefore, at low oxygen pressures, the rate of catalyst re-oxidation by gas phase oxygen becomes comparable to the rate of catalyst reduction. Figure 1.1 also shows that, for a catalyst that has previously been stabilized

in ammoxidation conditions, the rate of propene consumption is independent of ammonia pressure across the range of NH_3/C_3H_6 ratios from 0 to 2. The reactant pressure dependencies reported here for propene consumption are consistent with those reported earlier for acrylonitrile formation[27,28]. For an O_2/C_3H_6 ratio greater than or equal to 1.5, this leads to the following rate expression (Eqn. 1.3) for the consumption of propene.

$$-r_{C_3H_6} = k_{RLS}P_{C3H6} \qquad (3)$$

Fig. 1.1. Dependence of the rate of propene consumption on reactant feed partial pressures for reaction at 673 K. Total propene conversion 0.8%±0.1%. (a) Dependence on P_{C3H6} for $P_{O2} = 16.3$ kPa and $P_{NH3} = 0$ kPa (open symbol) or 7.4 kPa (filled symbol). (b) Dependence on P_{O2} for $P_{C3H6} = 8.0$ kPa and $P_{NH3} = 7.4$ kPa. Vertical dashed line indicates the oxygen pressure where $O_2/C_3H_6 = 1.5$. (c) Dependence on P_{NH3} for $P_{C3H6} = 8.0$ kPa and $P_{O2} = 16.3$ kPa. Curves are to guide the eye.

The dependence of ammonia consumption rate on reactant partial pressures is displayed in Figure 1.2. We observe a slightly negative order dependence on propene pressure, a zero-order dependence on oxygen pressure (except at very low O_2 pressures), and a positive fractional order dependence on ammonia pressure. It is also notable that the rate of ammonia consumption is about an order of magnitude higher than the rate of propene consumption at each reaction condition. Therefore, as can be seen from the left-hand ordinate of Figure 1.3, the ammonia conversion is substantial and variable across the range of ammonia pressures under conditions where propene conversion is always less than 1%. Figure 1.3 also shows the variation of the calculated outlet water pressure with the pressure of ammonia in the feed. Since H_2O pressure cannot be directly measured in our system, the outlet H_2O pressure is calculated by assuming that the reactor is at steady-state and all hydrogen atoms removed from propene or ammonia to produce products leaves as water (i.e. by stoichiometry, three water molecules are produced simultaneously with each acrylonitrile molecule produced). Clearly, the outlet water pressure

also varies significantly with the feed conditions. The effects of water pressure on product formation rates will be discussed in more detail in Section 3.1.3.
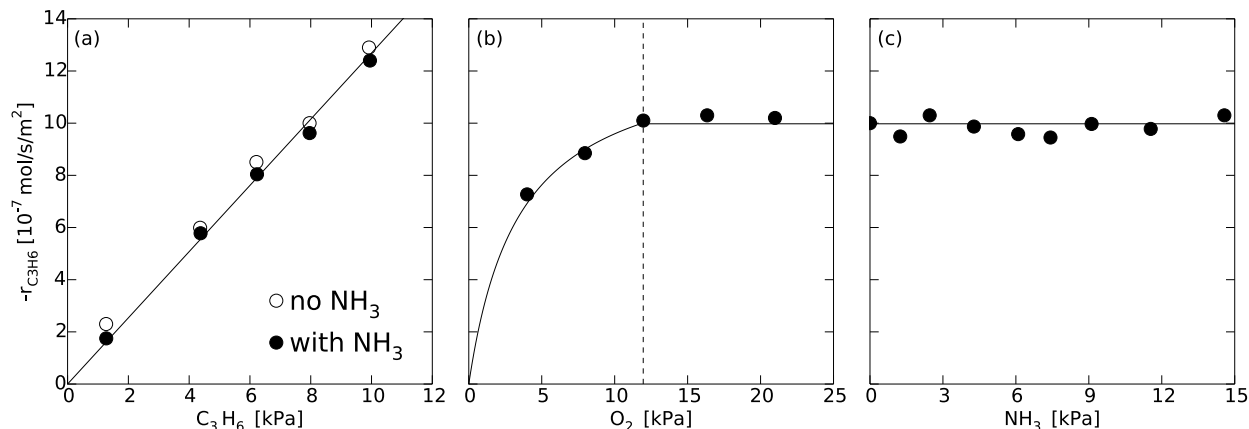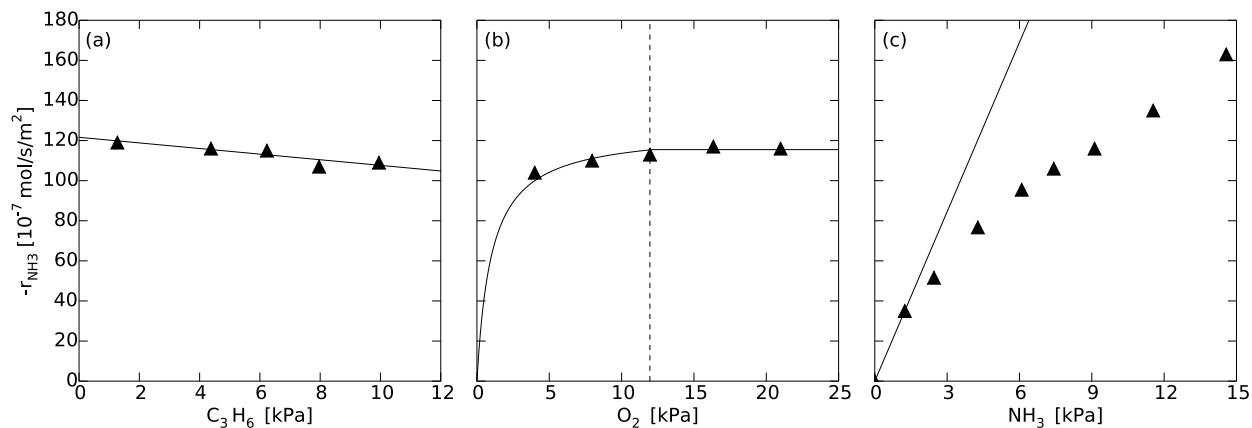

Fig. 1.2. Dependence of the rate of ammonia consumption on reactant feed partial pressures for reaction at 673 K. Total propene conversion 0.8%±0.1%. (a) Dependence on P_{C3H6} for P_{O2} = 16.3 kPa and P_{NH3} = 7.4 kPa. (b) Dependence on P_{O2} for P_{C3H6} = 8.0 kPa and P_{NH3} = 7.4 kPa. Vertical dashed line indicates the oxygen pressure where O_2/C_3H_6 = 1.5. (c) Dependence on P_{NH3} for P_{C3H6} = 8.0 kPa and P_{O2} = 16.3 kPa. Curves are to guide the eye.
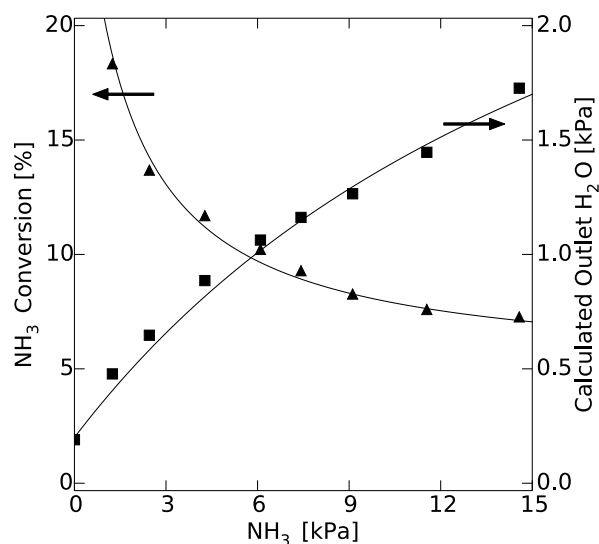
Fig. 1.3. The dependence of ammonia conversion (left axis, ▲) and calculated outlet water pressure (right axis, ■) on the inlet ammonia pressure at 673 K. P_{C3H6} = 8.0 kPa, P_{O2} = 16.3 kPa and total propene conversion 0.8%±0.1%. Curves are to guide the eye.

8

3.1.2 Carbon and nitrogen selectivities

Twelve carbon-containing products were observed during propene ammoxidation and their relative selectivities vary with reactor conditions, as will be discussed in this section. We have chosen to group these products into four general categories (see Table 1.1) based on similar response to the addition of NH_3. Figure 1.4 displays C selectivity versus NH_3 pressure for only those species that have <20% C selectivity at all NH_3 pressures in order to emphasize these minor products and justify the category groupings we have made. Figure 1.5 displays the response of the four product categories to NH_3 pressure. The first category, designated as acrylonitrile or ACN, is the sum of the primary ammoxidation product acrylonitrile and a small amount of propionitrile. As seen in Figure 1.4, propionitrile is produced with the approximately constant carbon selectivity of only ~2.5% at all conditions with nonzero NH_3. Because of its minor importance, its structural similarity to acrylonitrile, and its similar response to NH_3 pressure, we group these two products together. The second category, designated as acrolein or ACO, consists of the primary oxidation product, acrolein. The third category, designated as nitrogen-containing byproducts or NBP, consists of the sum on a C-atom basis of two major ammoxidation byproducts: hydrogen cyanide (HCN) and acetonitrile. The data in Figure 1.4 show that the carbon selectivities to each of these two products have parallel responses to ammonia pressure. Additionally, they are always produced in the constant ratio of approximately 5 HCN: 2 acetonitrile, allowing us to group them together. The fourth category, designated as oxygen-containing byproducts or OBP, consists of the carbon-scaled sum of all carbon byproducts that do not contain nitrogen. More than 50% of this group is CO_2, with the remainder consisting of CO, acetaldehyde, and trace amounts of acetic acid, acetone, acrylic acid, and ethene. As seen in Figure 1.4, the selectivity to each of these products decreases by over 50% upon ammonia addition and together only add up to <10% selectivity when NH_3/C_3H_6 =1. Therefore, we group these byproducts together.

Product Category Name	Abbreviation	Included Compounds
Acrylonitrile	ACN	Acrylonitrile and Propionitrile
Acrolein	ACO	Acrolein
Nitrogen-Containing Byproducts	NBP	Hydrogen Cyanide and Acetonitrile
Oxygen-Containing Byproducts	OBP	Carbon Dioxide, Carbon Monoxide, Acetaldehyde, Acetic Acid, Ethene, Acrylic Acid and Acetone
Nitrogen	N2	Nitrogen and Nitrous Oxide

Table 1.1. Categorization of propene ammoxidation products. The right-hand column lists products in order of decreasing selectivity.
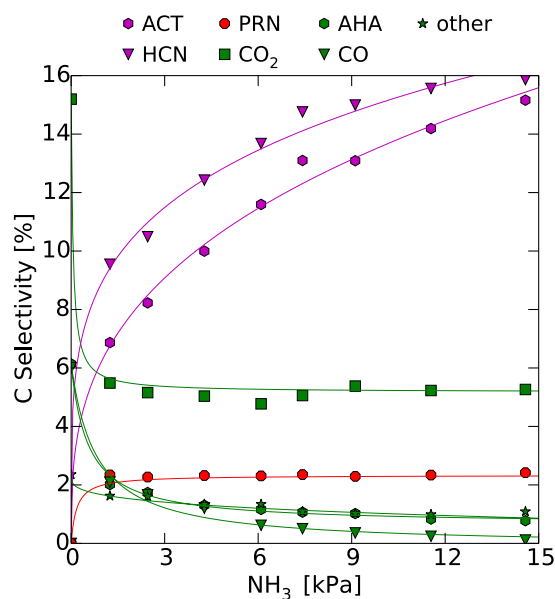

Fig. 1.4. Dependence of carbon-scaled byproduct selectivities on inlet ammonia pressure at 673 K. P_{C3H6} = 8.0 kPa, P_{O2} = 16.3 kPa, and total propene conversion 0.8%±0.1%. ACT = acetonitrile, PRN = propionitrile, AHA = acetaldehyde, Other = ethene + acetic acid + acetone. Curves are to guide the eye.

Figure 1.5 (a) displays the carbon selectivities to these four product groups versus inlet ammonia pressure at low propene conversion. Even at the lowest experimentally attainable ammonia pressure, acrylonitrile (ACN) becomes the primary product with a nearly constant selectivity of ~ 60% across the entire range of non-zero ammonia pressures. The nitrogen-containing byproducts account for the majority of the remaining converted carbon. The selectivity to NBP increases monotonically with ammonia pressure, in contrast to the selectivity to ACN which plateaus at low ammonia pressures and then decreases slightly at very high ammonia pressures. Figure 1.5 (a) shows that only ~10% of the converted propene ends up in species that do not contain nitrogen, with the majority going to CO_2 when at least stoichiometric ammonia is present in the feed. When no ammonia is present, the observed selectivity to the oxidation product acrolein is ~70%, however, as soon as ammonia is introduced, very little acrolein is observed in the reaction products, consistent with previous reports[27, 28].

Fig. 1.5. Dependencies of (a) carbon-scaled product selectivities and (b) nitrogen-scaled product selectivities on inlet ammonia pressure at 673 K. P_{C3H6} = 8.0 kPa, P_{O2} = 16.3 kPa, and total propene conversion 0.8%±0.1%. Symbols are data points; lines are calculated from the reaction network model.

Figure 1.6 (a) displays the carbon selectivities to the four product groups versus inlet oxygen pressure. Oxygen pressure does not have as pronounced an effect on the carbon selectivities as the ammonia pressure, although we observe a decrease in the ACN and an increase in NBP selectivities with increasing oxygen pressure. A plot of the natural log of the NBP rate versus the natural log of the oxygen pressure has a slope of 0.4, indicating the existence of a reaction between a hydrocarbon intermediate and one O-atom from O_2 to form the nitrogen-containing byproducts. A similar effect was observed for propene oxidation over

11

bismuth molybdate, for which higher pressures of oxygen resulted in a lower selectivity to acrolein and a higher selectivity to the combustion products[26]. Propene pressure had no observable effect on the product distribution.

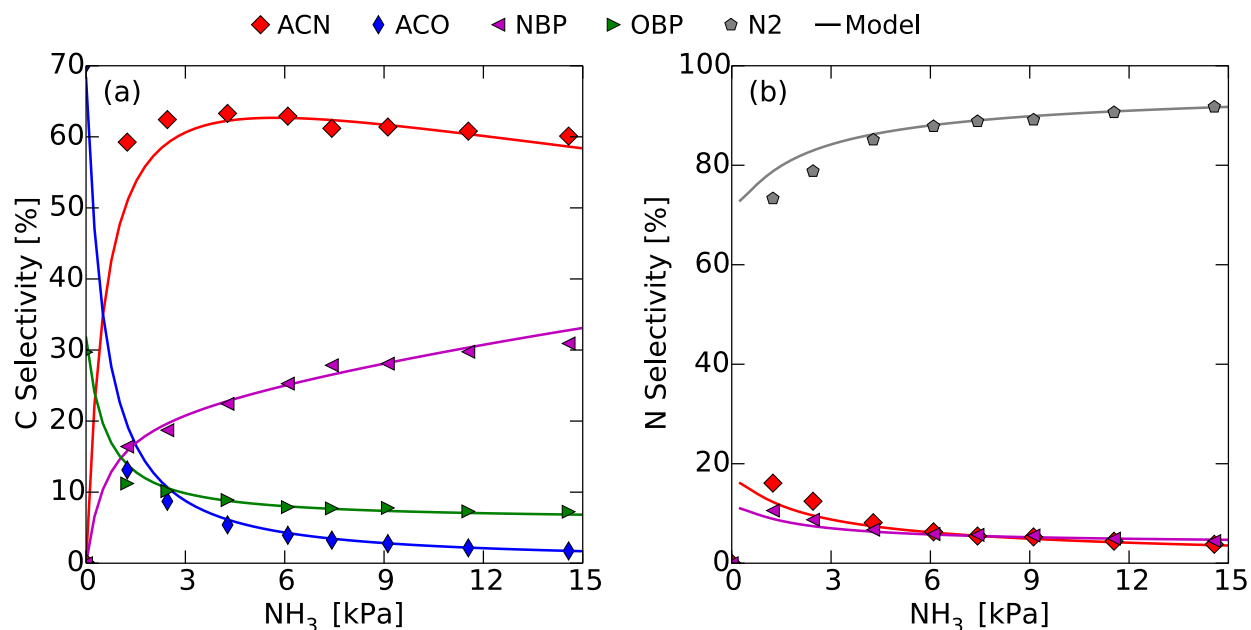Fig. 1.6. Dependence of (a) carbon-scaled product selectivities and (b) nitrogen-scaled product selectivities on inlet oxygen pressure at 673 K. P_{C3H6} = 8.0 kPa, P_{NH3} = 7.4 kPa, and total propene conversion 0.8%±0.1%. Symbols are data points; lines are calculated from the reaction network model.

We also group the nitrogen-containing products into three categories. Again, acrylonitrile (ACN) is the sum of acrylonitrile and trace amounts of propionitrile. As above, the nitrogen-containing byproducts (NBP) group consists of the sum on an N-atom basis of hydrogen cyanide and acetonitrile. The final category, nitrogen (N2), consists of the sum on an N-atom basis of molecular nitrogen and trace amount of nitrous oxide (< 3% N-selectivity).

Figure 1.5 (b) displays the nitrogen selectivities to the three nitrogen product groups as a function of ammonia pressure. The predominant product is N_2 (> 70% N-selectivity at all conditions), which is formed by ammonia oxidation (2 NH_3 + 1.5 O_2 → N_2 + 3 H_2O). The formation of products with –CN bonds (ACN and NBP) accounts for less than 20% of the converted ammonia at stoichiometric conditions (1NH_3:1C_3H_6) and <1% propene conversion. The presence of excess ammonia results in combustion of ammonia to nitrogen, rather than increasing the formation of the desired –CN products. There is little effect of oxygen pressure on the nitrogen selectivities, as observed in Fig. 1.6 (b).

3.1.3 Effect of water on product formation

The only product we have not yet discussed is water, which is produced in significantly higher concentrations than any of the products discussed in Section 3.1.2. In order to balance the stoichiometry at steady state, at least one molecule of water is produced in conjunction with each molecule of carbon- or nitrogen-containing product. Because of this, the concentration of water changes significantly throughout the reactor bed and with changing conditions (see Figure 1.3), even when the propene conversion is very low. To explore the influence of water on the reaction rates and selectivities, water vapor was added to the reactor feed. From Fig. 1.7, it is clear that the addition of water suppresses the rate of ammonia consumption significantly, while having a negligible effect on the rate of propene consumption. When 4.4 kPa of water is added to the feed, the rate of ammonia consumption was about 10-fold lower than in the absence of added water. This effect is attributed to suppression of the rate of ammonia oxidation to nitrogen, since the selectivity to this product is ~90% at these conditions without the addition of water. Additionally, by feeding 10.5 kPa H_2O, we were able to completely suppress the formation of N_2. Fig. 1.8 displays the carbon (a) and nitrogen (b) selectivities as a function of the pressure of water in the feed. For the carbon-containing products, we observe a significant increase in the selectivity to acrolein, from 6% to 15%. There is a commensurate decrease in the selectivities to both ACN and NBP, though the selectivity to ACN remains ~60%. For the nitrogen-containing products, we observe a substantial decrease in the N2 selectivity to values significantly lower than those observed when only changing ammonia pressure.
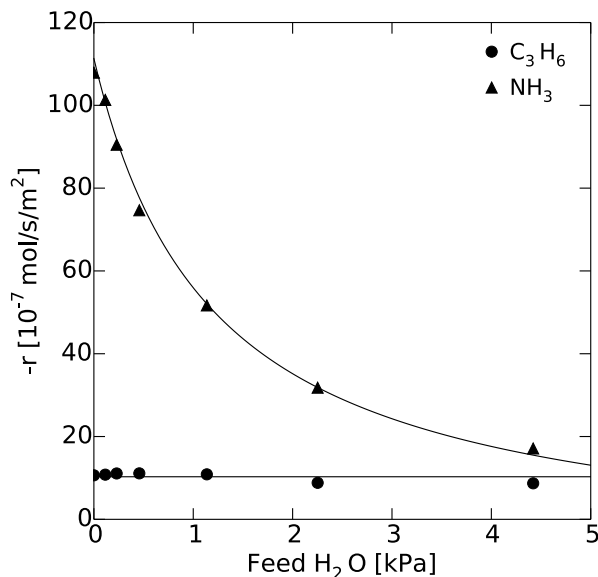
Fig. 1.7. Dependence of propene and ammonia consumption rates on feed water pressure. 673 K, P_{C3H6} = 8.2 kPa, P_{NH3} = 8.2 kPa, and P_{O2} = 16.4 kPa. Total propene conversion 0.7%±0.1%. Lines are to guide the eye.
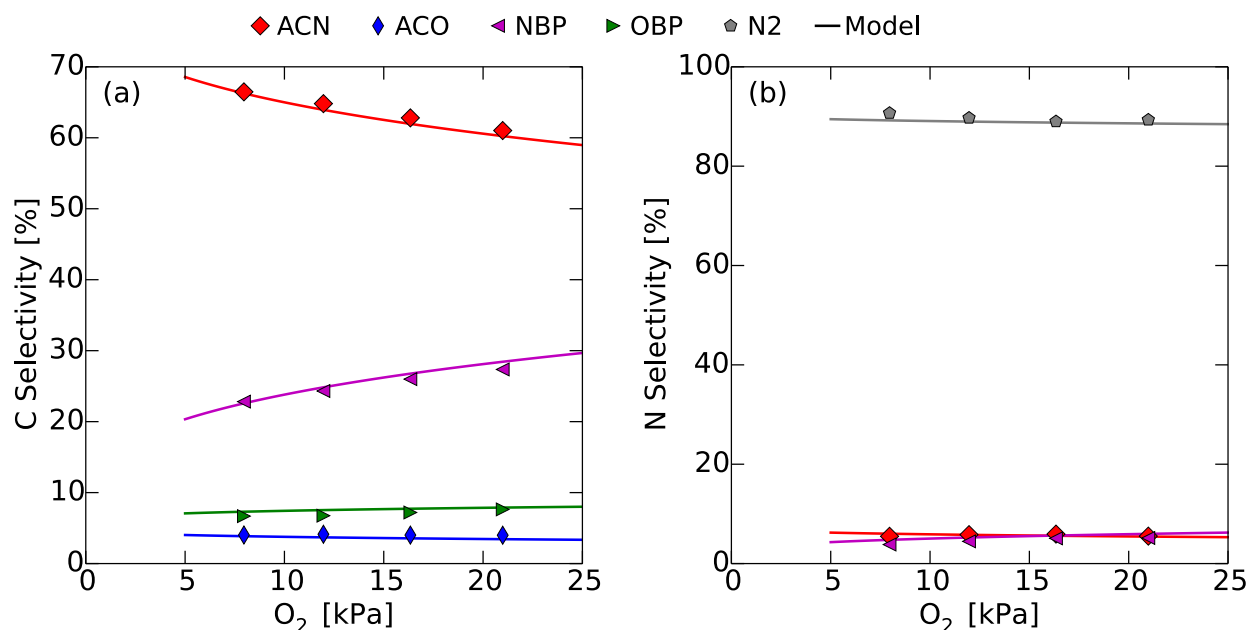
Fig. 1.8. Dependence of (a) carbon-scaled product selectivities and (b) nitrogen-scaled product selectivities on feed water pressure. 673 K, P_{C3H6} = 8.2 kPa, P_{NH3} = 8.2 kPa, and P_{O2} = 16.4 kPa. Total propene conversion 0.7%±0.1%. Symbols are data points; curves are calculated from the reaction network model.

A comparison of the effects of water on steady-state rates of propene consumption for propene oxidation and ammoxidation is reported in Table 1.2. For propene oxidation over a fresh catalyst (base case used for normalization), the propene consumption rate is not affected by the presence of water (lines 1 and 2). However, if the catalyst is first treated with NH_3 and O_2, the propene consumption rate during propene oxidation increases by a factor of 1.6 over that on a fresh catalyst (line 3). However, if the NH_3-treated catalyst is subsequently exposed to a high pressure of water plus O_2, the rate of propene consumption returns to its base case value (line 4). Regardless of the catalyst pretreatment, the selectivity to ACO during propene oxidation is always ~70%. Exposure of a fresh catalyst to ammoxidation conditions causes the propene consumption rate to slowly increase over a period of ~8 h until it reaches a rate that is 1.6 times higher than that of propene oxidation on a fresh catalyst (line 5). Upon cessation of the NH_3 flow, the rate of propene consumption at low conversion remained constant at this higher value for a period of at least 24 h. However, treating the catalyst with a high pressure of water eliminates this rate enhancement (line 6). In both cases when NH_3 is present in the reactor feed (lines 5 and 6), the selectivity to ACN is ~60%. These results suggest that treatment of $Bi_2Mo_3O_{12}$ with NH_3 causes a change in the surface composition or the number of active sites exposed, leading to a ~1.6x increase in propene activation activity. However, this activity increase can be undone by exposure to high concentrations of water vapor, and is therefore likely only relevant at low propene conversions.

14

Reactor Feed	Catalyst Pretreatment	Normalized S.S. $-r_{C3H6}$
$C_3H_6 + O_2$	(none)	1.00
$C_3H_6 + O_2 + H_2O$	(none)	1.02
$C_3H_6 + O_2$	NH_3	1.59
$C_3H_6 + O_2 + H_2O$	(1) NH_3; (2) H_2O	0.97
$C_3H_6 + O_2 + NH_3$	NH_3	1.63
$C_3H_6 + O_2 + NH_3 + H_2O$	(1) NH_3; (2) H_2O	0.92

Table 1.2. Normalized steady-state rate of propene consumption as a function of the reactor feed and of the catalyst pretreatment. Reactor feed as indicated in the table, with $P_{C3H6} = 8.0$ kPa, $P_{NH3} = 8.0$ kPa, $P_{O2} = 16.0$ kPa, and $P_{H2O} = 10.5$ kPa. A (none) pretreatment indicates freshly calcined catalyst. NH_3 pretreatment involves exposure to $P_{NH3} = 8.0$ kPa and $P_{O2} = 16.0$ kPa for 24 hours; a H_2O pre-treatment is exposure to $P_{H2O} = 10.5$ kPa and $P_{O2} = 16.0$ kPa for 12 hours. The reported normalized rate of propene consumption is measured after the rate has reached a steady-state level for the specified reactor feed.

3.2 Secondary reactions

3.2.1 Selectivity versus conversion

To distinguish whether the products of propene ammoxidation are formed via primary reactions or secondary reactions of the primary products, we examined how the C-selectivities depend on propene conversion. Propene conversion was changed by varying the total molar flow rate, while maintaining constant feed partial pressures. Figure 1.9 shows that, for very low propene conversion (<0.7%), there is a higher selectivity to acrolein and lower selectivity to acrylonitrile than observed at higher conversions. The selectivities to the nitrogen- and oxygen-containing byproducts remained essentially constant with conversion. The change in selectivity with conversion was larger at lower ammonia pressures, though, regardless of the ammonia pressure, changes in selectivity at less than 0.7% conversion were always observed. These results suggest that acrolein undergoes secondary reaction to form acrylonitrile, although, in agreement with literature[27,28], this does not appear to be the major route to acrylonitrile since even at 0.2% conversion, the ACN selectivity is still greater than 55%.
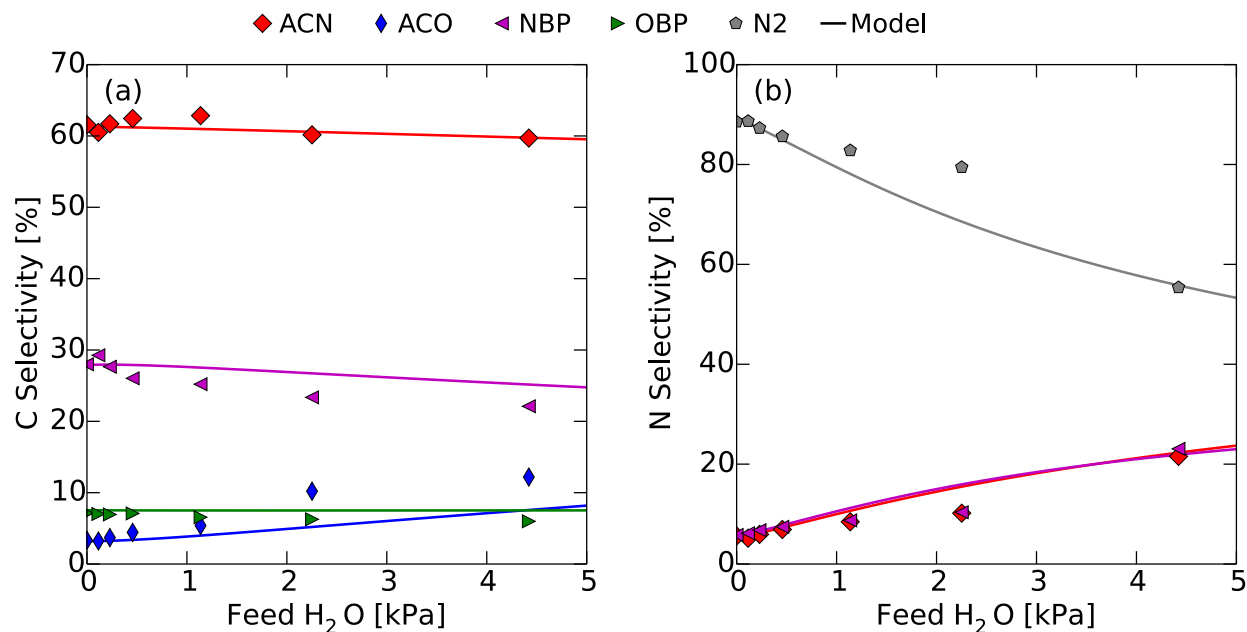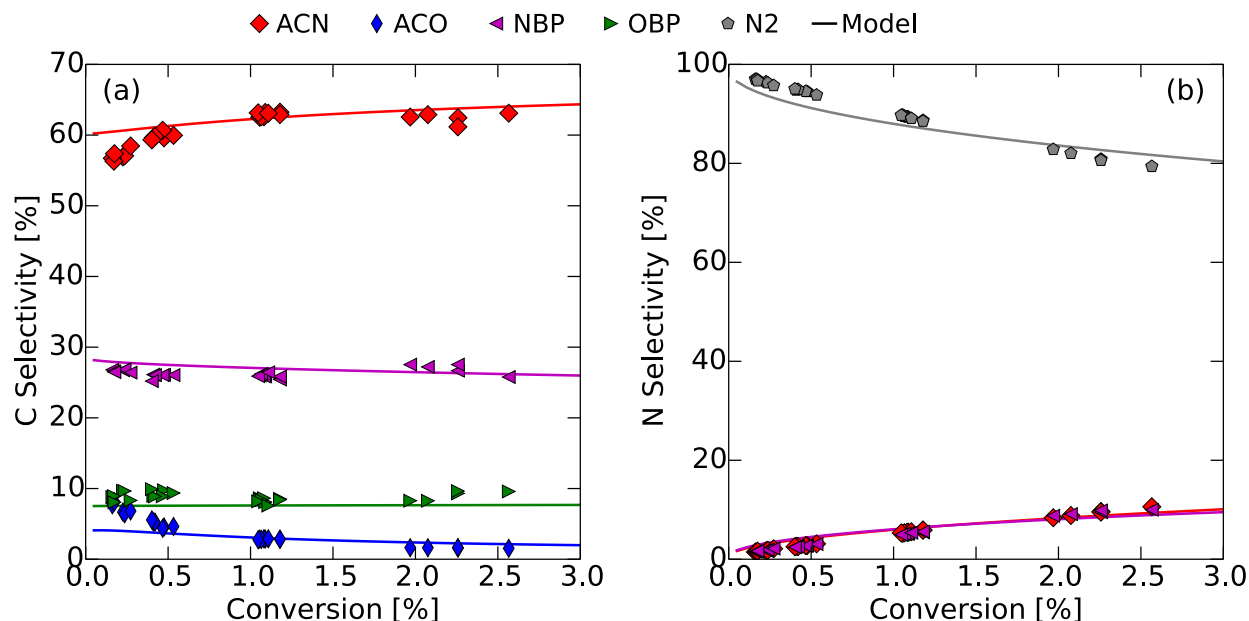
Fig. 1.9. Dependence of (a) carbon-scaled product selectivities and (b) nitrogen-scaled product selectivities, both versus propene conversion at 673 K, P_{C3H6} = 8.0 kPa, P_{NH3} = 8.0 kPa, and P_{O2} = 16.0 kPa. Symbols are data points; lines are calculated from the reaction network model.

The data in Figure 1.9 also show that both the nitrogen- and oxygen-containing byproducts are formed via primary routes, and not by secondary (amm)oxidation of the primary three-carbon products, since all selectivities are non-zero upon extrapolation to zero percent conversion. This finding is consistent with previous work, which has shown that for propene oxidation, oxygen-containing byproducts are not formed by combustion of acrolein[27,28]. We also observe a decrease in the dinitrogen selectivity from almost 100% to 80% with increased conversion, as water concentration increases with increasing conversion.

3.2.2. Secondary reactions of primary products

To further explore the role of secondary reactions, acrolein was fed to the reactor at 673 K together with ammonia and oxygen. Acrolein converts almost completely to nitrogen-containing products when fed with ammonia (Table 1.3), in agreement with prior studies[27]. At this high conversion of acrolein, we observe ~90% selectivity to acrylonitrile, with the rest of the C-atoms appearing as nitrogen- or oxygen-containing byproducts. In contrast, when either acrylonitrile or acetonitrile (lines 2 and 3 of Table 1.3, respectively) is fed to the reactor with ammonia and oxygen, its conversion is less than 1%, indicating that both compounds are relatively stable to secondary reaction. Similar results were obtained in the presence of propene in the feed stream. The much higher ratio of ACN to NBP when acrolein instead of propene is the reactant is used as the reactant another indication that most of the nitrogen-containing products are not formed via acrolein. Therefore, to a first approximation, the low selectivity to

16

the nitrogen-containing byproducts from acrolein and the negligible conversion of acrylonitrile allows us to neglect all secondary pathways to the byproducts in our proposed reaction network (Section 4).

Feed	Conv. (%)	Sel. ACN (%)	Sel. ACO (%)	Sel. NBP (%)
Acrolein + O_2 + NH_3	80	90	--	7
Acrylonitrile + O_2 + NH_3	<1	--	--	60
Acetonitrile + O_2 + NH_3	<1	--	--	50
Allylamine + O_2	~50	53	23	18
Allylamine + O_2 + NH_3	~50	56	9	29
Allylamine + O_2 + H_2O	~50	56	28	9
1,2-diaminopropane + O_2	0			

Table 1.3. Conversion of acrolein, acrylonitrile, allylamine, and 1,2-diaminopropane over $Bi_2Mo_3O_{12}$ at 673 K with $P_{hydrocarbon}$ = 0.2 kPa and P_{O2} = 16.3 kPa. Where indicated in table, P_{NH3} = 8.2 or P_{H2O} = 2 kPa. Carbon-scaled conversion (%) and selectivities (%) to ACN, ACO, and NBP, with remaining carbon conversion to OBP.

The reactivity of allylamine was also investigated. Even pure allylamine could not be accurately measured in our FID, presumably because its size and the stickiness of its –NH_2 group result in a broad peak that cannot be reliably integrated. However, by measuring the reaction products and knowing the inlet concentration of allylamine, the conversion of allyamine was estimated to be ~50% at the reaction conditions used for the other experiments listed in Table 1.3. Allylamine was reacted in the presence of oxygen (line 4), oxygen and ammonia (line 5), and oxygen and water (line 6). In all cases, the primary product was acrylonitrile, although products in all the other carbon product categories were also observed. Propionitrile was formed with a C-selectivity of <3% in all cases with allylamine as the reactant, so it is again lumped with acrylonitrile in the ACN product group. When ammonia was co-fed, the selectivity to the nitrogen-containing byproducts increased substantially, and when water was co-fed, the selectivity to acrolein increased substantially. The role of allylamine as a possible intermediate in propene ammoxidation will be discussed in Section 4.2. Finally, 1,2-diaminopropane was also fed over the catalyst without detectable formation of any product.

3.2.3 Kinetics of acrolein consumption

The data in Sections 3.2.1 and 3.2.2 lead to the conclusion that the reaction of acrolein and ammonia to form acrylonitrile is the only significant secondary process. In order to understand this reaction further, we investigated the influence of reactant partial pressures on this reaction at 603 K. A lower temperature was required in order to attain acrolein conversions

below ~5%. Figure 1.10 illustrates that, at low partial pressures, the rate of acrylonitrile formation is first-order in acrolein pressure, zero-order in oxygen pressure, and first-order in ammonia pressure.
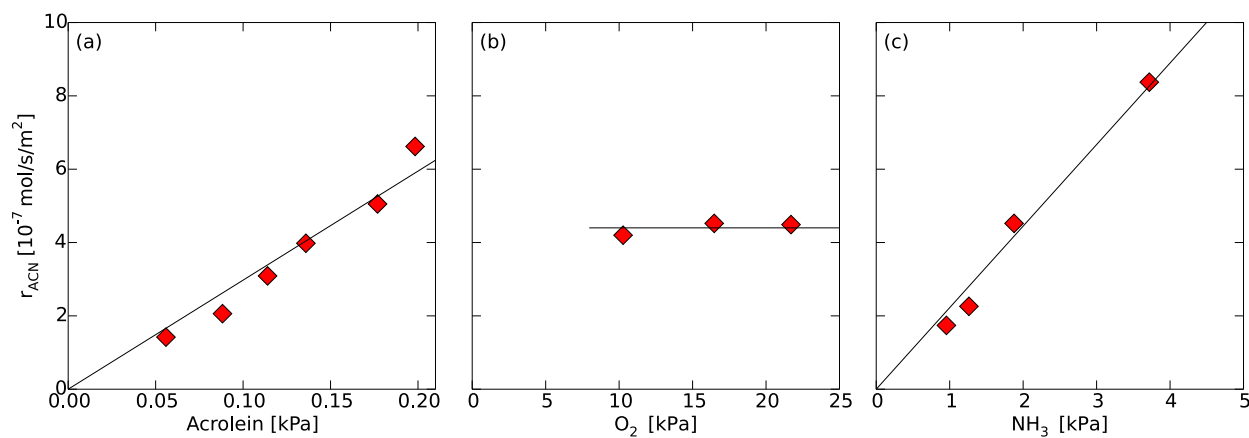
Fig. 1.10. Dependence of the rate of acrylonitrile formation on reactant partial pressures for the reaction of acrolein at 603 K. Total acrolein conversion 5%±2%. (a) Dependence on $P_{acrolein}$ with P_{O2} = 16.5 kPa and P_{NH3} = 1.9 kPa. (b) Dependence on P_{O2} with $P_{acrolein}$ = 0.14 kPa and P_{NH3} = 1.9 kPa. (c) Dependence on P_{NH3} with $P_{acrolein}$ = 0.14 kPa and P_{O2} = 16.5 kPa. Lines are to guide the eye.

3.3 Effects of temperature

An Arrhenius plot of the apparent rate coefficient (k_{RLS} defined in Eqn. 1.3) for the rate of propene consumption during propene ammoxidation (603 – 733 K) is shown in Figure A.2 in Appendix A. These data gives an activation energy of 22.4 ± 0.5 kcal/mol. This value agrees well with the activation energy calculated the same way for propene oxidation (21.7 ± 0.7 kcal/mol) at slightly lower temperatures (573 – 713 K) (see also Fig. A.2).

Figure 1.11 shows the carbon (a) and nitrogen (b) selectivities for each of the product groups across the same temperature range for conversions of 0.2-0.5%, 1.4-1.9%, and 2.7-3.4%. Two regimes are observed: one below ~673 K in which the selectivity to acrylonitrile decreases and the selectivity to the nitrogen-containing byproducts increases as the temperature decreases, and a second regime above ~673 K in which the selectivity to acrolein increases and the selectivity to the nitrogen-containing byproducts decreases as the temperature increases. The selectivity to the oxygen-containing byproducts is essentially constant at ~10% for all conversions and temperatures. The changes with temperature give some information about the relative activation energies to the different products after the common, initial rate-limiting step, as will be discussed in more detail in Section 4.
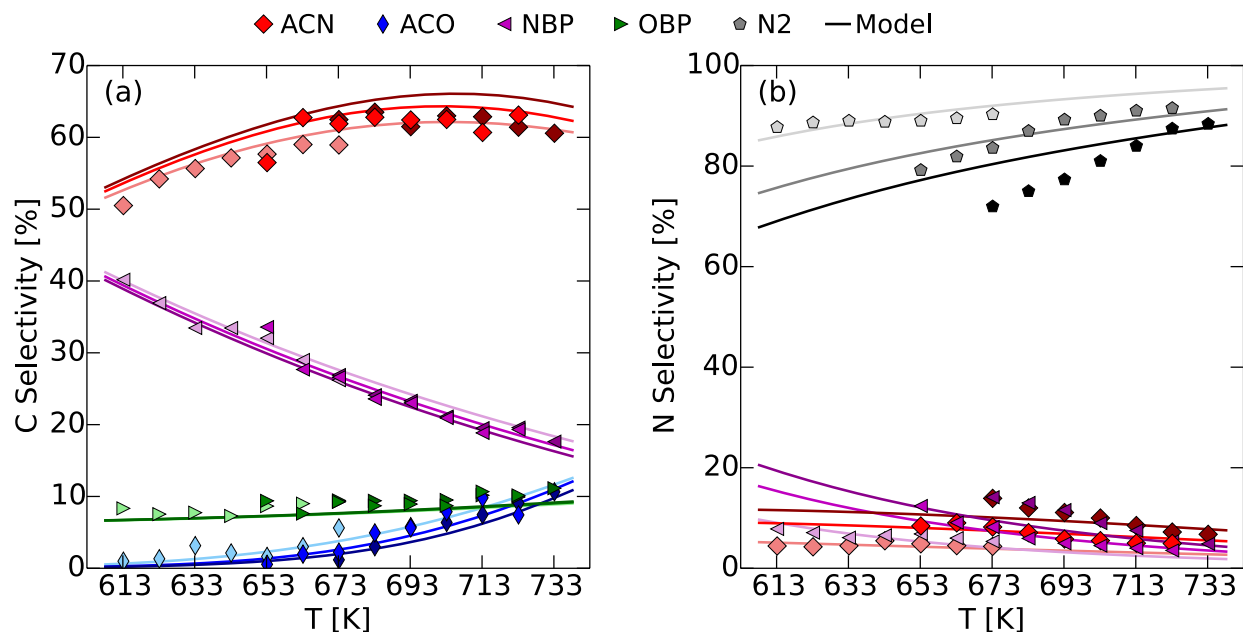
Fig. 1.11. Dependence of (a) carbon-scaled product selectivities and (b) nitrogen-scaled product selectivities on temperature. P_{C3H6} = 8.0 kPa, P_{NH3} = 8.0 kPa, and P_{O2} = 16.0 kPa. Symbols are data points; lines are calculated from the reaction network model. Light color = low C_3H_6 conversion (data 0.2-0.5%, model 0.4%), medium color = medium C_3H_6 conversion (data 1.4-1.9%, model 1.6%), dark color = high conversion (data 2.7-3.4%, model 3.0%).

As mentioned above, we report activation energies for propene oxidation and ammoxidation on the basis of the rate of propene consumption (k_{RLS} = ln(-r_{C3H6}/P_{C3H6}) vs. 1/T). This approach differs from that used in literature, where authors report activation energies from Arrhenius plots based on the rate of primary product (acrolein or acrylonitrile) formation (ln(r_{ACO}/P_{C3H6}) or ln(r_{ACN}/P_{C3H6}) vs. 1/T). However, when the natural log of product formation rate is plotted against inverse temperature, the result is not linear, since there is contamination from the changes in product selectivity with temperature. Our approach using the rate of propene consumption results in a truly linear Arrhenius plot (Appendix A, Fig. A.2). Since the products are thought to proceed via a common, initial, rate-limiting step[11,12,29] (see Section 4.2 for more discussion), the apparent activation energy determined from an Arrhenius plot based on propene consumption is the chemically significant quantity describing the energy for propene activation, whereas the chemical significance of an apparent activation energy determined from an Arrhenius plot based on product formation is not obvious. Nevertheless, to compare our results with those of previous researchers, we calculated the apparent activation energy for acrylonitrile formation for temperatures from 673 to 733 K, over which the Arrhenius plot is approximately linear. The resulting values are 19.4 ± 0.6 kcal/mol for propene ammoxidation and 19.9 ± 0.8 kcal/mol for propene oxidation, both of which agree very well with values by other researchers for similar catalysts (see Table 1.4). Though there is some variation between researchers in the

activation energy values, there is general agreement that the activation energy for acrylonitrile formation is essentially identical to that for acrolein formation.

Reference (Catalyst)	Calculation Method	E_a[kcal/mol] (T range)	
		Oxidation	Ammoxidation
This work $Bi_2Mo_3O_{12}$	Propene Consumption	21.7 ± 0.7 (573 – 713 K)	22.4 ± 0.5 (603 – 733 K)
This work $Bi_2Mo_3O_{12}$	Product Formation*	19.9 ± 0.8 (573 – 713 K)	19.4 ± 0.6 (673 – 733 K)
Callahan et al.[27] (Bi-P-Mo-O/SiO$_2$, Bi/Mo = 1.63)	Product Formation*		19 (Near 698 K)
Kolchin et al.[29] $Bi_2Mo_3O_{12}$	Product Formation*	20 – 21 (690 – 833 K)	18 – 19 (690 – 833 K)
Wragg et al.[28] (UBM4, Bi/Mo = 0.73)	Product Formation*	25 (673 – 773 K)	25 (648 – 723 K)

*Formation of acrolein or acrylonitrile respectively

Table 1.4. Reported activation energy for propene consumption and product formation over the temperature range listed in parentheses.

4. Discussion

Deductions drawn from the experimental results reported in the preceding section enable us to propose a new mechanism for the ammoxidation of propene over bismuth molybdate, which is illustrated in Scheme 1. Justifications for the steps included in this scheme are presented in Section 4.2, while Section 4.3 discusses the use of the proposed mechanism to describe the kinetics of propene ammoxidation. The results of this model are presented as the solid curves appearing in Figures. 1.5, 1.6, 1.8, 1.9, 1.11 and 1.12.
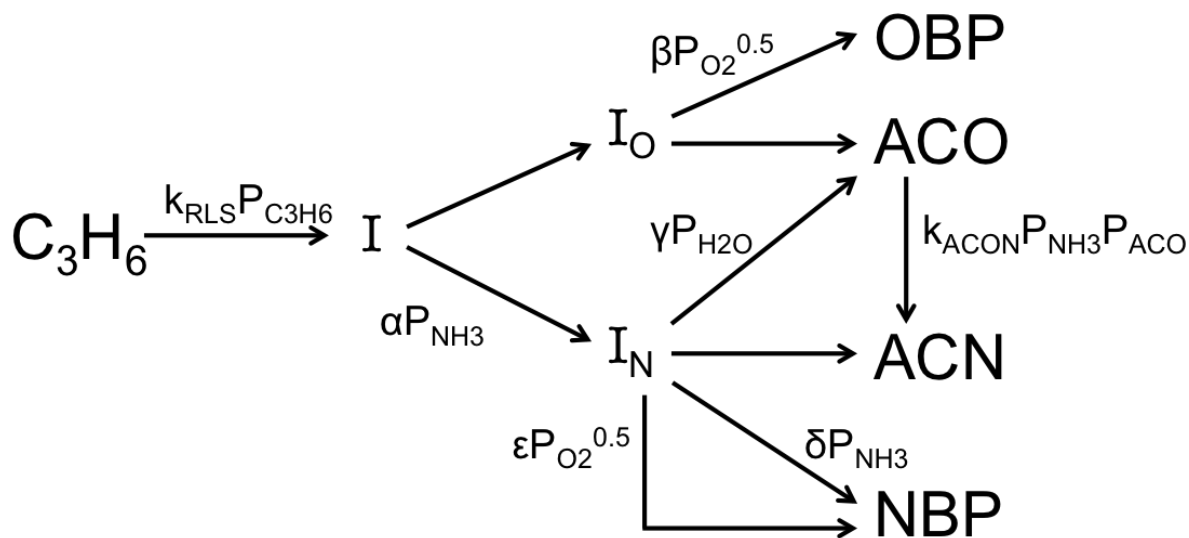
Scheme 1. Overall reaction scheme showing proposed routes to all major carbon-containing product groups.

4.1 Relevant nitrogen species

We propose that two N-containing species are present on the surface of $Bi_2Mo_3O_{12}$: NH_3 adsorbed on Bi^{3+} cations that are responsible for C-N bond formation and metastable $M-NH_x$ (M = Mo, Bi; x = 1, 2) species that are involved in N_2 formation, but are readily destroyed by reaction with water vapor to reform the native surface M-O species and NH_3. As discussed below, a very low surface concentration of Mo=NH species may also be responsible for the 1.6x rate enhancement in the rate of propene consumption after the catalyst has been pretreated with NH_3 and O_2 (see Table 1.2), which disappears upon exposure of the catalyst to high water concentrations.

The primary reason for proposing two distinct N-containing surface species is the observed differences in the responses of the rates of propene ammoxidation and of ammonia oxidation to the co-feeding of water. The rate of acrylonitrile formation is essentially unchanged upon addition of a moderate pressure of water, demonstrating that the N-containing species involved in C-N bond formation are unaffected by water. However, ammonia oxidation to N_2 is significantly suppressed by even a low pressure of water, achieved by either introducing water into the feed or by operating at higher propene conversion. N_2 formation can be completely suppressed by feeding a sufficiently high concentration of water, indicating that the N-containing species involved in N_2 formation is very sensitive to the presence of water.

DFT calculations of the interaction of NH_3 with $(O=Mo=O)_2Bi_2O_{10}H_{10}$, a cluster chosen to represent a part of the (010) surface of $Bi_2Mo_3O_{12}$ (see Appendix A for more details), show no evidence for NH_3 interaction with Mo^{6+} ions. However, adsorption of NH_3 on Bi^{3+} cations via a σ-donation of electron density from the lone pair on the N atom is favorable. This type of

interaction is similar to that proposed by Matsuura to explain the observation of weakly adsorbed NH_3 on the surface of Bi_2MoO_6 (ΔH_{ads} = -6.2 kcal/mol)[35]. Using our model cluster, we calculate $\Delta H_{ads,673K}$ = -12.7 kcal/mol and $\Delta G_{ads,673K}$ = -7 kcal/mol for adsorption of NH_3 on Bi^{3+}. The corresponding equilibrium constant for NH_3 adsorption at 673 K is $K_{eq} \sim 1.7$, and, assuming Langmuirian adsorption, the fraction of Bi^{3+} cations occupied by NH_3 is ~0.1 at a representative NH_3 pressure of 8 kPa. Additionally, the calculated enthalpy of NH_3 adsorption is unaffected by the presence or absence of a hydrocarbon intermediate on the neighboring Mo site.

The next question is whether water displaces adsorbed NH_3, since H_2O could also interact with Bi^{3+} cations via σ donation from the lone pair of electrons on oxygen. Our calculations indicate that the free energy for the adsorption of water is 3 kcal/mol less favorable than that for NH_3. Therefore, the addition of water, especially at a lower partial pressure than that of NH_3, should not significantly impact the low surface coverage of adsorbed NH_3. This insensitivity to water makes adsorbed NH_3 an attractive candidate for the N-containing species responsible for C-N bond formation. The occupancy of Bi^{3+} sites by NH_3 is expected to increase linearly with NH_3 pressure, since the occupancy of these cations is predicted to be in the Henry's law regime (~0.1 fractional occupancy of Bi^{3+} by NH_3, see discussion above). If, as discussed in Section 4.2, the formation of acrolein and acrylonitrile proceeds via a common intermediate that can react with adsorbed NH_3 to produce a precursor to acrylonitrile or undergo additional hydrogen abstraction to produce acrolein, the ratio of acrylonitrile to acrolein should depend on the occupancy of Bi^{3+} cations by NH_3 and should therefore increase linearly with NH_3 pressure. The data points in Figure 1.12 (a) indicate that this ratio is indeed nearly linear with NH_3 pressure for a range of temperatures, consistent with our proposal that reaction with adsorbed NH_3 is responsible for C-N bond formation. It is for this reason that the rate of I_N formation in Scheme 1 is proportional to NH_3 pressure. This relationship is used in the model of the reaction network (Scheme 1) in order to generate the best-fit lines appearing in Fig. 1.12a.
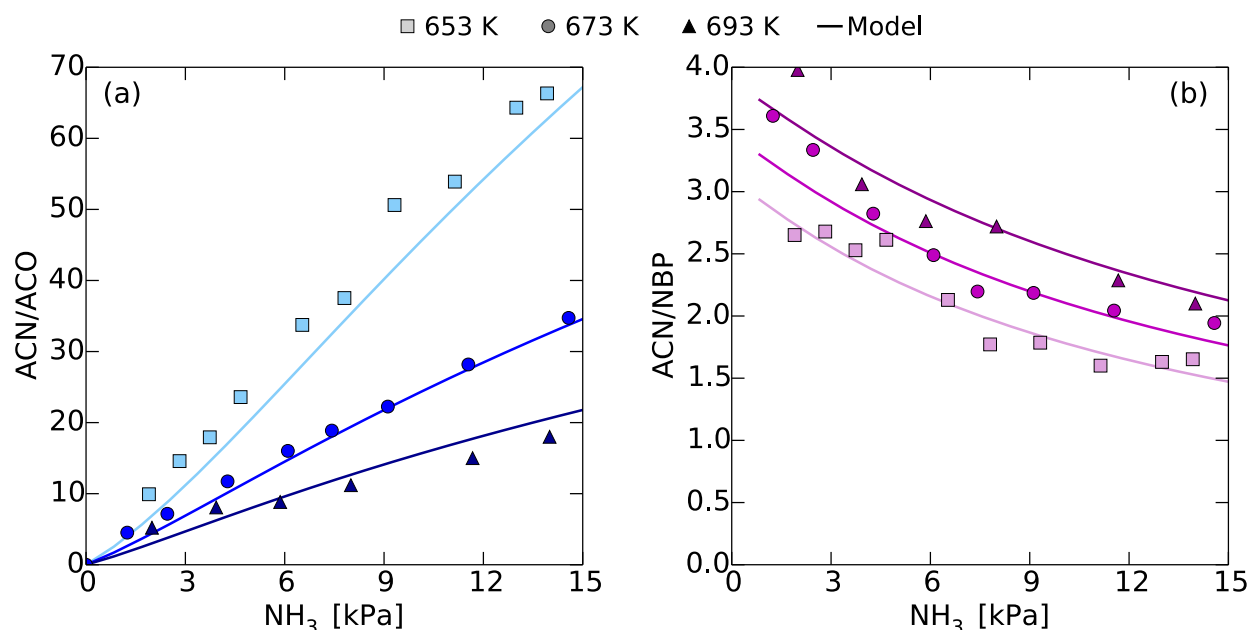
Fig. 1.12. Dependence of the product ratios (a) ACN/ACO and (b) ACN/BNP on the feed ammonia pressure for three different temperatures. P_{C3H6} = 8.0 kPa and P_{O2} = 16.3 kPa. 653 K (light color, ■) with C_3H_6 conversion 0.9%±0.1%; 673 K (medium color, ●) with C_3H_6 conversion 0.8%±0.1%; and 693 K (dark color, ▲) with C_3H_6 conversion 1.0%±0.1%. Symbols are data points; lines are calculated from the reaction network model.

As discussed in the Introduction, both theoretical calculations on a small Mo^{6+} cluster (ΔG_{673K} = 12.4 kcal/mol for (O=Mo=O)MoCl$_2$ + NH$_3$ → (O=Mo=NH)MoCl$_2$ + H$_2$O)[34] and the organometallic literature for Mo^{6+} complexes with imine ligands[35,36,37] indicate that Mo^{6+}=NH groups are not thermodynamically stable in the presence of water, and are therefore likely to be destroyed by reaction with water to reform the native Mo^{6+}=O groups and NH$_3$. Consistent with these observations, we have calculated the internal energy change for the reaction (O=Mo=O)$_2$Bi$_2$O$_{10}$H$_{10}$ + NH$_3$ → (O=Mo=NH)(O=Mo=O)Bi$_2$O$_{10}$H$_{10}$ + H$_2$O to be substantial (18.2 kcal/mol). Since ammonia oxidation to N$_2$ is significantly suppressed by water, we propose that low concentrations of Mo=NH or other M-NH$_2$ (M = Bi^{3+} or Mo^{6+}) species may be involved in N$_2$ formation. For example, it is possible to envision the reaction of Mo=NH with NH$_3$ to form hydrazine, which then could react further to produce N$_2$ and H$_2$O. For such a pathway to be viable, the activation barrier to form hydrazine would have to be low in order to compensate for the expected low concentration of the water sensitive Mo=NH groups. This proposed pathway to N$_2$ is admittedly speculative and, therefore, further research would need to be conducted in order to gain additional mechanistic insights into the ammonia oxidation reaction.

However, a very low concentration of Mo=NH groups may be responsible for the ~1.6x rate enhancement in the rate of propene oxidation and ammoxidation observed after catalyst

pretreatment in NH_3 and O_2 (see Table 1.2). If we assume that the rate-limiting step of alpha hydrogen abstraction from propene could occur with equal probability at either an Mo=O site with an activation energy ξ kcal/mol or at a Mo=NH site with an activation energy ξ-10 kcal/mol, both with the same activation entropy and thus the same pre-exponential factor, then only 1 Mo=NH site per 1100 Mo=O sites would result in a ~1.6x rate enhancement. Therefore, a contribution to propene activation from a very low concentration of metastable Mo=NH groups could explain both the observed ~1.6x increase in steady state propene consumption rate after prolonged exposure to NH_3, as well as the removal of said rate enhancement after subsequent treatment with a high pressure of water (see Table 1.2). In support of this proposal, Pudar *et al.* [39] have reported that Mo=NH groups are better hydrogen abstraction sites than Mo=O groups, and that the activation barrier for hydrogen abstraction by an Mo=NH group is ~10 kcal/mol lower than that for hydrogen abstraction by a Mo=O group. In agreement, we find the H radical addition energy, which is correlated with the energy required for hydrogen abstraction[16], on our $(O=Mo=O)_2Bi_2O_{10}H_{10}$ cluster to be 13.0 kcal/mol less negative (less favorable) for Mo=O than for Mo=NH. Therefore, we consider it plausible that a very low concentration of surface Mo=NH groups could contribute to the enhanced activity for propene consumption during propene oxidation and ammoxidation over $Bi_2Mo_3O_{12}$ pretreated in NH_3 and O_2 under conditions where the water pressure is relatively low.

4.2 Chemical justification for the proposed propene ammoxidation mechanism

Previous studies of propene oxidation and ammoxidation have found that the rate-limiting step for both reactions involves cleavage of one of the allylic C-H bonds[11,12,29]. The results presented here are fully consistent with this conclusion. The kinetics of propene consumption during oxidation and ammoxidation are identical; for both reactions, the rate is first-order in the pressure of propene and zero-order in the pressure of oxygen, and in the case of propene ammoxidation, zero order in the pressure of ammonia (see Fig. 1.1). Likewise, the apparent activation energies for propene oxidation and ammoxidation are essentially the same (see Table 1.4). Whereas earlier studies have suggested that the rate-limiting step occurs on oxygen atoms associated with bismuth[8,9,10], our recent experimental and theoretical work on propene oxidation provides compelling evidence that the active site is a molybdenyl oxo group (Mo=O) perturbed electronically by a neighboring bismuth atom[16,26]. We therefore propose that activation of propene occurs on the same site (Mo=O) during both propene oxidation and ammoxidation.

Our proposed mechanism for propene oxidation has been discussed previously[16,26], and therefore will only be summarized here. The allyl radical formed upon propene activation rapidly reacts with a Mo=O group to form a Mo-bound allyl alkoxide species (intermediate I), which then undergoes an energy-intensive[38] second hydrogen abstraction to produce coordinated acrolein at a reduced site (intermediate I_O). Acrolein coordinated at a reduced site is susceptible to attack by adsorbed oxygen atoms to produce the oxygen-containing byproducts, before

undergoing what Pudar *et al.* [38] found to be unfavorable acrolein desorption. These byproducts have been reported previously to derive primarily from an adsorbed acrolein precursor, and not via secondary combustion of acrolein[12,26]. Previous work has found that CO_2 production is 0.5 order in the pressure of oxygen[26], therefore, since CO_2 accounts for more than 50% of the oxygen-containing byproducts at all ammonia pressures (see Fig. 1.4), we treat the reaction of intermediate I_O to form oxygen-containing byproducts as dependent on the O_2 pressure to the 0.5 power. Since we are proposing that the catalyst surface is relatively unchanged upon ammonia exposure, the primary pathways to both acrolein and the oxygen-containing byproducts are assumed to occur via the same pathways when ammonia is present. We have indicated these two reactions in the top half of Scheme 1.

The oxidation and ammoxidation have a common initial rate-limiting step from propene, but most of the acrylonitrile is not formed via ammoxidation of acrolein (see above). Therefore, in order to form acrylonitrile, NH_3 must react with some hydrocarbon species that is in between the propene reactant and the acrolein product. This reactive hydrocarbon intermediate could be either the physisorbed allyl radical or the Mo-bound allyl alkoxide species (Mo^{5+}-$OCH_2CH=CH_2$), or both. The Mo-bound allyl alkoxide is the most likely species to react with adsorbed ammonia, since theoretical studies by Pudar *et al.* [38] using a molybdate molecular cluster report that the free energy barrier for the hydrogen abstraction from a Mo-bound allyl alkoxide to produce coordinated acrolein (viz. Mo^{6+}=O + Mo^{5+}-$OCH_2CH=CH_2$ → Mo^{5+}-OH + Mo^{4+}←O=CHCH=CH_2) is quite substantial (ΔG_{593K} = 37.5 kcal/mol). Theoretical studies in our own group on the (010) surface of $Bi_2Mo_3O_{12}$ also found that this second hydrogen abstraction is the second most energetically-difficult step in the production of acrolein[16]. Therefore, Mo-bound allyl alkoxide species should be the longest-lived propene-derived intermediates on the pathway to acrolein, making them prime candidates for reaction with NH_3 adsorbed on nearby Bi^{3+} cations to instead form acrylonitrile. We propose that if NH_3 adsorbs near a Mo^{5+}-$OCH_2CH=CH_2$ and reacts with it before it undergoes the difficult hydrogen abstraction, an acrylonitrile precursor would form. For this proposed reaction mechanism, the ratio of acrylonitrile to acrolein should be proportional to NH_3 pressure at low conversion, since at low coverage, adsorption is first-order in the adsorbent pressure. An approximately first order dependence is indeed observed experimentally (see Fig. 1.12 (a)). Additionally, the reaction with adsorbed ammonia must be energetically more favorable than hydrogen abstraction, in order to account for the observed high selectivity to acrylonitrile even at very low pressures of ammonia (see Fig. 1.5 (a)). In the bottom half of Scheme 1, we include a reaction between intermediate I (Mo-bound allyl alkoxide) and ammonia to form a carbon-nitrogen intermediate (I_N) that becomes relevant when ammonia is present in the feed.

Based on the preceding discussion, we hypothesize that the carbon-nitrogen intermediate (I_N) formed by the reaction of adsorbed NH_3 and Mo^{5+}-$OCH_2CH=CH_2$ may be adsorbed allylamine (Mo^{5+}-$OCH_2CH=CH_2$ + Bi^{3+}←:NH_3 → Mo^{5+}-OH + Bi^{3+}←:$NH_2CH_2CH=CH_2$). Previous researchers have investigated the reaction of allylamine over $Bi_2Mo_3O_{12}$, though they considered it as a probe molecule, instead of a potential intermediate[46]. They reported that

allylamine, both with and without co-fed ammonia, converts mainly to acrylonitrile, propionitrile, and acetonitrile, though with much higher yields of propionitrile than we observe. Their experiments with 1,1-d$_2$-allylamine produce almost exclusively d$_0$ acrylonitrile, indicating that the –CN group of allylamine remains intact during reaction. Our data for the reaction of allylamine are presented in Table 1.3. We observe that in the presence of oxygen, allylamine forms acrylonitrile with ~55% selectivity, as well as acrolein and the nitrogen-containing byproducts. Upon addition of ammonia to the allylamine and oxygen reactor feed, the selectivity to the nitrogen-containing byproducts increases significantly, and all the product ratios become approximately the same as those observed during propene ammoxidation at the same ammonia pressure. While these observations support the plausibility of adsorbed allylamine as a possible intermediate, without direct observation of during propene ammoxidation, they are not sufficient to unequivocally conclude that allylamine is indeed an intermediate.

We propose four separate pathways by which the intermediate I$_N$ can form the observed products. The most important among these is a series of four hydrogen abstractions that eventually produce acrylonitrile. If I$_N$ is indeed allylamine, we know from gas phase bond dissociation energy (BDE) calculations that the α-H of allylamine is quite weak (82 kcal/mol vs. 93 kcal/mol for the α-H of propene). Abstraction of this H atom leaves a NH$_2$-stabilized allyl species, which could undergo three additional hydrogen abstractions in a number of possible mechanisms to produce the very thermodynamically favorable acrylonitrile (NH$_2$-CH$_2$-CH=CH$_2$ + ½O$_2$ → NC-CH=CH$_2$ + H$_2$O; ΔG$_{673K}$ = -104 kcal/mol).

Two different routes from I$_N$ to nitrogen-containing byproducts are proposed. The first of these involves interaction with ammonia, possibly via addition of adsorbed NH$_3$ across the C-C bond of allylamine to create two CN fragments. The gas phase free energy for reaction of allylamine and ammonia to form methylamine and ethenamine is close to thermoneutral (ΔG$_{673K}$ = +3.7 kcal/mol), and can be driven by the extremely favorable oxidative dehydrogenation of these two molecules to make HCN or acetonitrile respectively and water (ΔG$_{673K}$ = -95 kcal/mol and -63 kcal/mol, respectively). 1,2-diaminopropane, the Markovnikov product of NH$_3$ addition across the C=C bond of allylamine, has a higher gas phase free energy of formation from allylamine (ΔG$_{673K}$ = +11.2 kcal/mol) than the C-C cleavage products, and that 1,2-diaminopropane decomposition was not observed experimentally (see Table 1.3). Since the observed ratio of HCN to acetonitrile ratio is 5:2, but we do not observe acetonitrile decomposition to HCN (Table 1.3), a fraction of the ethenamine (or some 2C-1N fragment precursor to acetonitrile) must undergo additional attack by NH$_3$ to create two 1C-1N fragments which each convert to an HCN molecule in a thermodynamically-favorable process. Since the ratio of acrylonitrile to the nitrogen-containing byproducts does not depend on ammonia pressure to the negative first power, but rather to a fractional negative power (see Fig. 1.12 (b)), a second route to the nitrogen-containing byproducts with a rate independent of ammonia pressure is also required.

We propose that this second route to the nitrogen-containing byproducts involves attack by adsorbed oxygen atoms, in a reaction similar to the one we propose to produce the oxygen-

containing byproducts. The exact mechanism for such a reaction is unclear and difficult to probe experimentally. Nevertheless, some process involving O to perform C-C bond cleavage and eventually produce the nitrogen-containing byproducts is necessary to explain the observed ~0.5 order in oxygen pressure (see Fig. 1.6 (a)). If I_N is allylamine, C-C bond scission should be relatively facile, since the BDE of this bond is only 96 kcal/mol as compared to the C-C bond of either propene or acrolein (BDE = 107 and 101 kcal/mol respectively). After the carbon-carbon bond scission event involving I_N and O, the fragments would need to incorporate additional NH_3 in order to create the nitrogen-containing byproducts.

We also include an additional pathway involving reaction of I_N with water to produce acrolein, in order to account for the observed increase in acrolein selectivity when water is added to the feed with either propene or allylamine as the reactant. The C-N bond of allylamine is its weakest bond, having a BDE of 76 kcal/mol, so this bond may break upon interaction with water to generate an acrolein precursor. A possible pathway for this is the approximately thermoneutral reaction of allylamine with water to create allyl alcohol and ammonia ($H_2C=CH-CH_2-NH_2 + H_2O \rightarrow H_2C=CH-CH_2-OH + NH_3$; $\Delta G_{673K} = +1.3$ kcal/mol), followed by the thermodynamically very favorable reaction of allyl alcohol and oxygen to produce acrolein and water ($H_2C=CH-CH_2-OH + O_2 \rightarrow H_2C=CH-CHO + H_2O$; $\Delta G_{673K} = -53$ kcal/mol). The conversion of allyl alcohol to acrolein with high selectivity, as well as the slight conversion of allylamine to acrolein in the presence of water, has been reported previously[46,47].

Additionally and in agreement with previous reports[27,28], we find that acrolein reacts in the presence of ammonia to form acrylonitrile (see Table 1.3). The reactivity of acrolein with ammonia is consistent with the results shown in Figure 1.10, which illustrates the intrinsic first-order dependencies of acrolein reaction to acrylonitrile on the partial pressures of both acrolein and ammonia. A small amount of nitrogen-containing byproducts are observed when acrolein is the reactant; however, the selectivity is approximately ten-fold lower than the selectivity to acrylonitrile. Therefore, to a first approximation, the secondary reaction of acrolein to NBP can be neglected. Considering the selectivity versus conversion data presented in Fig. 1.9, the small, but detectable, influence of the secondary pathway from acrolein to acrylonitrile is directly observable at low conversions. The inclusion of this reaction in our network completes the pathways for Scheme 1.

The final reaction occurring during propene ammoxidation is the oxidation of ammonia to nitrogen gas. Selective catalytic oxidation (SCO) of ammonia has been found to occur over many different metal oxides, including Bi_2MoO_6 and molybdenum oxides with and without Bi or Pb doping[40,48]. These studies found ammonia SCO to be first-order in ammonia and zero-order in oxygen pressures, and to be inhibited by water, though not suppressed to the same extent as during propene ammoxidation over $Bi_2Mo_3O_{12}$. As discussed in Section 4.1, we propose that N_2 formation involves the reaction of gas-phase ammonia with surface $M-NH_x$ groups (M = Bi, Mo; x = 1, 2). The destruction of these groups upon contact with water may explain the significant suppression of the rate of N_2 formation upon co-feeding even a moderate concentration of water, even though the rate of propene consumption is not affected. Irrespective of how N_2 is formed,

the rate of formation of this product can be described empirically by Eqn. 1.4. This rate expression involves two rate coefficients, k_{N2} and k_{H2O}, which we do not attempt to interpret chemically.

$$r_{N_2} = \frac{k_{N_2}P_{NH3}}{1+k_{H_2O}P_{H2O}}$$

(1.4)

4.3 Reaction network model

The reaction network given in Scheme 1 was used to develop a model for the kinetics of propene ammoxidation. Expressions for propene consumption and for ammonia oxidation to N_2 are described by Eqns. 1.3 and 1.4, respectively. Based on the discussion presented in Section 3.2.3, a rate expression for acrolein ammoxidation to acrylonitrile can be written as $k_{ACON}P_{ACO}P_{NH3}$. By applying the pseudo-steady-state approximation to the three intermediate species, I, I_O, and I_N, the remaining reactions can be described by five independent selectivity ratios. As shown in Scheme 1, these are:

(i) αP_{NH3} The ratio of the rate at which I is converted to I_N relative to the rate at which it is converted to I_O.

(ii) $\beta P_{O2}{}^{0.5}$ The ratio of the rate at which I_O is converted to the oxygen-containing byproducts relative to the rate at which it is converted to acrolein.

(iii) γP_{H2O} The ratio of the rate at which I_N is converted to acrolein relative to the rate at which it is converted to acrylonitrile.

(iv) δP_{NH3} The ratio of the rate at which I_N is converted to the nitrogen-containing byproducts with NH_3 relative to the rate at which it is converted to acrylonitrile.

(v) $\varepsilon P_{O2}{}^{0.5}$ The ratio of the rate at which I_N is converted to nitrogen-containing byproducts with O_2 relative to the rate at which it is converted to acrylonitrile.

The aforementioned parameters are used in the overall rate expressions given by Eqns. 1.5-8. Since the selectivity to the oxygen-containing byproducts at all conditions was >6%, we assume that 6% of the fed propene goes to these products. In this way, the selectivity to the oxygen-containing byproducts will exhibit the observed >50% decrease in selectivity upon addition of the lowest experimentally-attainable NH_3 pressure, and still be finite when P_{NH3} is high.

$$r_{ACN} = 0.94 k_{RLS}P_{C3H6}\left(\frac{\alpha P_{NH3}}{1+\alpha P_{NH3}}\right)\left(\frac{1}{1+\gamma P_{H2O}+\delta P_{NH3}+\varepsilon P_{O2}{}^{0.5}}\right) + k_{ACON}P_{ACO}P_{NH3}$$

(1.5)

$$r_{NBP} = 0.94 k_{RLS}P_{C3H6}\left(\frac{\alpha P_{NH3}}{1+\alpha P_{NH3}}\right)\left(\frac{\delta P_{NH3}+\varepsilon P_{O2}{}^{0.5}}{1+\gamma P_{H2O}+\delta P_{NH3}+\varepsilon P_{O2}{}^{0.5}}\right)$$

(1.6)

28

$$r_{ACO} = 0.94 k_{RLS} P_{C3H6} \left[\left(\frac{1}{1+\alpha P_{NH3}} \right) \left(\frac{1}{1+\beta P_{O2}{}^{0.5}} \right) + \left(\frac{\alpha P_{NH3}}{1+\alpha P_{NH3}} \right) \left(\frac{\gamma P_{H2O}}{1+\gamma P_{H2O}+\delta P_{NH3}+\varepsilon P_{O2}{}^{0.5}} \right) \right] -$$
$$k_{ACON} P_{ACO} P_{NH3} \tag{1.7}$$

$$r_{OBP} = 0.94 k_{RLS} P_{C_3H_6} \left(\frac{1}{1+\alpha P_{NH3}} \right) \left(\frac{\beta P_{O2}{}^{0.5}}{1+\beta P_{O2}{}^{0.5}} \right) + 0.06 k_{RLS} P_{C_3H_6} \tag{1.8}$$

Eqns. 1.3-8 were incorporated into a steady-state, one-dimensional, plug-flow reactor model to calculate the conversion of propene, ammonia and oxygen to various products. An integral reactor model was needed to account for changes in the concentrations of ammonia and water through the reactor, even though the conversion of propene was small. The rate parameters appearing in the model were determined by fitting the selectivity outputs to the observed selectivity data at the experimentally observed propene conversion. More details about the modeling process are given in Appendix A.

The rate parameters were initially regressed to selectivity data at 673 K, and then extended to other temperatures by fitting an activation energy and setting the pre-exponential factor to give the previously optimized rate parameter determined for 673 K. Table 1.5 lists the activation energies and pre-exponential factors for all of the rate coefficients described above. Values of the pre-exponential factor and the activation energy for k_{RLS} were obtained from the Arrhenius plot (see Appendix A), and the activation energy for k_{ACON} was taken from the literature[26]. All other values were obtained by fitting the model to the data, but because of the model complexity and large number of independent variables, they have a high degree of uncertainty. It is evident from the solid curves in Figures 1.5, 1.6, 1.8, 1.9, 1.11, and 1.12 that, while not perfect, the model is able to capture the trends in the experimental data as a function of all partial pressures, conversions and temperatures investigated.

	Ea (kcal/mol)	A	Units of A
k_{RLS}	22.4 ± 0.5	2.3 ± 1	mol/s/m^2/kPa
k_{ACON}	7 ± 2	$6(\pm 3) \times 10^{-04}$	mol/s/m^2/kPa^2
k_{N2}	35 ± 5	$9(\pm 5) \times 10^5$	mol/s/m^2/kPa
k_{H2O}	2 ± 2	$5(\pm 3) \times 10^1$	mol/s/m^2/kPa
α	-15 ± 5	$3(\pm 2) \times 10^{-05}$	mol/s/m^2/kPa
β	-5 ± 2	$2(\pm 1) \times 10^{-03}$	mol/s/m^2/kPa
γ	10 ± 5	$2(\pm 1)$	mol/s/m^2/kPa
δ	-10 ± 5	$1(\pm 0.5) \times 10^{-05}$	mol/s/m^2/kPa
ε	-5 ± 2	$2(\pm 1) \times 10^{-03}$	mol/s/m^2/kPa

Table 1.5. Values of the activation energy E_a and the pre-exponential factor A used in our kinetic model for each of the reactions and selectivity ratios shown in Scheme 1.

Our values for k_{RLS} (1×10^{-7} mol/s/m^2/kPa) and k_{ACON} (3×10^{-6} mol/s/m^2/kPa^2) calculated from the Arrhenius parameters at 673 K for Bi$_2$Mo$_3$O$_{12}$ are within an order of magnitude of those reported by Wragg *et al.*[28] for propene and acrolein ammoxidation over a different catalyst with Bi:Mo of 0.73:1 at 673 K, though their rate law for acrolein ammoxidation did not involve P_{NH3} ($k_{RLS} = 5 \times 10^{-8}$ mol/s/m^2/kPa assuming a BET surface area of 1.0m^2/g; $k_{ACON} = 6 \times 10^{-7}$ mol/s/m^2/kPa^2 assuming a BET surface area of 1.0m^2/g and dividing out a $P_{NH3} = 20$ torr). The large activation energy associated with k_{N2} indicates that critical step in the oxidation of ammonia is demanding, consistent with the high BDE of the N-H bonds in NH$_3$ (114.1 kcal/mol). We not attempted to use theory to elucidate a possible mechanism for NH$_3$ oxidation to N$_2$, choosing to focus only on the main carbon-containing products. Our N$_2$ activation energy is in agreement with the value reported by Matsuura for first order ammonia oxidation to N$_2$ over Bi$_2$MoO$_6$ (37 kcal/mol)[40].

In agreement with previous studies that find acrylonitrile is mostly produced from primary reaction of propene[27,28], our model indicates that, at stoichiometric feed conditions, 673 K and 1% conversion, only ~5% of the outlet acrylonitrile is produced via acrolein. This is equivalent to ~50% of the acrolein generated in the reactor being converted to acrylonitrile in secondary reaction, consistent with the low activation energy for acrolein to acrylonitrile reaction. At these same conditions (stoichiometric feed, 673 K, 1% conversion), our model predicts that approximately one third of the produced acrolein is from reaction of I$_N$ and H$_2$O, with the remainder coming via I$_O$. We also find that the majority (~70%) of the nitrogen-containing byproducts are produced from I$_N$ via initial reaction with adsorbed oxygen, rather than initial reaction with NH$_3$.

The negative activation energies for β, δ, and ε demonstrate that higher temperatures favor the three-carbon products over the one- and two-carbon products. Burrington *et al.*[14] also found that the formation of acrylonitrile during ammoxidation and acrolein during oxidation relative to CO$_2$ is favored at higher temperatures on Bi$_2$Mo$_3$O$_{12}$. A large, negative value for the activation energy associated with α is found, which accounts for the higher observed selectivity to acrolein during ammoxidation at high temperatures (see Fig. 1.11(a)). This negative sign and the magnitude of this activation energy reflect the substantially higher activation energy for hydrogen abstraction from allyl alkoxide to produce (primarily) acrolein compared to reaction with adsorbed NH$_3$ to produce (primarily) acrylonitrile. This pattern is consistent with the theoretical analysis showing that hydrogen abstraction from allyl alkoxide is a difficult process[16,38], and implies that reaction of the allyl alkoxide with adsorbed ammonia is facile.

5. Conclusions

This study provides new insights into the mechanism of propene ammoxidation over Bi$_2$Mo$_3$O$_{12}$, and in particular the manner in which reaction conditions affect the distribution of products. Our results confirm that the kinetics of ammoxidation are first order in propene pressure and zero order in both oxygen (for O$_2$/C$_3$H$_6 > 1.5$) and ammonia pressures, and that the

apparent activation energy for propene consumption is ~22 kcal/mol for both propene oxidation and ammoxidation. The similarity in the activation energy and the dependence on only propene pressure for both propene oxidation and ammoxidation suggests that both reactions occur via a common rate-limiting step, in good agreement with prior studies.

We propose that two types of N-containing species are involved in propene ammoxidation: one that is extremely sensitive to water and one that is not. NH_3 adsorbed on Bi^{3+} ions is taken to be the N-containing species responsible for C-N bond formation. DFT calculations suggest that under the conditions of our experiments, the occupancy of Bi^{3+} cations by adsorbed NH_3 is low, but non-zero, and that NH_3 adsorption is insensitive to the presence of water. Additional DFT calculations indicate that Mo^{6+}=NH groups are highly unstable thermodynamically in the presence of water. Therefore, we propose that surface $M-NH_x$ (M=Bi, Mo; x=1, 2) species are responsible for NH_3 oxidation to N_2, a reaction that can be completely suppressed by moderate pressures of water. The unlikelihood of Mo=NH groups participating in the formation of C-N bonds is supported by our observation that the formation of acrylonitrile and other N-containing compounds is unaffected by the presence of water.

We hypothesize that the C-N bond formation during propene ammoxidation may proceed via the reaction Mo^{5+}-OCH_2CH=CH_2 + Bi^{3+}←:NH_3 → Mo^{5+}-OH + Bi^{3+}←:NH_2CH_2CH=CH_2. While the product of this reaction, allylamine, was not observed as an intermediate, introduction of allylamine together with ammonia and oxygen produces a product distribution very similar to that observed during propene ammoxidation. The reaction leading to allyamine is thought to compete with that leading to acrolein (Mo^{6+}=O + Mo^{5+}-OCH_2CH=CH_2 → Mo^{5+}-OH + Mo^{4+}←O=CHCH=CH_2). Even at low pressures of ammonia and low conversion, the selectivity to acrylonitrile dominates that to acrolein, indicating that the former reaction is preferred over the later. We have also shown, in agreement with previous researchers[27], that while acrolein is easily converted to acrylonitrile, this process likely accounts for only ~5% of the acrylonitrile formed.

Acetonitrile and hydrogen cyanide are the dominant nitrogen-containing carbon byproducts formed during propene ammoxidation. The selectivity to these products increases with increasing ammonia and oxygen pressures, but is not very sensitive to propene conversion or the pressure of water vapor, and decreases with increasing temperature. We hypothesize that two different reaction mechanisms are important for the formation of acetonitrile and hydrogen cyanide – one involving addition of an adsorbed NH_3 across the C-C bond of allylamine to form methylamine and ethenamine, and one involving reaction of allylamine with surface O resulting in C-C bond scission. Since the observed ratio of HCN to acetonitrile ratio is a constant 5:2, in either case, the intermediates would need to undergo additional attack by NH_3.

The reaction mechanism shown in Scheme 1 was proposed to account for all observed products and byproducts, and was used to build a model of the kinetics of product formation as a function of reactant and product partial pressures and temperature. With the rate parameters given in Table 1.5, this model does a reasonably good job of describing the effects of reaction conditions on the distribution of products. The model also reveals that to achieve high yields of

acrylonitrile, it is desirable to operate at high temperatures, low pressures of ammonia, and low pressures of oxygen. These conditions minimize the formation of acetonitrile and hydrogen cyanide, but increase the intrinsic selectivity to acrolein. However, conversion of the later product to acrylonitrile via secondary reaction is highly favorable, especially at higher propene conversions. Our work also shows that addition of moderate pressures of water vapor to the feed can significantly suppress the wasteful consumption of ammonia to N_2, while having only a very minimal effect on the carbon product distribution.

Chapter 2

A DFT Investigation of the Mechanism of Propene Ammoxidation over α-Bismuth Molybdate[0]

1. Introduction

Approximately 25% of the organic chemical building blocks produced commercially are obtained via heterogeneously catalyzed partial oxidation of alkanes or alkenes.[1] Two of the most important examples of such reactions are propene oxidation to acrolein and propene ammoxidation to acrylonitrile:

$$C_3H_6 + O_2 \rightarrow C_3H_4O + H_2O$$

$$C_3H_6 + {}^3/_2\,O_2 + NH_3 \rightarrow C_3H_3N + 3\,H_2O$$
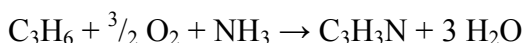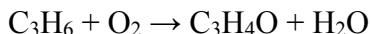
These reactions produce ~10 billion pounds/year each of acrolein, about 90% of which is directly converted to acrylic acid,[2] and of acrylonitrile,[3] which is used to produce plastics (e.g. ABS, SAN, NBR) and high volume commodity chemicals (e.g., acrylic fiber, acrylamide, adiponitrile). Both reactions occur with high intrinsic carbon selectivity over alpha bismuth molybdate $Bi_2Mo_3O_{12}$, ~70% for propene oxidation to acrolein and ~60% for propene ammoxidation to acrylonitrile.[4] While industrial catalysts have been engineered over the past 60 years to attain even higher product yields, the majority of the catalysts used still contain bismuth and molybdenum as key elements.[1]

The mechanism and kinetics of propene oxidation and ammoxidation have many features in common. The apparent activation energy for both reaction is virtually the same (~22 kcal/mol) and the rate of both reactions is first-order in propene pressure, zero-order in oxygen pressure, provided the feed concentration of oxygen is stoichiometric or greater, and zero-order in ammonia pressure (for propene ammoxidation).[4,5,6,7,8] Both deuterium[9,10,11] and carbon-13[12,13,14] labeling experiments provide compelling evidence that the rate-determining step for both reactions is the same, and involves hydrogen abstraction from the methyl group of propene to produce a loosely adsorbed allyl species. Since the initial propene activation step is rate-

determining, it is difficult to probe the subsequent reactions and, therefore, several hypotheses have been presented to account for the formation of acrolein and acrylonitrile. In particular, while acrolein is produced in only low concentrations when ammonia is present and is not thought to be an intermediate on the primary path to acrylonitrile,[4,5,8] it is not clear at what point the common intermediate diverges to become either acrolein or acrylonitrile.

Insights into the activation of propene on $Bi_2Mo_3O_{12}$ have also been obtained from density functional theory calculations. Despite many of the inherent challenges of modeling reducible transition metal oxides with DFT because of problems with electron self-interaction error, previous work has found that reasonably accurate estimates of oxide semi-conductor band gaps, lattice parameters, heats of molecular adsorption and reaction energies can be obtained at a supportable cost using the M06-L functional[15] implemented for a periodic boundary system representation of the (010) surface of $Bi_2Mo_3O_{12}$.[16] Using this approach, we have investigated the surface chemistry involved in the oxidation of propene to acrolein. This work has shown that the most active site for the rate-limiting propene activation step is a surface molybdenyl oxo that is mildly perturbed electronically by a nearby bismuth cation,[16,17] and not an oxygen atom bound to bismuth as proposed previously.[18,19,20] The apparent activation energy calculated for the abstraction of a hydrogen atom from the methyl group of propene by this oxo group is 27.9 kcal/mol.[16] This value is in reasonably good agreement with the experimentally measured value of 22kcal/mol,[4] considering the technical difficulties associated with the calculations. The theoretical finding that the active site is an oxygen atom bound only to molybdenum is consistent with our experimental *in situ* XANES results, which show that, even under extremely reducing conditions (exposure to pure propene for 24 h at 713 K), only molybdenum is reduced from 6+ to 4+ and bismuth remains in the 3+ oxidation state.[7]

Experiments with $^{18}O_2$ have demonstrated that the acrolein O originates from the catalyst, and not from gas phase oxygen,[21,22] leading to a general consensus that, after the initial hydrogen abstraction, the nascent allyl radical first inserts into a molybdenyl oxo $Mo^{6+}=O$ to form an allyl alkoxide species, which then undergoes a hydrogen abstraction followed by desorption of acrolein leaving a reduced Mo^{4+} site.[17,20] Based on calculations conducted using a Mo_3O_9 cluster, Pudar *et al.*[23] have estimated that both the hydrogen abstraction step and the release of acrolein to leave a Mo^{4+} cation are demanding steps with activation barriers of 35.6 kcal/mol and 31.9 kcal/mol, respectively. The authors proposed that acrolein release may be facilitated by concurrent adsorption of gas phase oxygen on molybdenum, thereby maintaining molybdenum in a higher oxidation state and resulting in acrolein release being energetically favorable.

Burrington *et al.*[20] have proposed, by analogy with the mechanism for propene oxidation, that propene ammoxidation involves the insertion of an allyl radical into a molybdenyl imido $Mo^{6+}=NH$ group, followed by three hydrogen abstraction steps. The authors proposed that the catalyst surface is dominated by imido groups, formed by the reaction of NH_3 with Mo=O groups, since little acrolein is produced during propene ammoxidation.[24] Using this scheme as a basis, Pudar *et al.*[25] explored the reaction of allyl radicals with a Mo_3O_9 cluster in which 1, 2, 3 or 6 of the oxo groups is replaced with imido groups. This work showed that hydrogen

abstraction by an imido group is ~8 kcal/mol more favorable than by an oxo group, and that a spectator imido bound to the same Mo^{6+} further facilitates hydrogen abstraction by an additional ~15 kcal/mol. It is notable, however, that the production of an imido group and water by reaction of ammonia with an Mo oxo group is endothermic by 13.7 kcal/mol, indicating that the imido groups will be unstable in the presence of water.[26]

Given the unfavorable thermodynamics for imido group formation on the surface of bismuth molybdate, these groups are not likely to be present at high coverages during propene ammoxidation, since this reaction produces a considerable amount of water. Consistent with this reasoning, we have recently reported that co-feeding water together with propene, oxygen, and ammonia has a negligible effect on the rate of acrylonitrile formation, leading to the conclusion that imido groups are unlikely to be responsible for C-N bond formation.[4] We have proposed, instead, that the formation of C-N bonds occurs via the reaction of allyl alkoxide groups (produced by addition of an allyl radical to a Mo=O group) with ammonia adsorbed on Bi^{3+} cations via sigma donation from the lone pair on the nitrogen atom of NH_3. The product of this step was proposed to be adsorbed allylamine. While this compound was not observed as a stable product, introduction of allylamine with ammonia and oxygen at conditions of propene ammoxidation resulted in a product distribution very similar to that observed during propene ammoxidation.[4]

A small amount of acrolein has been observed during propene ammoxidation under conditions of differential conversion; however, the majority of the acrolein produced undergoes facile secondary reaction to acrylonitrile with an activation energy of ~7 kcal/mol.[4,5,8] Finally, acetonitrile and hydrogen cyanide (HCN) are important byproducts of propene ammoxidation. Our experimental studies have shown that these products are produced from propene in an approximately constant ratio of 5 HCN: 2 acetonitrile at all conditions, and together account for ~30% of the reacted propene.[4]

The aim of the present investigation was to carry out a detailed analysis of the reaction pathways involved in the oxidation and ammoxidation of propene. Specific objectives were to identify the elementary steps for the formation of both acrolein and acrylonitrile during propene ammoxidation, the pathway by which acrolein is subsequently converted to acrylonitrile, and the pathways by which the byproducts acetonitrile and hydrogen cyanide are formed. The objectives were pursued by analysis of the energetics for the reaction pathway proposed on the basis of our experimental studies.[4] Periodic density functional theory (DFT) calculations were conducted on the (010) surface of $Bi_8Mo_{12}O_{48}$. Given the very large number of organic intermediate structures investigated, we only considered the reaction barriers for three key steps: (1) hydrogen abstraction from propene, the rate-limiting step that is common to propene oxidation and ammoxidation; (2) hydrogen abstraction from surface allyl alkoxide species to produce adsorbed acrolein; and (3) the reaction of allyl alkoxide species with adsorbed ammonia to produce allylamine. All other aspects of the reaction pathways were explored by examining the energies of reaction.

2. Theoretical methods

All calculations were performed using the Vienna *Ab initio* Simulation Package (VASP)[27] version 5.3.5 using the PBE[28] and M06-L[15] functionals. Plane wave basis sets[29] were used to model valence electrons and projector augmented wave (PAW) functions[30,31] were used to model the core electrons. The PAW cores were designed for a plane wave cutoff energy of 400 eV and this cutoff was used for all calculations. We used 240 bands in order to capture the 200 electron pairs present in $Bi_8Mo_{12}O_{48}$, the lowest energy unoccupied bands involved in reactions, and the additional electrons introduced with the reactants. Convergence tests with respect to k-point mesh revealed that 3x2x2 k-points are sufficient to simulate the bulk $Bi_8Mo_{12}O_{48}$ with the M06-L functional.[16] Energies were converged with a Gaussian energy smearing of 0.05 eV.

The bulk atomic positions of $Bi_8Mo_{12}O_{48}$, which is one unit cell of alpha bismuth molybdate, were taken from literature[32] and allowed to relax at a series of fixed volumes[16]. The Burch-Murnaghan Equation of State[33] was used to fit the data of energy versus volume to calculate the cell volume with the minimum energy. The atoms were then allowed to relax at this fixed minimum energy volume until the total energy converged to within 0.1 meV. The optimized cell volume from this method is ~2.3% larger than the experimental unit cell volume.[16] In order to generate the lowest energy (010) surface, 14 Å of vacuum was introduced above the bulk $Bi_8Mo_{12}O_{48}$ atoms and the top two layers of the four layer unit cell were allowed to relax to a convergence of 0.5 meV with 3x1x2 k-points, while the bottom two-layers were fixed in their bulk positions to simulate the bulk oxide below the surface. The Minnesota family of functionals requires a fine integration grid to provide accurate energies,[34] therefore an integration grid of 90 x 288 x 144 was used in all calculations.

To model reactant and product structures, the positions of both the reactants and the relevant atoms at the active site were optimized initially with the less-computationally-intensive PBE functional and with 1x1x1 k-points. Once a structure was optimized to within 0.5 meV, the entire surface was allowed to relax using the M06-L functional with 3x1x2 k-points until the final structure converged to within 1 meV. The charge density and wave function from a single point PBE calculation was always used as an initial guess for M06-L calculations, since the M06-L functional performs poorly with the default random number initial guess of the wave function.

The Nudged Elastic Band (NEB) method[35] was used to calculate the three reaction barriers we investigated. As mentioned in the Introduction, the transition state for the rate-limiting hydrogen abstraction from propene has been found to be the singlet-triplet spin crossing.[17] Therefore, for this barrier, we first optimized a spin-relaxed pathway until the forces on all the atoms were less than 0.1 eV/Å. We then ran two single-point NEBs on the final optimized pathway geometries, one confined in the singlet state and one confined in the triplet state, and extracted the forces and energies. From these data, we generated cubic splines

representing the singlet and triplet potential energy surfaces and found the spin crossing point. We interpolated along the pathway to find the geometry at the spin crossing point, and verified that the resulting geometry had the same energy in the singlet and triplet spin states. The probability of spin-crossing due to spin-orbit coupling is known to be almost 100% for this system,[17] therefore the highest energy along the true spin-coupled pathway was found by subtracting the spin-orbit coupling energy (4.6 kcal/mol) estimated from values reported in the literature[36] from the crossing point of the two fixed spin pathways. Additional details on this method can be found in our previous study of this subject.[17] For the reaction barriers of allyl alkoxide to acrolein and allyl alkoxide plus ammonia to allylamine, the initial and final states had the same spin state (doublet), so spin-crossing calculations were not necessary. For both of these pathways, the Climbing Image NEB method, optimized until the forces on each atom were less than 0.5eV/Å, was used to find the transition state.[37]

We also performed a few bond dissociation energy (BDE) and gas phase free energy calculations using the Q-Chem simulation package, version 4.3.2.[38] Both types of calculations were performed using the ωB97X-D functional and the 6-311++G(3df,3pd) basis set for final energy values.

3. Results and discussion

3.1 Catalyst active site

Figure 2.1 depicts a section of top layer of the (010) surface of $Bi_2Mo_3O_{12}$ from our optimized slab model, with relevant distances indicated. The highlighted **A** and **B** sites are both oxygen atoms formally doubly-bonded to molybdenum cations and perturbed electronically[17] by neighboring bismuth atoms. Since previous work found that unperturbed molybdenyl oxo groups are less active than Bi-perturbed ones, and that bismuth-molybdenum bridging oxygen sites are even less active than either Mo-oxo species,[17] we did not consider reaction at any other sites. However, since site **A** is slightly closer to the nearby bismuth than site **B** (2.80 Å and 2.99 Å respectively) and thus has a stronger electronic perturbation, site **A** is the most active surface site and was used as the primary site for our calculations.

As indicated in Figure 2.1a, sites **A** and **B** repeat in the order **A-B-A-B** etc. in a line on the (010) surface. As the oxo groups distort to the side to reduce the repulsive interaction with the bismuth lone pair, one **A-B** pair gets closer together while the other pair gets farther apart (3.25 Å and 5.12 Å respectively) on the surface optimized at 0 K. At reaction temperatures, the exact location of each oxo group will fluctuate, but each one will always have two neighboring oxo species 3-5 Å away. We invoke the involvement of two sites for many of the reactions below, since this 3-5 Å gap is small enough that the hydrocarbon can easily span it. One unit cell of $Bi_2Mo_3O_{12}$ contains one **A** and one **B** surface site, plus one bridging molybdenum site, such that there are three molybdenum atoms and two bismuth atoms at the surface. To depict our proposed mechanisms, we use a top-down view representation of the unit cell surface with the

primary **A** site indicated in black and the secondary neighboring **B** site in grey (see Fig. 2.1b). Since the unit cell model is periodic, the secondary **B** site used for calculations that require two sites is actually both on the close (3.25 Å) side and on the far (5.12 Å) side of the primary **A** site.
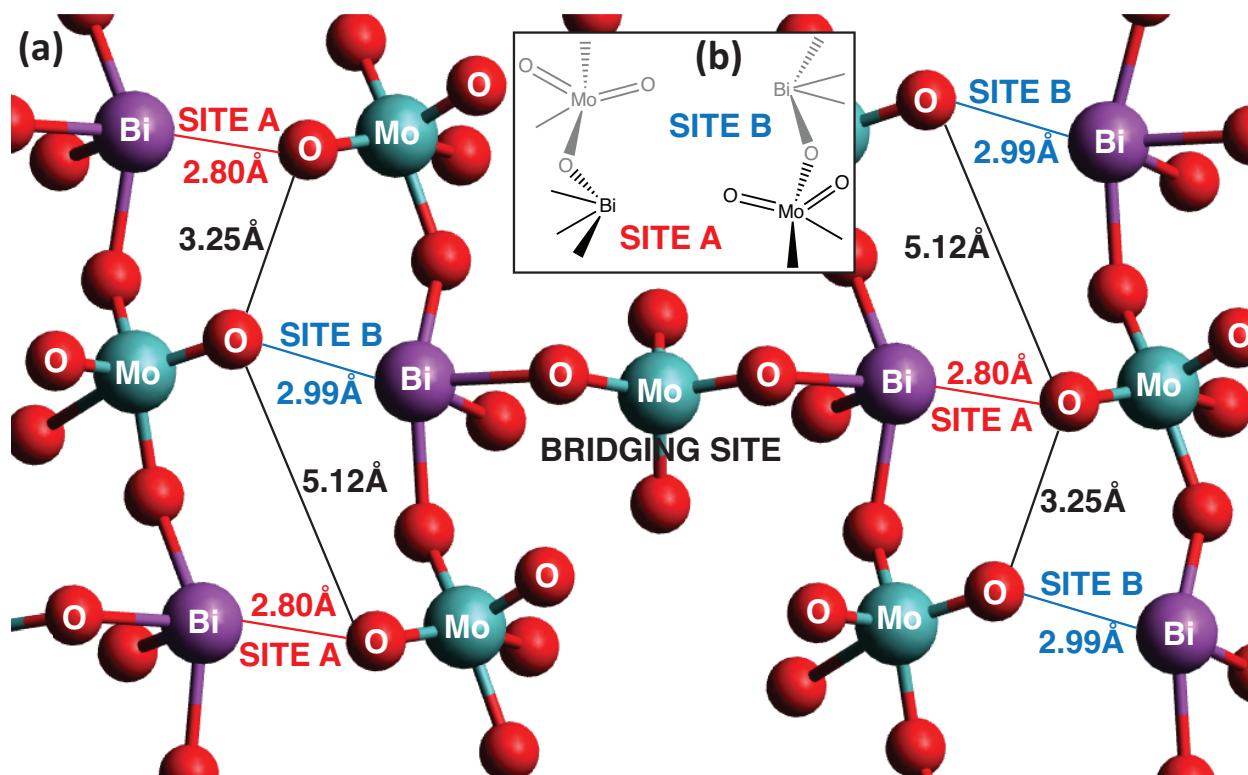

Fig. 2.1 (a) Top-down view of the top layer of optimized (010) surface of $Bi_2Mo_3O_{12}$, with relevant distances indicated in Å and the key **A** and **B** sites labeled. All red spheres represent oxygen atoms, but only those marked with an "O" are at the surface. (b) Simplified representation of the same surface used in the rest of this paper.

3.2 Catalyst reoxidation

During propene (amm)oxidation, hydrogen atoms are removed from propene and from ammonia by the catalyst, resulting in reduction of the catalyst surface. In order to complete the catalytic cycle, pairs of hydrogen atoms must combine with oxygen atoms generated by dissociation of molecular oxygen in order to release water. Previous authors have assumed that all hydrocarbon conversion steps occur before the catalyst surface in reoxidized in the final step of the catalytic cycle. However, this way of viewing the reaction mechanism is not chemically plausible, since, as discussed below, experiments show that the catalyst is reoxidized at rate that is much faster than the rate of reduction. Additionally, assuming that reoxidation occurs at the end of all steps leading to products is unrealistic for calculations of propene ammoxidation to acrylonitrile over a $Bi_8Mo_{12}O_{48}$ unit cell, which only has four surface molybdenyl oxo units (only two of which are the most active bismuth-perturbed oxos) on which to put H atoms. During propene ammoxidation, six H atoms are removed from propene and ammonia (3 from each

reactant), and consequently there are simply not enough low energy locations on one unit cell to store all of the liberated H atoms without intervening water desorption and reoxidation.

XANES experiments indicate that even under extreme reducing conditions (exposure to 1 bar propene for 24 h at 713 K) only molybdenum is reduced and only to Mo^{4+}, and that under standard propene oxidation conditions ($O_2/C_3H_6 = 1$ and T = 713 K) both metals remain in their highest oxidation state.[7] Previous studies have shown that the rate of propene consumption during both oxidation and ammoxidation is independent of the oxygen pressure, as long as it is supplied at stoichiometric or higher concentrations. These observations indicate that the rate of catalyst reoxidation by oxygen is faster at these conditions than the rate of catalyst reduction by propene.[4,8,39] Moreover, experiments conducted in the absence of oxygen demonstrate that, for a short period of time, the rate of propene oxidation is the same whether or not oxygen is provided, indicating that highly mobile O^{2-} ions can migrate to the surface from the bulk of the catalyst and participate in reactions.[40,41,42] The participation of lattice oxygen atoms is further supported by experiments in which a mixture of $^{16}O_2$ and $^{18}O_2$ is fed over bismuth molybdate and no evidence is found for $^{16}O^{18}O$ formation, indicating that dissociation of gas-phase oxygen is favorable and irreversible.[43] Taken together, these observations lead to the conclusion that, under standard reaction conditions with a feed containing at least a stoichiometric concentration of oxygen, the catalyst surface is very close to being completely oxidized and that surface oxygen atoms are highly mobile and can react with hydrogen atoms produced by the cleavage of C-H or N-H bonds to generate water.

Therefore, in all our calculations, as soon as a hydrogen atom is liberated from propene or ammonia, it is removed in a reoxidation step involving ¼ O_2 to produce ½ H_2O. Leaving the H atom on the surface until another H is liberated not only blocks the only adjacent H abstraction site competent to do chemistry, but results in an unphysical situation in which $^1/_3$ of the surface of molybdenum cations are reduced. Continuing to perform reactions on partially reduced surfaces becomes more and more unfavorable. In order to assure that all calculations relate to a fully oxidized surface, as indicated by experimental results, we immediately remove released H atoms to mimic the experimentally-observed rapid reoxidation of the catalyst.

3.3 Relevant hydrogen bond dissociation energies

Table 2.1 shows the DFT-calculated C-H, N-H and O-H bond dissociation energies (BDEs) for a number of gaseous species relevant to the chemistry of propene oxidation and ammoxidation catalysis. The BDE is the difference between the sum of the energy of a hydrogen radical and the optimized remaining radical fragment and the energy of the optimized parent molecule. The entries shown in black represent C-H bonds that appear to be weak enough to be broken by $Bi_2Mo_3O_{12}$ in the course of propene oxidation and ammoxidation, while the entries shown in red represent C-H and N-H bonds that appear to be too strong to be directly broken by the catalyst. The BDE cutoff for $Bi_2Mo_3O_{12}$ seems to be ~94 kcal/mol, since the C_1-H bond of propene (BDE = 92.7 kcal/mol) is broken in the rate-limiting step, but acrolein, which has a C_1-

H bond that is only slightly stronger (BDE = 95.3 kcal/mol) is a stable product during propene oxidation. Were $Bi_2Mo_3O_{12}$ able to abstract this hydrogen of acrolein, it would only be an intermediate to a more highly-oxidized final product. Thus materials that have stronger H abstraction sites than $Bi_2Mo_3O_{12}$, such as $BiVO_4$,[7] have a low activation energy for propene activation but are unselective and mostly combust propene all the way to CO_x, while those with weaker H abstraction sites, such as $PbMoO_4$,[44] are not able to activate propene to begin the reaction. The relevance of bond dissociation energies is also supported by our prior work on the reactivity of different hydrocarbons (propane, propene, 1-butene, 2-butene and isobutene) over $Bi_2Mo_3O_{12}$, which showed a correlation between the strength of the weakest C-H bond and the apparent activation energy of that compound in either oxidative dehydrogenation or partial oxidation.[45]

| Molecule	BDE [kcal/mol]			
	C_1–H	C_2–H	C_3–H	N–H or O-H
$C_3H_2=C_2H-C_1H_3$ Propene	92.7	114.2	119.3	--
$C_3H_2=C_2H-C_1H_2-OH$ Allyl alcohol	85.1	115.0	117.4	(O-H) 111.1
$C_3H_2=C_2H-C_1H=O$ Acrolein	95.3	118.4	118.0	--
$C_3H_2=C_2H-C_1H_2-NH_2$ Allylamine	82.3	114.9	117.8	(N-H) 106.4
$C_3H_2=C_2H-C_1H=NH$ 2-propen-1-imine	102.1	109.9	117.7	(N-H) 96.7
$C_3H_2=C_2H-C_1\equiv N$ Acrylonitrile	--	111.2	119.5	--
$C_2H_3-C_1\equiv N$ Acetonitrile	--	101.9	--	--
$HC_1\equiv N$ Hydrogen Cyanide	135.2	--	--	--
$C_3H_2=C_2H-C_1H(-OH)(-NH_2)$ 2-propen-1-ol-1-amine	80.6	116.2	117.3	(N-H) 109.0 (O-H) 111.8
$C_3H_2=C_2H-C_1H(-OH)(=NH)$ 2-propen-1-ol-1-imine	--	116.5	117.3	(N-H) 109.6 (O-H) XX
$C_3H_2=C_2H-C_1(=O)(-NH_2)$ Acrylamide	--	114.2	117.1	(N-H) 117.5
NH_3 Ammonia	--	--	--	(N-H) 114.1

Table 2.1. Gas phase bond dissociation energies

3.4 Propene oxidation to acrolein

The proposed elementary steps and corresponding energy profile for propene oxidation to acrolein are shown in Scheme 2.1 and Figure 2.2, respectively. In agreement with experiment, the initial activation of propene to form a physisorbed allyl radical (steps **0 → 3**) is rate-limiting and is common to propene oxidation and ammoxidation routes. The subsequent steps (**3 → 8**) are very similar to those that proposed in previous studies.[7,17,20]

The first step (**0 → 1**) is propene physisorption. Previous DFT work has reported an internal energy of adsorption over the (010) surface of $Bi_2Mo_3O_{12}$ to be -4.4 kcal/mol; however, that value is for a non-specific van der Waals adsorption above the space between sites **A** and **B**.[16] We have since found that the strongest propene adsorption site is directly over a surface Bi^{3+} atom at a distance of 3.33Å from the center of the double bond. In this adsorption mode, the pi-bonding electrons from the double bond of propene donate electron density to the large, unoccupied orbitals of the under-coordinated Bi^{3+} via a dative type interaction, resulting in a calculated internal energy of adsorption of -11.5 kcal/mol. For comparison, the experimental value for the enthalpy of adsorption of propene on bismuth molybdate is ~8 kcal/mol.[46]

The second step (**1 → 2**) is the abstraction of a hydrogen atom from the methyl group of propene by a bismuth-perturbed molybdenyl oxo. This key step has been previously investigated and has been found to involve a singlet-triplet spin crossing transition state.[16,17] The reaction pathway starting from propene adsorbed over a neighboring Bi^{3+}, including the spin-singlet, spin-triplet and spin-coupled energy landscapes and geometries for the initial, spin crossing, and final state, is shown in Figure 2.3. From its lowest energy adsorbed state, the propene moves parallel to the surface towards the molybdenyl oxo and passes over the hydrogen, then moves back to re-establish a dative interaction between the newly formed allyl radical and the bismuth cation. After subtracting the spin-orbit coupling energy from the spin-crossing point to attain the reaction pathway transition state, the value of ΔE_{TS} is found to be 38.9 kcal/mol. However, at reaction temperatures of ~673 K, the catalyst resting state is the bare catalyst surface; therefore, the propene adsorption energy is subtracted from the transition state energy to obtain an apparent activation energy of 27.3 kcal/mol (see Fig. 2.3). This value of the apparent activation barrier for the rate-limiting step is reasonably close to that measured experimentally for propene oxidation or ammoxidation (22 kcal/mol)[4].
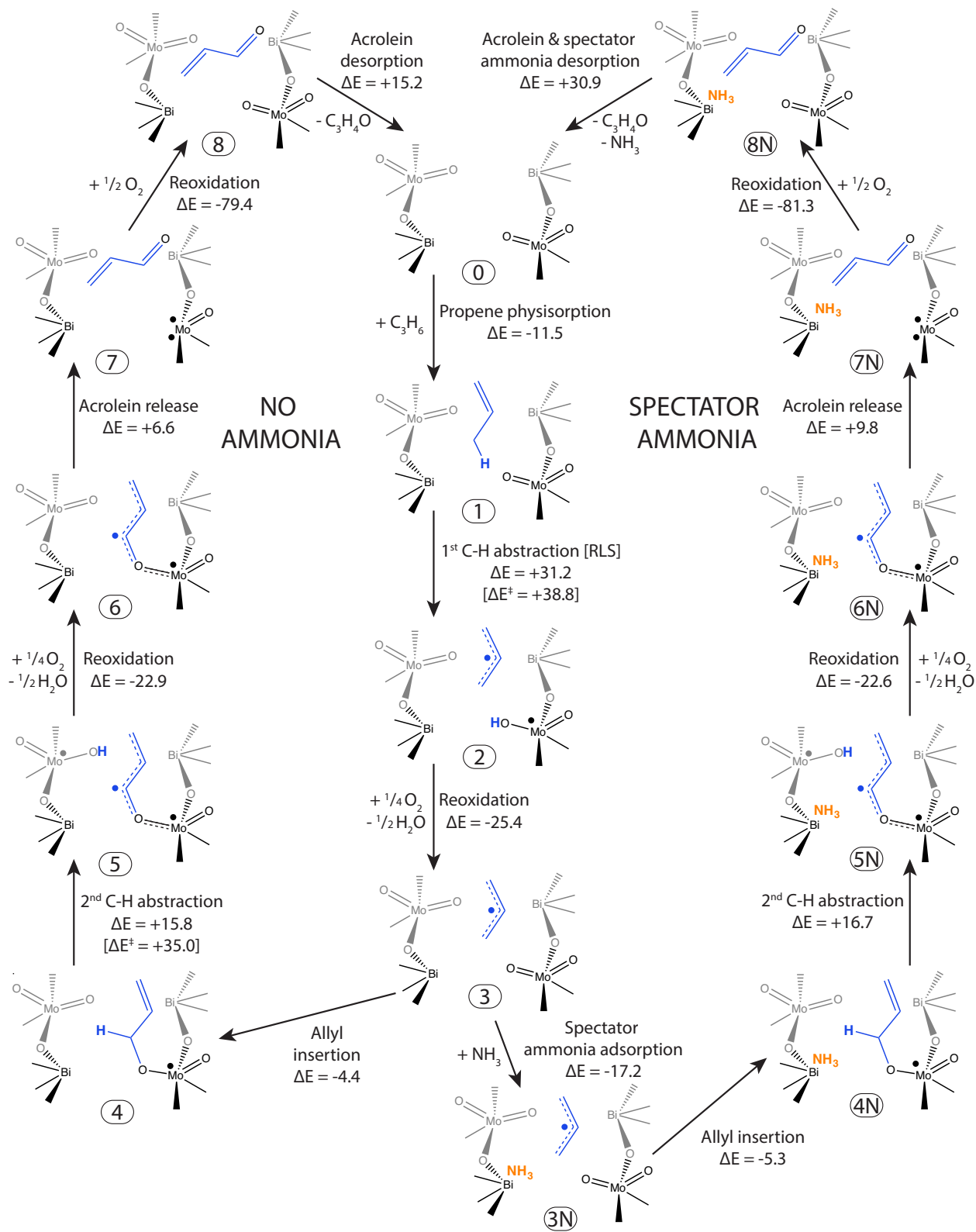
Scheme 2.1. Proposed elementary steps for propene oxidation to acrolein (ΔE in kcal/mol).
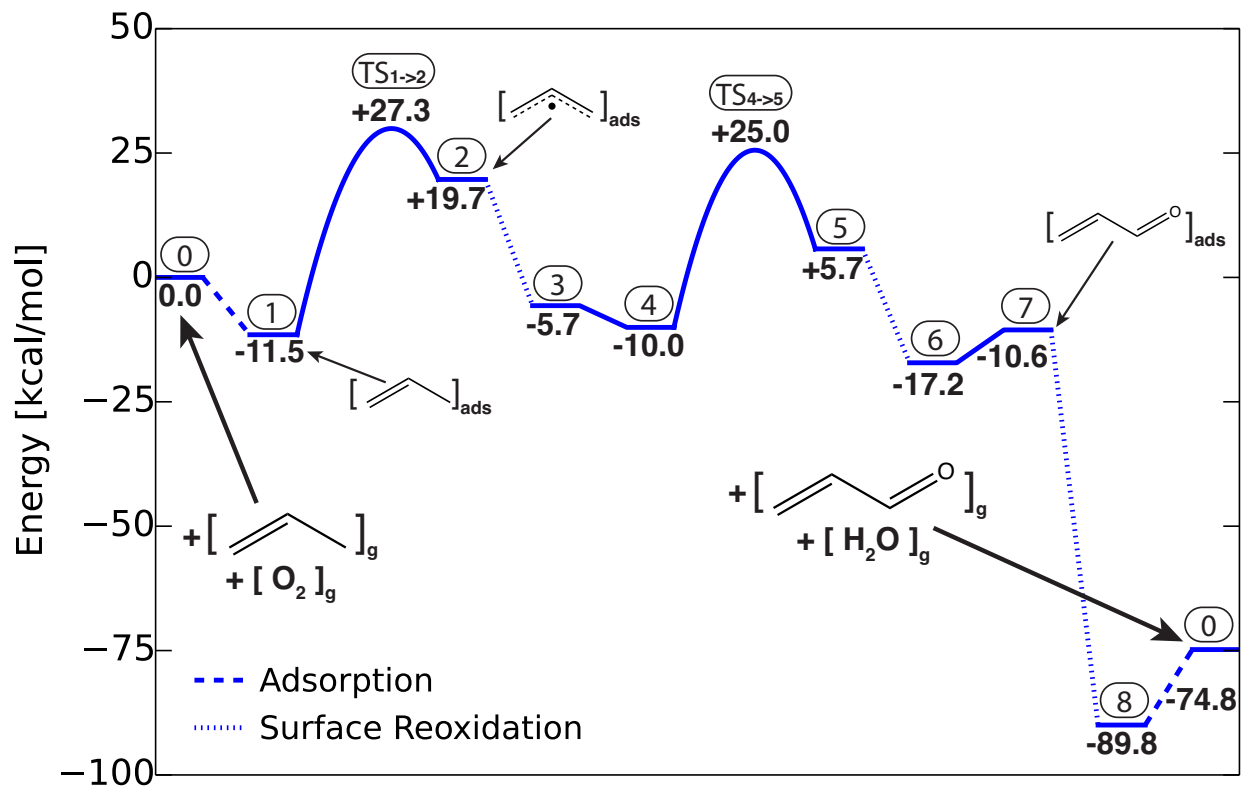
Fig. 2.2 Energy landscape for propene oxidation to acrolein. Encircled integers refer to structures in Scheme 2.1, bold numbers give the energy of each structure relative to the initial state.

The overall energy of reaction, ΔE_{rxn}, is very similar to the value of ΔE_{TS}, since the final state contains a high-energy radical species. In fact, we can see from the geometries on the right side of Figure 2.3 that the transition-state geometry is very similar to the final-state geometry, with the molybdenum-oxygen bond highly elongated, the oxygen-hydrogen bond almost completely formed, the carbon-hydrogen bond already completely broken and the two carbon-carbon bonds of almost equal length. Consistent with the DFT-calculated final state **2**, experimental studies have shown that acrolein produced from 1-^{13}C-propene contains a 50/50 mixture of ^{13}C label in both terminal C positions of the product,[12] demonstrating that a free allyl species is produced is produced as an intermediate that can then react with equal probability at either end. While it appears that this reaction could easily go backward via **2 → 1**, this is unlikely to occur because of the rapid and highly exothermic water desorption and catalyst reoxidation. As is clear from Figure 2.2, the catalyst reoxidation to remove the hydrogen atom and leave an allyl radical over an oxidized surface (**2 → 3**) provides the thermodynamic driving force for propene activation.
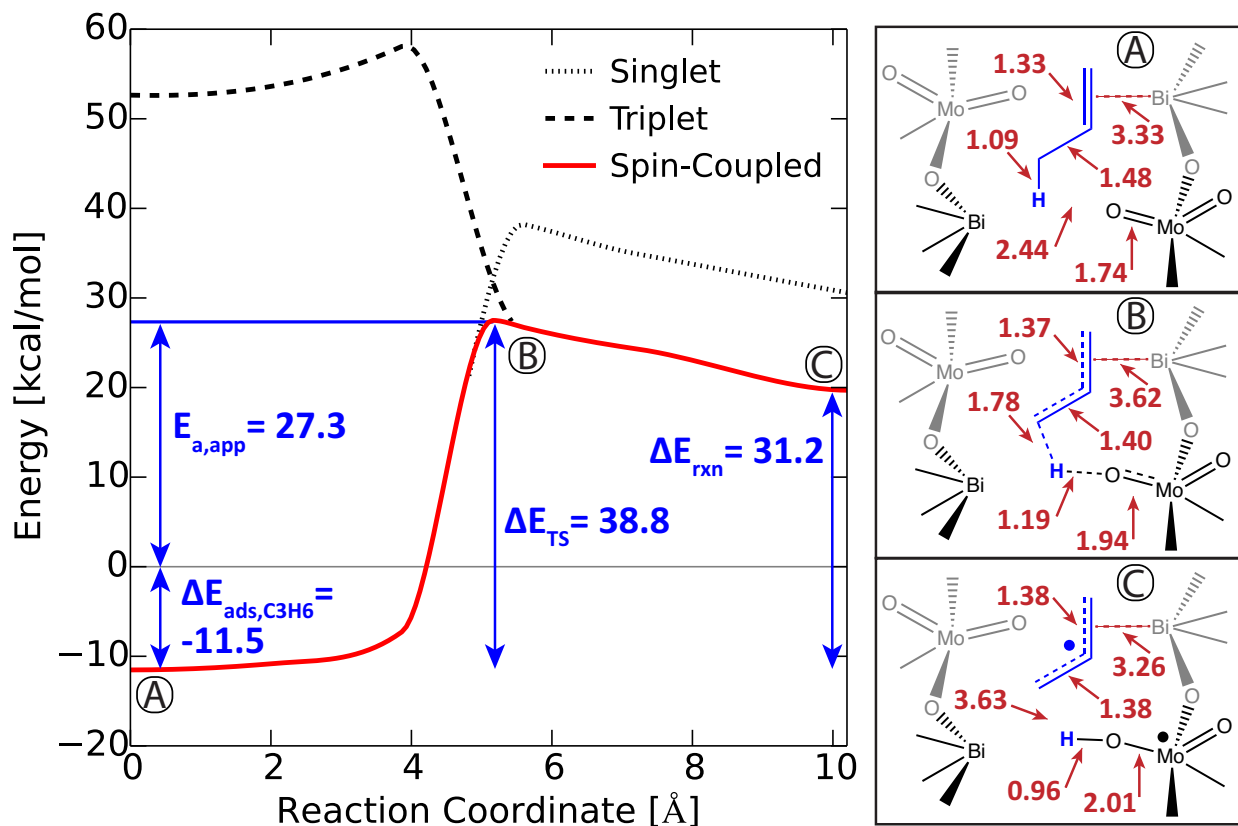
Fig. 2.3 Optimized spin-crossing reaction barrier for initial hydrogen abstraction from propene, with relevant energies annotated. Geometries for the initial state (A), spin-crossing transition state (B) and final state (C) are shown on the right, with relevant distances in Å indicated.

The next step ($3 \rightarrow 4$) is the insertion of allyl into a Mo=O bond to create an energetically-favored surface allyl alkoxide species. Experimental studies conducted with $^{18}O_2$ in the gas phase have shown that the O in the product acrolein comes from the catalyst surface, and not from gas phase oxygen;[41] therefore, the C–O bond formed in step $3 \rightarrow 4$ remains in the final product. Considering the bond distances given in Table 2.2, we see that the allyl species (3) shares one unpaired electron among the three carbon atoms, resulting in two ~1.5 order bonds, while in 4, there is a clear terminal C_2-C_3 double bond and single bonds between Mo and O, O and C_1, and C_1 and C_2.
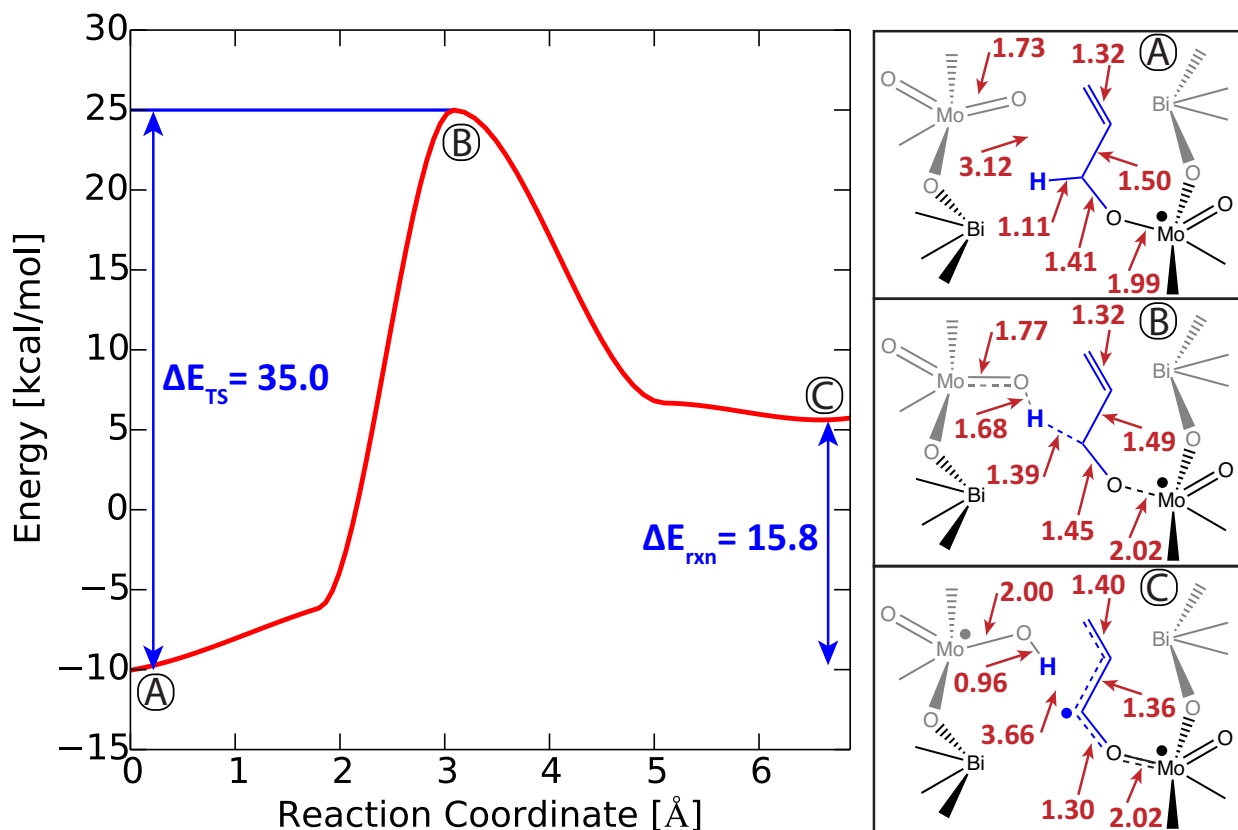
Fig. 2.4 Optimized reaction barrier for hydrogen abstraction from allyl alkoxide to produce coordinated acrolein, with relevant energies annotated. Geometries for the initial state (A), transition state (B) and final state (C) are shown on the right, with relevant distances in Å indicated.

The subsequent step ($4 \rightarrow 5$) is the next most energetically-demanding step after the initial, rate-limiting step of propene activation step, and involves abstraction of an H atom from the allyl alkoxide species by a neighboring $O=Mo^{6+}=O$ group to produce Mo-coordinated acrolein and a reduced neighboring site. This hydrogen abstraction has previously been proposed by Burrington et al.[20] and by Getsoian et al.[17] to occur via reaction with the other oxo group bound to the same molybdenum as the allyl alkoxide. However, our calculations show that the energy of this final structure (C_3H_4O-Mo^{4+}-OH) is 5 kcal/mol higher in energy than the final structure for hydrogen abstraction by a neighboring oxo group (C_3H_4O-$Mo^{5+}=O$ and $O=Mo^{6+}$-OH). Since the neighboring $O=Mo^{6+}=O$ group is close enough for the reaction to occur, we consider **5** to be the preferred end state. The reaction barrier energy and geometries are shown in Figure 2.4.

As is clear from Figure 2.4, abstraction of a hydrogen atom from allyl alkoxide to produce an adsorbed acrolein is quite difficult, and the value of ΔE_{TS} for this step is only slightly lower than that for the initial hydrogen abstraction from propene. While the BDE for allyl

45

alcohol (see Table 2.1), which is an approximation of the allyl alkoxide species where the surface Mo is replaced by H, is relatively low, the transition state is geometrically constrained since the hydrocarbon remains bound to the surface during reaction. From the bond distances shown in Figure 2.4, we see that, during the reaction pathway, the allyl alkoxide fragment undergoes significant geometric distortion in order to move closer to the neighboring molybdenyl oxo group and vice versa. When hydrogen is transferred in the transition sate, the allyl alkoxide is still essentially intact with bond distances similar to those in the reactant state. However, the final state after hydrogen abstraction has all partial bond distances (Table 2.2), demonstrating that there is electron delocalization across the entire acrolein fragment from molybdenum through the terminal carbon. There are formally three unpaired electrons in the final state as indicated in Figure 2.4, but only the one unpaired electron on the Mo that just abstracted the hydrogen atom from allyl alkoxide is isolated. The other two electrons can pair with the electrons in the carbon-carbon double bond or in the oxygen lone pairs to form the resonance structures Mo*–O–C_1*–C_2=C_3, Mo*–O–C_1=C_2–C_3*, Mo*–O*=C_1–C_2=C_3 or Mo=O*–C_1=C_2–C_3*, where * indicates an unpaired electron. Therefore, these two electrons on the acrolein species are actually paired and the lowest energy spin state of **5** is a doublet, not a quadruplet (only unpaired electron on the Mo with the newly formed hydroxyl). This is true for the reacting species over the entire reaction trajectory from **4** → **5**, which remains in the doublet spin state with only one unpaired electron.

Unlike the initial rate-limiting hydrogen abstraction, in the reaction of **4** → **5** the final state is significantly lower in energy than the transition state. This is because the radical species remaining after hydrogen abstraction is significantly stabilized by the bonding to oxygen and molybdenum that allows significantly more electron delocalization that is possible across the three carbon atoms of the free allyl radical. Reoxidation of the H abstraction site in **5** produces structure **6**, which still has electron delocalization across the entire acrolein fragment resulting in partial order bonds (see bond distances in Table 2.2).

In Structure **7**, the product has disassociated from the molybdenum to generate adsorbed acrolein with a fully formed carbon-oxygen double bond and a reduced Mo^{4+}=O site. Acrolein adsorbs quite favorably at Bi^{3+} cations via electron donation from one of the lone pairs on oxygen to the under-coordinated bismuth cation. The reaction of **6** → **7** requires substantial rearrangement of the oxygen atoms around molybdenum, which is in a triplet state with an unpaired electron in each of two distinct d orbitals. Formation of **7** is energetically uphill and, as suggested by Pudar et al.;[23] may be facilitated by simultaneous molecular oxygen adsorption to displace the acrolein and maintain the molybdenum in a high oxidation state. However, we find that interaction with O_2 is not required for reasonable reaction energies (Figure 2.2). The oxygen vacancy in **7** created upon acrolein formation is then restored by atomic oxygen to form Structure **8**; however, we did not attempt to elucidate the details of this process. As observed in Figure 2.2, this step (**7** → **8**) is extremely favorable thermodynamically.

| Structure #	Mo–O distance (Å)	O–C$_1$ distance (Å)	C$_1$–C$_2$ distance (Å)	C$_2$–C$_3$ distance (Å)
3	1.74 *B.O. = 2*	*No bond*	1.38 *B.O. = 1.5*	1.37 *B.O. = 1.5*
4	2.00 *B.O. = 1*	1.41 *B.O. = 1*	1.49 *B.O. = 1*	1.33 *B.O. = 2*
5	2.02 *B.O. = 1*	1.30 *B.O. = 1.5*	1.36 *B.O. = 1.5*	1.40 *B.O. = 1.5*
6	2.03 *B.O. = 1*	1.28 *B.O. = 1.5*	1.41 *B.O. = 1.5*	1.35 *B.O. = 1.5*
7 & 8		1.21 *No bond* *B.O. = 2*	1.45 *B.O. = 1*	1.33 *B.O. = 2*

Table 2.2. Bond distances and formal bond orders (*B.O.*) from optimized structures **3**-**8**.

The final step in propene oxidation is desorption of acrolein from the catalyst surface, thereby regenerating the bare surface (**0**). As mentioned in Section 3.3, acrolein has a C-H bond that is likely just slightly stronger than what can easily be broken by $Bi_2Mo_3O_{12}$, and is therefore reasonably stable to subsequent oxidation. We do observe high conversion of acrolein and ammonia to acrylonitrile (see Section 3.7), but this reaction must be facilitated by ammonia, since acrolein is not observed to undergo further oxidation at 673 K over $Bi_2Mo_3O_{12}$ without ammonia present.[4]

3.5 Propene ammoxidation to acrylonitrile

Scheme 2.1 shows the pathway for propene oxidation to acrolein in the presence of a spectator ammonia molecule (structure numbers are the numbers for the same structure without ammonia followed by an "N"). The energies for this pathway are shown in Fig. 2.5 so that they can be compared with those for the propene ammoxidation to acrylonitrile pathway shown in Scheme 2.2. In agreement with experiment, and as already discussed in Section 3.4, the activation of propene to produce allyl radical (steps **0** → **3**, see Fig. 2.2) is common to all product pathways.[9,20]

As proposed in our recent experimental work, we hypothesize that C-N bonds are formed by reaction of allyl alkoxide species with adsorbed ammonia.[4] Ammonia adsorbs favorably on surface Bi^{3+} cations via sigma donation from the lone pair of nitrogen to empty bismuth 6p orbitals. Using our periodic $Bi_8Mo_{12}O_{48}$ slab model, we calculate the energy of ammonia adsorption over Bi^{3+} to be -17.9 kcal/mol on a fully oxidized surface. Since the 6p orbitals of bismuth are very large and diffuse, we observe that ammonia can be anywhere in a ~2Åx2Å area, as long as the nitrogen lone pair points toward a Bi^{3+} that is 2.6-3.0Å away, and have approximately the same energy of adsorption. We find that adsorption of ammonia next to an adsorbed allyl (**3** → **3N**) is essentially equivalent to ammonia adsorption on a bare catalyst surface (-17.2 vs. -17.9 kcal/mol).
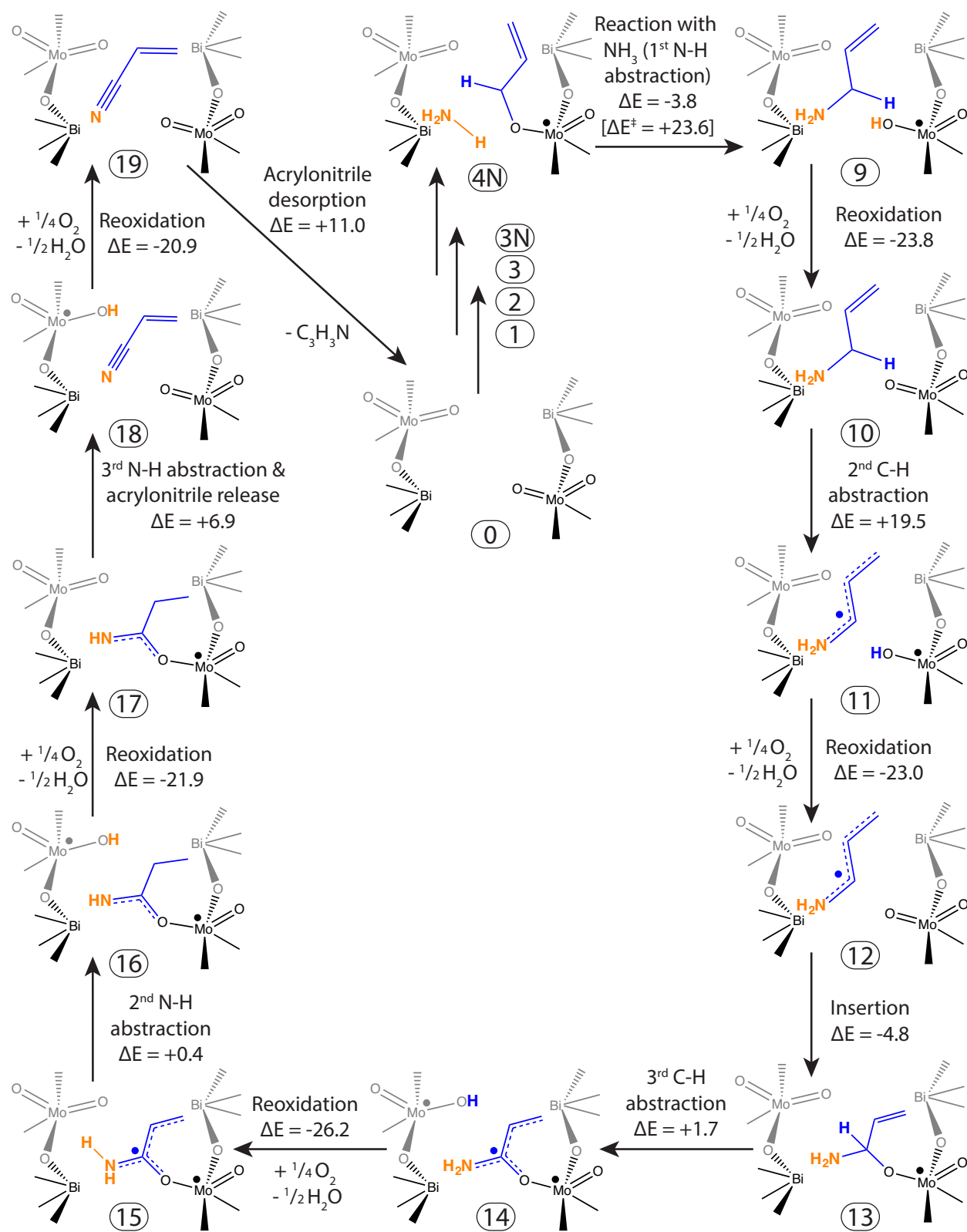
Scheme 2.2. Proposed elementary steps for propene ammoxidation to acrylonitrile (ΔE in kcal/mol).
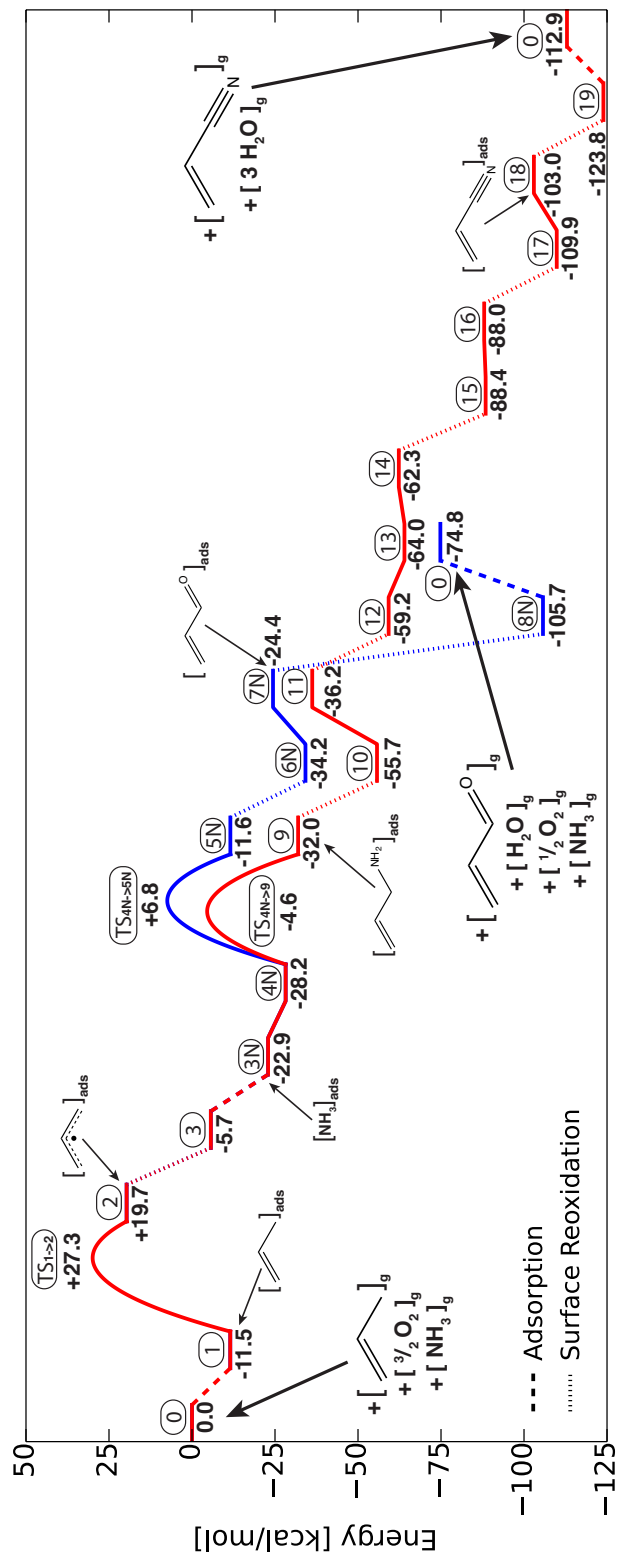
Fig. 2.5 Energy landscape for propene ammoxidation to acrylonitrile. Encircled integers refer to structures in Scheme 2.2, bold numbers give the energy of each structure relative to the initial state.

As suggested by our experimental work,[4] we propose that reaction of allyl alkoxide species with adsorbed ammonia in structure **4N** produces allylamine, which then undergoes further reaction to form acrylonitrile (or acetonitrile and HCN). In the schemes, we indicate that ammonia adsorbs on structure **3** to form **3N**, which then undergoes allyl insertion to form **4N**; however, ammonia could also adsorb after insertion to form **4N** directly from **4** or could already be present before the allyl radical is formed. Additionally, while we indicate that ammonia is adsorbed on the Bi^{3+} cation that perturbs the allyl alkoxide oxygen, ammonia could also adsorb on either of the two neighboring Bi^{3+} sites to either side of the allyl alkoxide species, since they are also close enough to allow reaction between the ammonia and the allyl alkoxide species.

The allyl alkoxide intermediate (**4N**) can undergo one of two competing processes – abstraction of an H atom to form adsorbed acrolein and a neighboring Mo-OH group (**5N**) or reaction with adsorbed ammonia to form adsorbed allylamine and a Mo-OH group (**9**). The activation barrier for **4** → **5** was discussed in detail in Section 3.4 (see Fig. 2.4). We did not recalculate the activation barrier when a spectator ammonia molecule in adsorbed, but as can be seen by comparing the left and right sides of Scheme 2.1, the presence of a spectator ammonia does not have a significant effect on the values of $\Delta E_{reaction}$. Since the adsorbed ammonia does not lie along the **4** → **5** reaction pathway, but rather is located off to the side of the hydrocarbon, its presence should not affect the reaction barrier and therefore we assumed that ΔE_{TS} for **4N** → **5N** is the same as for **4** → **5**.

Our calculated potential energy for reaction of the allyl alkoxide species with ammonia to form allylamine is shown in Figure 2.6. We found ΔE_{TS} to be 23.6 kcal/mol and $\Delta E_{reaction}$ to be -3.8 kcal/mol. The initial movement along the reaction pathway involves detachment of the allyl species, converting **4N** back to **3N**, so that the allyl species in **3N** is favorably adsorbed above the bismuth cation. This part of the pathway accounts for the section of the reaction coordinate between 0 Å and 5 Å in Figure 2.6. We found that the interaction between allyl and bismuth cation leads to a significantly lower reaction barrier than for the same pathway in which the allyl radical is further above the surface and thus not able to interact with the bismuth cation. The transition state for reaction **4N** → **9** is the umbrella flip of ammonia, which removes the favorable lone pair interaction with the surface bismuth cation and forms a less favorable interaction with the electrophilic carbon of the allyl species. After the ammonia inverts, formation of the C-N bond followed by loss of a hydrogen atom to a surface molybdenyl oxo to form allylamine is highly exothermic. This reaction is a nucleophilic substitution reaction that most likely occurs by interaction of ammonia with an allyl cation to form allyl-NH_3^+ that then loses a proton to the oxygen anion to form allylamine. Once the allyl-NH_3^+ species loses a proton to the molybdenyl oxo, the nitrogen of allylamine can reform the favorable interaction with the surface bismuth cation that was lost in the transition state. The allylamine formed in reaction **4N** → **9** has the lowest adsorption energy of any species we investigated (ΔE_{ads} = -23.7 kcal/mol) because it has favorable, dative-type interactions from both the nitrogen lone pair and the carbon-carbon pi bond to two neighboring bismuth cations.

Overall, the activation barrier for allylamine formation is reasonably low because ammonia is stabilized by interaction with the carbon atom of the allyl species before it loses a hydrogen atom. As can be seen in Table 2.1, the N-H bonds of ammonia are significantly stronger than the C-H bond of the methyl group of propene that is broken in the rate-limiting step. We examined alternative pathways for the interaction of ammonia with various hydrocarbon intermediate species, but found that, because of the high bond dissociation energy of the N-H bonds of NH_3, any reaction step that began with abstraction of an H atom from ammonia was not favorable. From this we conclude that ammonia can only be activated by $Bi_2Mo_3O_{12}$ once the nitrogen fragment that will be formed upon hydrogen abstraction is first stabilized by favorable interaction with either the catalyst surface or a hydrocarbon species.
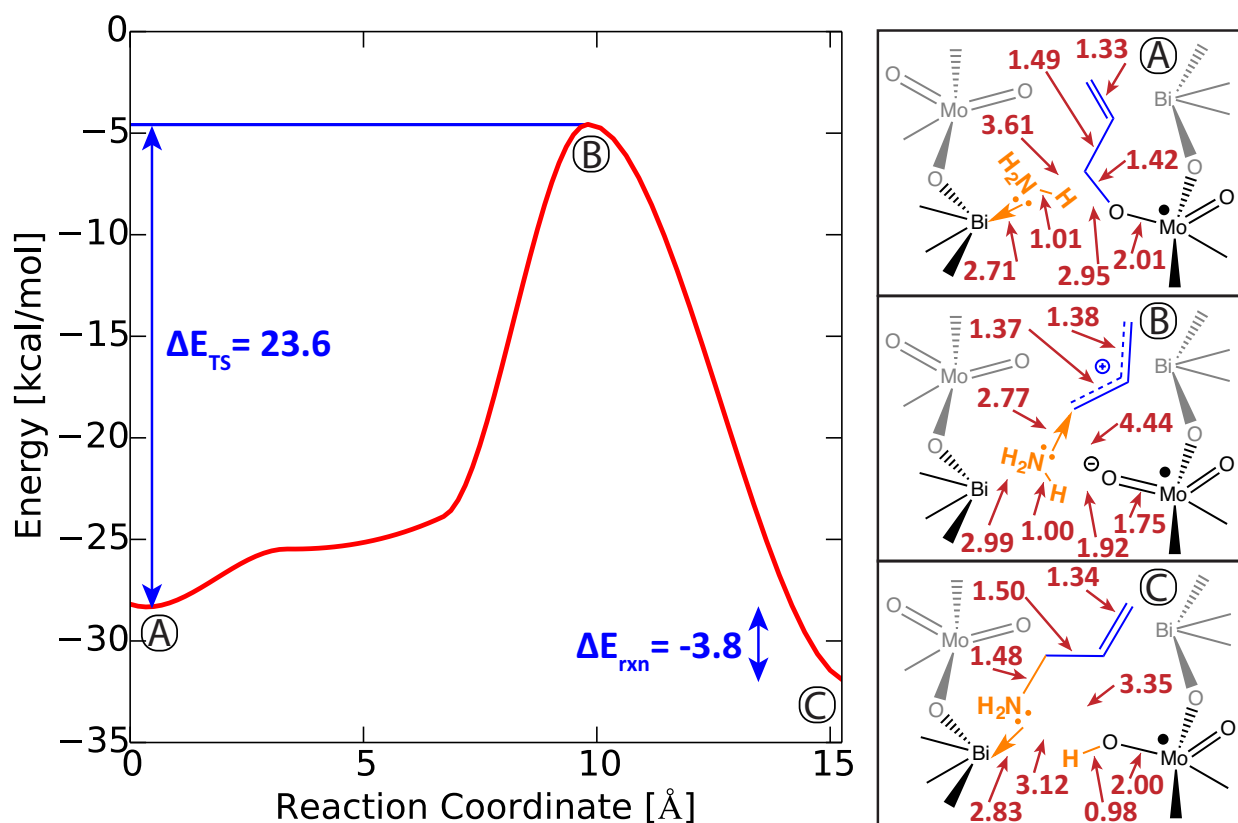
Fig. 2.6 Reaction barrier for reaction of allyl alkoxide and ammonia to produce adsorbed allylamine, with relevant energies annotated. Geometries for the initial state (A), transition state (B) and final state (C) are shown on the right, with relevant distances in Å indicated.

Comparing the reaction barrier of **4N → 9** with **4N → 5N**, it is clear that production of allylamine is energetically favored by more than 10 kcal/mol over production of acrolein when a neighboring ammonia molecule is present. The transition state for allylamine formation is also likely to be entropically favored over the transition state for acrolein formation, since the former has two separate physisorbed molecules that have not yet come together in the transition state

(see Fig. 2.6), whereas the latter is geometrically-constrained as the bound molecule stretches to a neighboring site (see Section 3.4 and Fig. 2.4). Therefore, at reaction temperatures, if an ammonia molecule adsorbs at any of the three bismuth cations near an allyl alkoxide species, allylamine will be produced. However, acrolein can still be formed via reaction **4** → **5** if ammonia is not adsorbed nearby. The ratio of acrylonitrile to acrolein is therefore only dependent on the ammonia coverage, which is a function of ammonia pressure to the first order in this low coverage regime. Experimentally, we have observed that the ratio of acrylonitrile to acrolein is approximately first-order in ammonia pressure and we have estimated from a kinetic model regressed to selectivity data that the activation barrier for acrolein formation is 15±5 kcal/mol higher than the barrier height for acrylonitrile formation from the common intermediate.[4] In summary, our DFT calculations for steps **4N** → **5N** and **4N** → **9** are consistent with the difference in the activation energies that we determined from analysis of the reaction kinetics.[4]

As discussed in Section 3.2, once H atoms are abstracted from a reacting species onto the catalyst surface, the catalyst is reoxidized, e.g., step **9** → **10 11** → **12**, **14** → **15**, **16** → **17**, and **18** → **19** (all indicated in Fig. 2.5 by hashed lines). These steps allow the overall conversion to occur, since all the hydrocarbon conversion steps are endothermic or thermoneutral and thus would eventually become too high in energy were they not balanced by the more exothermic reoxidation steps.

Allylamine has two relatively weak C-H bonds (see Table 2.1 for BDEs) and should thus undergo facile hydrogen abstraction. Since allylamine adsorbs quite strongly on the surface of $Bi_2Mo_3O_{12}$ via favorable electron donation from the nitrogen and from the carbon-carbon double bond to neighboring Bi^{3+} cations, it is unlikely to escape the reactor before undergoing subsequent reactions. Experimentally, we have observed a high conversion of allylamine when it is fed to the reactor under conditions where propene would only exhibit differential conversion, making it difficult to detect allylamine during propene ammoxidation.[4] The energy of reaction to abstract of one of the equivalent weak primary H atoms from allylamine (**10** → **11**) is ΔE = +19.5 kcal/mol, while the same value for abstraction of one of the equivalent primary H atoms from propene (rate-limiting step, **1** → **2**) is much higher at ΔE = +31.2. The energy for H abstraction from allylamine is much lower because resonance structures involving both the lone pair on the nitrogen atom and the carbon-carbon pi bond electrons stabilize the CH_2=CH-•CH-NH_2 radical (Structure **11**). It is evident from the bond distances given in Table 2.3 that the radical is delocalized across the entire fragment, resulting in all C-C and C-N bonds being 1.5 order.

Estimates of the activation barrier for reaction **10** → **11** suggest that this reaction has a singlet-triplet spin crossing transition state that is only a few kcal/mol higher in energy than the final state. A transition-state energy similar to the final-state energy is also observed for the initial hydrogen abstraction from propene (see Fig. 2.3). Therefore, because of the computationally-intensive nature of locating singlet-triplet crossing transition states, this reaction barrier was not fully optimized and is not presented here. However, since the difference between

the transition state and the final state in the rate-limiting hydrogen abstraction from propene (step $1 \rightarrow 2$) is only 7.6 kcal/mol, we expect that the very similar reaction of $10 \rightarrow 11$ has a transition state of ≤8 kcal/mol above the final state. Consequently, the activation of allylamine should be significantly less demanding (by approximately the 11.7 kcal/mol difference in their values of ΔE_{rxn}) than the activation of propene, and therefore will occur easily and not affect the overall rate of propene conversion.

We hypothesized initially that after the formation of the allyl-NH_2 radical ($10 \rightarrow 11$) and reoxidation of the catalyst surface ($11 \rightarrow 12$), one of the H atoms from the NH_2 group would be abstracted to form 2-propen-1-imine ($NH=CH-CH=CH_2$), a compound similar to acrolein. However, all attempts to react this species over our model surface resulted in very high values of $\Delta E_{reaction}$, due to the absence of any weak C-H or N-H bonds (see Table 2.1). We therefore considered an alternate mechanism, in which the allyl-NH_2 radical is first stabilized by insertion into a surface molybdenum-oxygen double bond ($12 \rightarrow 13$), thereby facilitating subsequent reactions. This reaction is the same as step $3 \rightarrow 4$ in the pathway for propene oxidation, except that the allyl species has a terminal -$CH-NH_2$ group instead of a terminal -CH_2 group. As can be seen in Table 2.3, reaction of the allyl-NH_2 fragment with a surface Mo=O group generates all integer bond orders, removing the resonance stabilization found in the free allyl.

The remaining alpha C-H bond in 13 is still quite weak compared to the allylic H of propene (see Table 2.1, approximated by 2-propen-1-ol-1-amine) and consequently its abstraction in step $13 \rightarrow 14$ is nearly thermoneutral. The resulting tertiary carbon radical is highly stabilized by conjugation. The electron delocalization among the nitrogen, primary carbon and oxygen atoms results in a lengthening of the molybdenum-oxygen distance such that it is no longer a single bond. Despite the possible resonance structures involving the carbon-carbon double bond, the bond distances listed in Table 2.3 indicate that substantial electron delocalization only occurs locally among the nitrogen, primary carbon, and oxygen atoms. The -ene group appears to be nearly completely formed, likely because the electron-withdrawing nitrogen and oxygen atoms are sufficient to stabilize the carbon radical. This step completes the necessary removal of the three H atoms from the methyl group of propene.

After reoxidation ($14 \rightarrow 15$), abstraction of one of the equivalent H atoms from the terminal NH_2 group occurs via another essentially thermoneutral process to form 16. As mentioned above and indicated in Table 2.1, N-H bonds are generally very strong and thus difficult to break. However, a hydrogen atom can easily be abstracted from 15, because doing so regenerates the lone pair on nitrogen as the bond count on that atom goes from 3.5 to 2.5 (see depiction in Scheme 2.2). This step is then followed by another reoxidation to form structure 17. The bond distances of Table 2.3 indicate that structures 16 and 17 have approximately 1.5 order bonds between the primary carbon and both nitrogen and oxygen, rather than the expected double bond to nitrogen and single bond to oxygen. These 1.5 order bonds to both nitrogen and oxygen are a result of both heteroatoms having lone pairs of electrons that can interact with the electrons on the primary carbon and the highly electrophilic oxygen pulling electron density from the -C=NH group.

Structure #	Mo–O distance (Å)	O–C$_1$ distance (Å)	C$_1$–N distance (Å)	C$_1$–C$_2$ distance (Å)	C$_2$–C$_3$ distance (Å)
10	1.75 *B.O. = 2*	*No bond*	1.48 *B.O. = 1*	1.49 *B.O. = 1*	1.32 *B.O. = 2*
11 & 12	2.01 *B.O. = 1*	*No bond*	1.35 *B.O. = 1.5*	1.39 *B.O. = 1.5*	1.36 *B.O. = 1.5*
13	2.01 *B.O. = 1*	1.39 *B.O. = 1*	1.47 *B.O. = 1*	1.50 *B.O. = 1*	1.32 *B.O. = 2*
14 & 15	2.17 *B.O. = 0.5*	1.25 *B.O. = 1.5*	1.33 *B.O. = 1.5*	1.46 *B.O. = 1*	1.33 *B.O. = 2*
16 & 17	2.05 *B.O. = 1*	1.29 *B.O. = 1.5*	1.30 *B.O. = 1.5*	1.47 *B.O. = 1*	1.33 *B.O. = 2*
18 & 19	1.75 *B.O. = 2*	*No bond*	1.17 *B.O. = 3*	1.42 *B.O. = 1*	1.34 *B.O. = 2*

Table 2.3. Bond distances and formal bond orders (*B.O.*) from optimized structures **10-19**.

Again, the final N-H bond in **17** is much stronger than the allylic C-H bond of propene (see Table 2.1, approximated by 2-propen-1-ol-1-imine). However, because this last hydrogen removal can be coupled with breaking the carbon-oxygen bond to release the acrylonitrile product, it still has a reasonable energy (**17 → 18**). Despite being mildly endothermic, this reaction will be favored entropically, since it releases a physisorbed product from a bound intermediate. Catalyst reoxidation (**18 → 19**) and desorption of acrylonitrile (**19 → 0**) completes the catalytic cycle, producing in total 1 acrylonitrile and 3 water molecules from 1 propene, 1 ammonia and $^3/_2$ oxygen molecules. Since acrylonitrile does not have any weak C-H bonds to attack, it should be stable to further oxidation, which is what is observed when acrylonitrile is fed over the catalyst at standard reaction conditions.[4]

3.6 Formation of acetonitrile and hydrogen cyanide

Our experimental work has shown that acetonitrile (CH$_3$CN) and hydrogen cyanide (HCN) are intrinsic products formed directly from propene, and not via secondary reactions involving either acrolein or acrylonitrile.[4] Given that allylamine is a likely intermediate along the route from propene and acrylonitrile and that ammoxidation of allylamine produces a similar ratio of byproducts to acrylonitrile as does ammoxidation of propene, we hypothesized that allylamine might also react to form CH$_3$CN and HCN. Since the byproducts have a higher N/C ratio than acrylonitrile and increasing the partial pressure of ammonia increases the selectivity to these byproducts,[4] we further hypothesized that allylamine might react with another ammonia molecule to form a 2C-1N fragment and a 1C-1N intermediate that could undergo additional reaction to form CH$_3$CN and HCN, respectively. Our experimental work showed that 1,2-

diaminopropane, the product of direct Markovnikov addition of ammonia across the carbon-carbon double bond of allylamine, did not react over the catalyst under the conditions used for propene ammoxidation.[4] However, the C-C bond in 1,2-diaminopropane is very weak, suggesting that if a similar species, but one stabilized by interaction with the catalyst, could form, it might serve as an intermediate to lower carbon number products. An illustration of this idea has already been discussed in Sections 3.4 and 3.5, where it was shown that intermediates stabilized by insertion into Mo=O bonds facilitated transformations that could not occur in the gas phase. As discussed below, we found that a species derived from allylamine bound to a surface molybdenyl oxo (Structure **13**) could react to form CH_3CN and HCN via an energetically-plausible pathway.

The formation of CH_3CH and HCN begins with allylamine adsorption onto a bare catalyst surface (Structure **10**), and then continues via steps **10** → **11** → **12** → **13** shown in Scheme 2.2. The subsequent steps leading to the two byproducts are shown in Scheme 2.3. As indicated in Figure 2.7, the adsorption of ammonia at a nearby Bi^{3+} cation produces structure **13N**. The adsorption is favorable, though not as favorable as on a bare surface; this is likely an artifact of artificial repulsive interactions between the two adsorbed molecules in neighboring unit cells, a consequence of the periodic boundary conditions.
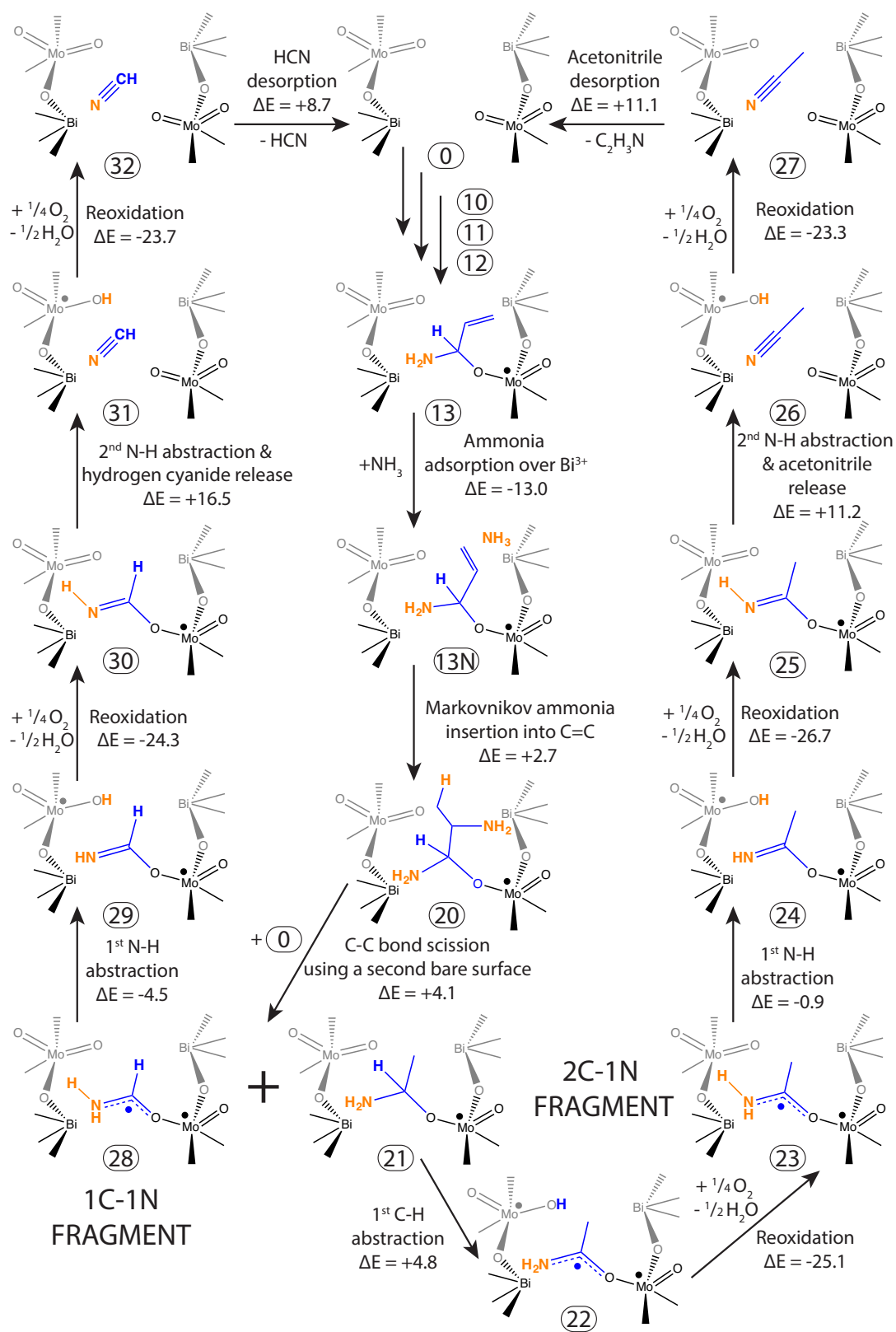
Scheme 2.3. Proposed elementary steps for allylamime ammoxidation to acetonitrile and hydrogen cyanide (ΔE in kcal/mol).
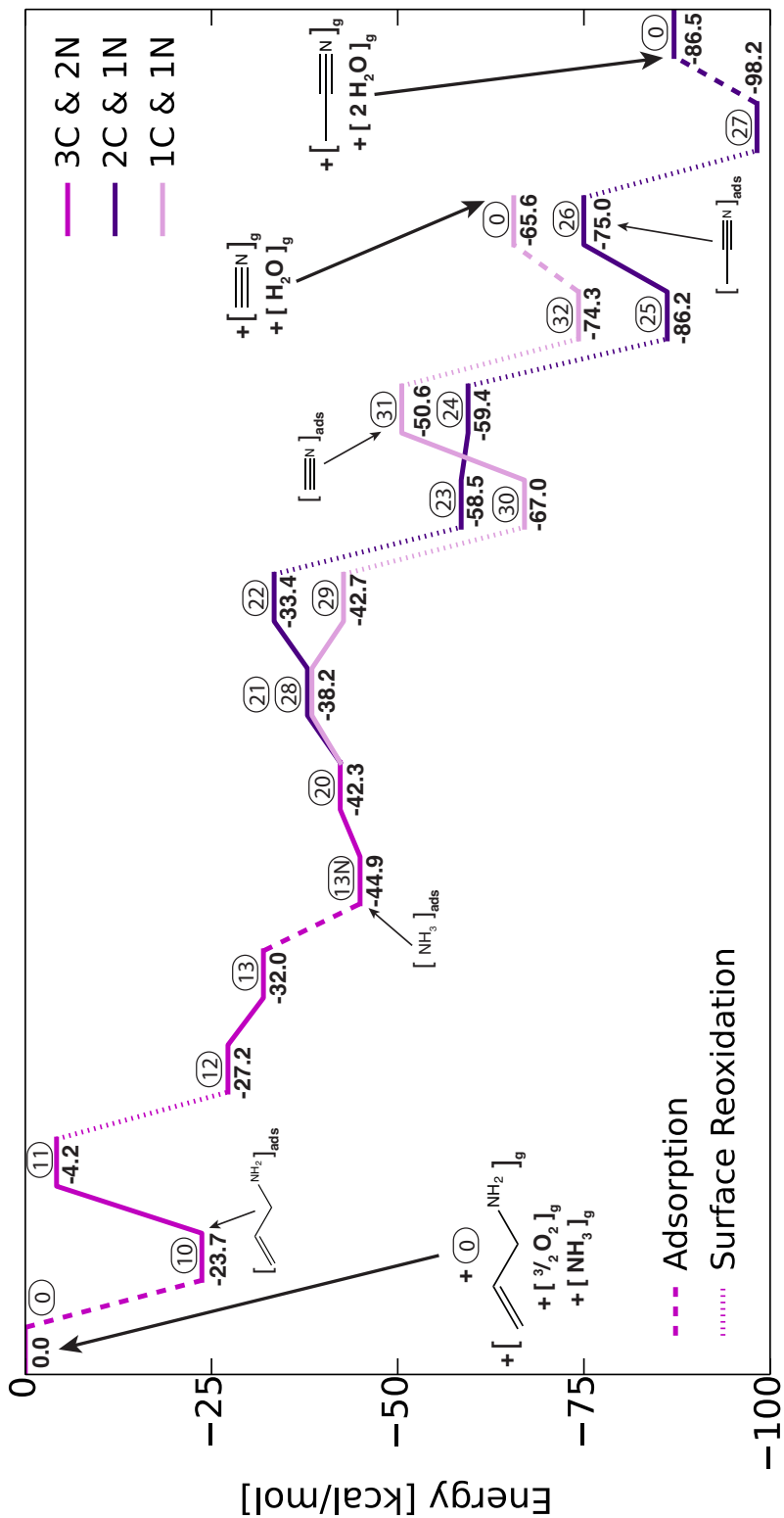
Fig. 2.7 Energy landscape for allylamine ammoxidation to acetonitrile and hydrogen cyanide. Encircled integers refer to structures in Scheme 2.3, bold numbers give the energy of each structure relative to the initial state.

The Markovnikov addition of the adsorbed ammonia across the carbon-carbon double bond of **13N** gives structure **20**. This reaction is only slightly endothermic. Breaking the C-C bond between the two carbon atoms that are each bound to nitrogen would result in a 2C-1N fragment that could become CH_3CN and a 1C-1N fragment that could become HCN. We hypothesize that this C-C bond cleavage reaction uses a neighboring $O=Mo^{6+}=O$ moiety to abstract the 2C-1N fragment, leaving behind the 1C-1N fragment. On the actual surface, after the C-C cleavage, the two fragments on neighboring $O=Mo^{6+}=O$ moities would be able to rotate away from each other, thus minimizing repulsive interactions between the two fragments. Unfortunately, because of the periodicity in our already very computationally-intensive unit cell, the fragments were not able to separate because they would encounter repulsive interactions with the repeating unit cell next door. This was not a problem in any of our other calculations because previously we have only ever abstracted a small hydrogen atom, not an entire hydrocarbon fragment. In order to compensate for this limitation of our quantum chemical model, we placed the 2C-1N fragment that would be abstracted by the neighboring $O=Mo^{6+}=O$ moiety onto a separate surface. This resulted in an overall reaction of **20 + 0 → 21 + 28**, which has a very low reaction energy of +4.1 kcal/mol. Therefore, while we are not able to calculate the reaction barrier for this C-C bond cleavage step, our approximation of the energy of reaction using two surfaces indicates that this is likely a very feasible reaction on the actual surface that does not have artificial periodicity.

After C-C cleavage, the two fragments formed in step **(20 + 0) → (21 + 28)** follow independent trajectories to their respective final products, CH_3CN and HCN. The 2C-1N fragment progresses through structures **21** through **27**, whereas the 1C-1N fragment progresses through structures **28** through **32** (see Fig. 2.7, Scheme 2.3 and Table 2.4) To illustrate these reactions on the energy landscape shown in Figure 2.7, we simply used the sum of the energies of structures **21** and **28** as the starting point, and then added or subtracted the energy difference between each structure and structure **21** (CH_3CN pathway) or **28** (HCN pathway) for the remaining steps. The steps are very similar to each other and follow the same trends with BDE as discussed in detail above for propene ammoxidation to acrylonitrile; therefore, they do not require much discussion beyond the fact that they are energetically favorable.

The first reaction of the 2C-1N fragment is a hydrogen atom abstraction from the central carbon to give **22**, since this bond is significantly weakened by the surrounding electron withdrawing O-Mo and NH_2 groups. This reaction is endothermic, with a reaction energy in the range of that calculated for other steps involving hydrogen abstraction from a bound intermediate (i.e. **4 → 5** and **13 → 14**). As in structure **14** discussed above, there is substantial electron delocalization between the nitrogen, primary carbon and oxygen atoms, such that each of those bonds is ~1.5 order, which results in the Mo-O bond order being less than 1. After the requisite reoxidation to give **23**, the fragment can lose one of the H atoms on the NH_2 group to leave a stable C=NH moiety (Structure **24**), a process that is energetically favorable (Fig. 2.7). After reoxidation to give structure **25**, the resulting fragment can lose its final H atom to a neighboring site and desorb from the catalyst surface (Structure **26**). This final step is endothermic but leads

to an entropy increase, since a physisorbed acetonitrile is produced from a surface-Mo-bound species. A final reoxidation step to give **27** and finally desorption of acetonitrile completes the catalytic cycle for a highly thermodynamically favorable reaction.

The reactions of the 1C-1N fragment are very similar to those of the 2C-1N fragment; however, because the fragment resulting from the C-C scission is a radical, the initial H abstraction from the NH$_2$ group to give Structure **29** is exothermic. After surface reoxidation, the fragment loses its final H atom and releases HCN from the surface (Structure **31**) in an energetically unfavorable, but entropically favorable, step. Reoxidation of the catalyst to give **32** and gas-phase HCN regenerates the bare surface in a highly exothermic reaction.

Structure #	Mo$_1$–O$_1$ or Mo$_2$–O$_2$ distance (Å)	O$_1$–C$_1$ or O$_2$–C$_2$ distance (Å)	C$_1$–N$_1$ or C$_2$–N$_2$ distance (Å)	C$_1$–C$_2$ or C$_2$–C$_3$ distance (Å)
20	2.01 [Mo$_1$–O$_1$] *B.O. = 1*	1.40 [O–C$_1$] *B.O. = 1*	1.45 [C$_1$–N$_1$] *B.O. = 1* 1.47 [C$_2$–N$_2$] *B.O. = 1*	1.56 [C$_1$–C$_2$] *B.O. = 1* 1.52 [C$_2$–C$_3$] *B.O. = 1*
21	2.00 [Mo$_2$–O$_2$] *B.O. = 1*	1.42 [O$_2$–C$_2$] *B.O. = 1*	1.48 [C$_2$–N$_2$] *B.O. = 1*	1.50 [C$_2$–C$_3$] *B.O. = 1*
22 & 23	2.17 [Mo$_2$–O$_2$] *B.O. = 0.5*	1.25 [O$_2$–C$_2$] *B.O. = 1.5*	1.33 [C$_2$–N$_2$] *B.O. = 1.5*	1.49 [C$_2$–C$_3$] *B.O. = 1*
24 & 25	2.05 [Mo$_2$–O$_2$] *B.O. = 1*	1.30 [O$_2$–C$_2$] *B.O. = 1.5*	1.30 [C$_2$–N$_2$] *B.O. = 1.5*	1.50 [C$_2$–C$_3$] *B.O. = 1*
26 & 27	1.74 [Mo$_2$–O$_2$] *B.O. = 2*	*No bond*	1.15 [C$_2$–N$_2$] *B.O. = 3*	1.43 [C$_2$–C$_3$] *B.O. = 1*
28	2.17 [Mo$_1$–O$_1$] *B.O. = 0.5*	1.25 [O$_1$–C$_1$] *B.O. = 1.5*	1.32 [C$_1$–N$_1$] *B.O. = 1.5*	
29 & 30	2.05 [Mo$_1$–O$_1$] *B.O. = 1*	1.29 [O$_1$–C$_1$] *B.O. = 1.5*	1.29 [C$_1$–N$_1$] *B.O. = 1.5*	
31 & 32	1.74 [Mo$_1$–O$_1$] *B.O. = 2*	*No bond*	1.15 [C$_1$–N$_1$] *B.O. = 3*	

Table 2.4. Bond distances and formal bond orders (*B.O.*) from optimized structures **20-32**.

Both acetonitrile and HCN are stable products, consistent with the high BDEs values of their residual hydrogen atoms (Table 2.1). However, we do observe experimentally that HCN and acetonitrile are produced in the constant ratio of approximately 5 HCN: 2 acetonitrile at all experimental conditions.[4] Therefore, one third of the 2C-1N intermediates react with another ammonia to make two 1C-1N fragments that both become HCN. The most likely scenario for this reaction is attack of the electron-deficient primary carbon of **25** by the lone pair on nitrogen, before **25** undergoes the endothermic final hydrogen abstraction and acetonitrile release to form **26**.

3.7 Acrolein ammoxidation to acrylonitrile

The final reaction we investigated is acrolein ammoxidation to acrylonitrile, which has been reported to be facile over bismuth molybdate but of minor importance, accounting for less than about 10% of the acrylonitrile formed from propene, because very little acrolein is formed when ammonia is present.[4,5,8] Our proposed mechanism for this reaction is shown in Figure 2.8. This pathway does not follow the same trends of sequential hydrogen abstractions from surface-Mo-bound species as the other pathways discussed above, since the reactant is already mostly oxidized. Instead, the catalyst only serves to stabilize the intermediates through physisorption, not chemical bonding, and to perform one hydrogen abstraction step in the pathway. However, it is the only chemically and energetically reasonable set of elementary steps that we were able to isolte for this reaction that experimentally has a very low activation energy of ~7kcal/mol[8].

The first step in this reaction (**0 → 8N**) involves adsorption of ammonia and acrolein, both of which occur favorably over Bi^{3+} cations via donation from lone pairs on the respective heteroatoms. These molecules are adsorbed on neighboring Bi^{3+} atoms that are 5.12 Å apart. Structure **8N** is also formed at the end of the pathway leading to acrolein in the presence of a spectator ammonia. Therefore, acrolein formed along that pathway could react immediately with an adsorbed ammonia molecule to form acrylonitrile rather than desorbing.

The next step is addition of ammonia across the carbon-oxygen double bond of acrolein (**8N → 33**). According to gas phase calculations, addition across this double bond is not as favorable as Markovnikov addition across the carbon-carbon double bond, as is done for allylamine conversion to acetonitrile and HCN (for NH_3 addition across C=O bond, ΔE = -8.1 kcal/mol; for NH_3 addition across the C=C bond, ΔE = -17.4 kcal/mol). Addition across the carbon-carbon double bond leaves an NH_2 bound to the central carbon and one terminal methyl group (CH_3-CH(-NH_2)-CH=O). However, is not obvious how this species could become acrylonitrile. We also considered other pathways for the reaction of acrolein, including one beginning with the abstraction of the reasonably high BDE aldehyde hydrogen ($\Delta E_{reaction}$ ~30 kcal/mol) and another in which acrolein inserts into a molybdenyl oxygen at the primary carbon atom ($\Delta E_{reaction}$ ~50 kcal/mol). However, because of the high reaction energies associated with these alternatives, neither is feasible for this low energy reaction.
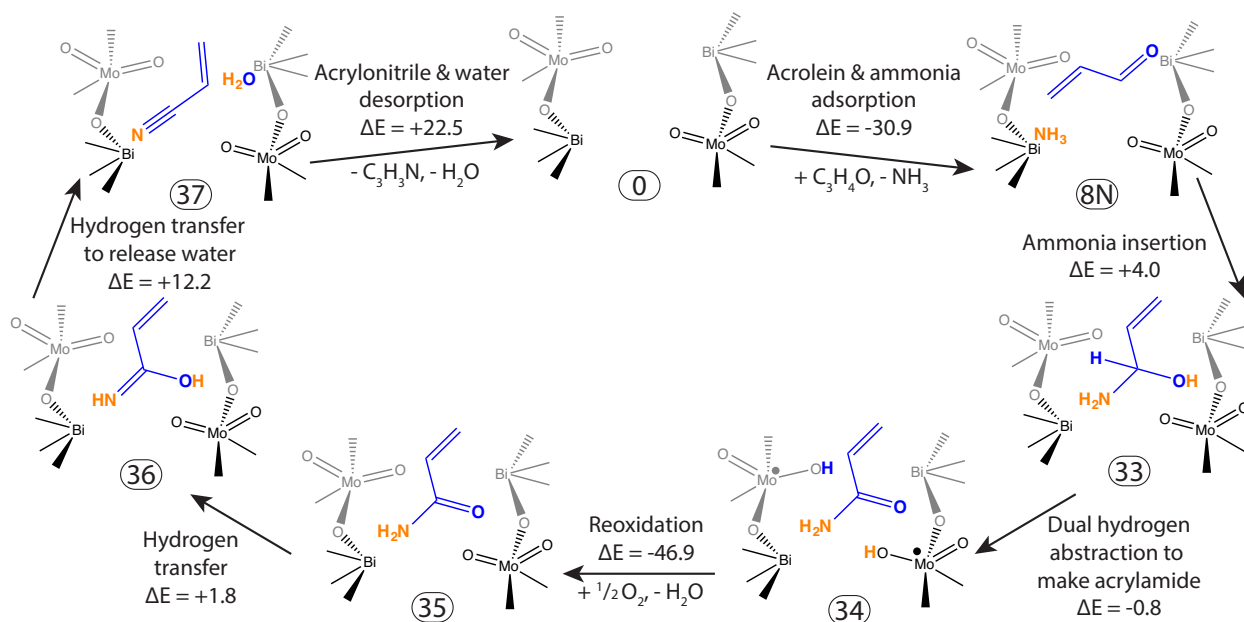
Scheme 2.4. Proposed elementary steps for acrolein ammoxidation to acrylonitrile (ΔE in kcal/mol).
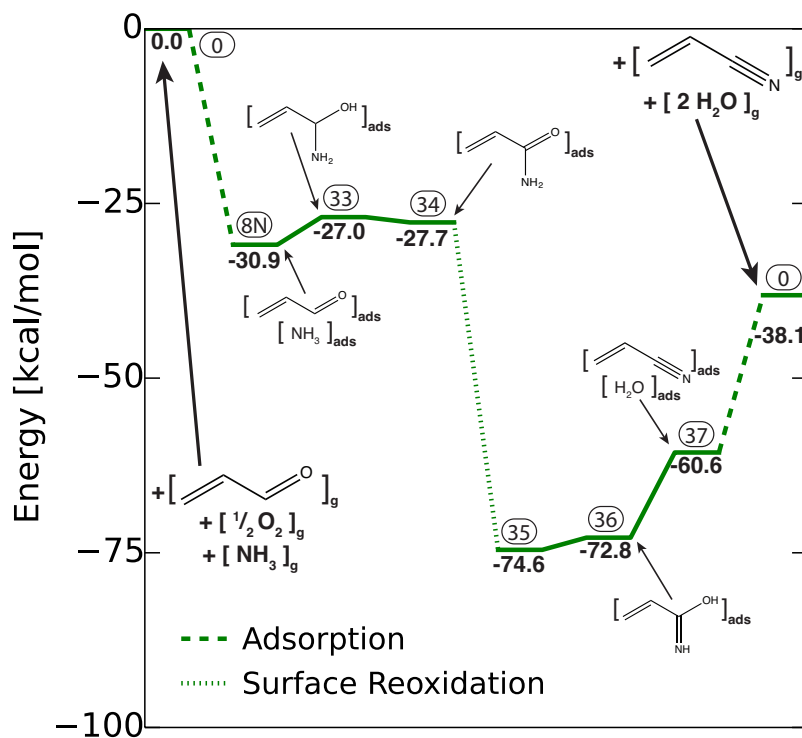

Fig. 2.8 Energy landscape for acrolein ammoxidation to acrylonitrile. Encircled integers refer to structures in Scheme 2.4, bold numbers give the energy of each structure relative to the initial state.

The addition of ammonia across the carbon-oxygen double bond of acrolein to form **33** is entropically disfavored and has a significant positive free energy in the gas phase (ΔG_{673K} = +20.1 kcal/mol). However, both acrolein and ammonia adsorb quite favorably on the surface of bismuth molybdate, promoting the reaction of the adsorbed molecules by increasing the probability of their interaction and reducing the entropy loss of their combination compared to that for reaction in the gas phase. This initial addition of ammonia to acrylonitrile (**8N → 33**) is likely to be the rate-limiting step for this reaction, since it is at the beginning of the pathway and both is mildly energetically and entropically disfavored.

The next step in this reaction is the sequential abstraction of two hydrogen atoms from **33** to form **34**. We initially tried to abstract only the hydrogen on the highly-substituted alpha carbon, since this bond is very weak (see Table 2.1, 2-propen-1-ol-1-amine); however, during optimization, the radical also shed the H atom on the OH group onto a nearby molybdenyl oxo to create a charge neutral acrylamide. Favorable reoxidation with an O atom removes both surface hydrogen atoms, leaving the adsorbed acrylamide (**35**).

Reaction of acrylamide to acrylonitrile and water involves two internal hydrogen atom transfers from the NH_2 group of acrylamide to the oxo group (**35 → 36 → 37**), followed by desorption. The internal hydrogen transfers of the adsorbed molecule may occur on their own or be facilitated by catalyst surface oxygen atoms. Considering the energy pathway in Figure 2.8, this reaction appears to be energetically unfavorable. Gas-phase calculations also show that this reaction is quite unfavorable at 0 K (ΔE = +26.0 kcal/mol) but at reaction temperature, (673 K) it becomes favorable (ΔG_{673K} = -4.4 kcal/mol). The likelihood of acrylamide as an intermediate in the formation of acrylonitrile is also supported by experimental observation. We tested the reaction of acrylamide in the presence of water vapor and oxygen over bismuth molybdate at 673 K, and observed almost complete conversion to acrylonitrile (see Ref. 4 for details of the experimental setup). Therefore, despite the mildly unfavorable energetics of Figure 2.8, a pathway from acrolein to acrylonitrile via acrylamide appears to be feasible.

4. Conclusions

We have analyzed the energetics of propene oxidation and ammoxidation occurring on the (010) surface of $Bi_2Mo_3O_{12}$ with the objective of establishing whether the proposed reaction sequence suggested by our experimental studies[4] is energetically feasible. We find that the most energetically demanding reaction is activation of a C-H bond of a methyl group in propene and that this process occurs preferentially at bismuth-perturbed Mo=O groups on the catalyst surface via a singlet-to-triplet spin-state crossing that occurs with high probability due to favorable spin-orbit coupling. This reaction has an intrinsic activation barrier of 38.8 kcal/mol. Favorable propene adsorption, a consequence of electron donation from the carbon-carbon pi bond to under-coordinated surface bismuth cations, results in an apparent activation energy of 27.3 kcal/mol. The transition state for hydrogen abstraction is similar in both energy and geometry to the product state, a physisorbed allyl radical and a surface hydroxyl. Rapid and energetically

favorable catalyst reoxidation accompanied by the release of water drives the activation reaction forward, offsetting the occurrence of the reverse reaction.

The allyl radical formed by propene activation is stabilized by reaction with a Mo=O group to form an allyl alkoxide. This species can then either undergo abstraction of its alpha hydrogen to form a surface-coordinated acrolein or reaction with NH_3 adsorbed via a dative bond on a proximate Bi^{3+} cation to form allylamine. We show that the activation barrier for the latter process is significantly lower than for the former, consistent with the experimental observations that, in the presence of gas-phase ammonia, acrylonitrile is formed preferentially to acrolein, and that the selectivity to acrolein increases with increasing temperature.[4]

In agreement with our experimental results, our calculations confirm that allylamine is a viable intermediate on the pathway to acrylonitrile. Reaction of allylamine occurs by sequential abstraction of the four hydrogen atoms in order of increasing bond dissociation energy, with stabilization of the intermediate species via bonding with a surface molybdenyl oxo species. Reaction of a surface bound allylamine with a second molecule of adsorbed NH_3 leads to a diamine species containing a weak C-C bond that can undergo cleavage to form intermediates that after dehydrogenation produce CH_3CN and HCN. These findings are in good accord with experimental observation. Finally, we have shown that acrolein can be converted to acrylonitirile via a sequence of steps that likely involve the formation of acrylamide. While the latter intermediate has not been observed experimentally, the reaction of acrylamide is found to produce acrylonitrile with almost complete conversion in the presence of oxygen at 673 K over $Bi_2Mo_3O_{12}$.

Chapter 3

Identifying the Unique Properties of α-Bi$_2$Mo$_3$O$_{12}$ for the Activation of Propene[0]

1. Introduction

Propene oxidation to acrolein and ammoxidation to acrylonitrile are commercially significant processes, each performed on the scale of ~10 billion lbs/year.[1] The catalysts used for these processes are based on bismuth molybdenum oxides, though commercial formulations may include as many as 10 additional elements to improve catalyst activity, selectivity, and lifetime.[2] The best single-phase catalyst for propene oxidation and ammoxidation is considered to be alpha bismuth molybdate, α-Bi$_2$Mo$_3$O$_{12}$, though some researchers have suggested that other bismuth molybdate phases, such as β-Bi$_2$Mo$_2$O$_9$ and γ-Bi$_2$MoO$_6$, exhibit similar activities.[3,4,5] Mechanistic studies of propene oxidation and ammoxidation have therefore focused on the three primary bismuth molybdate phases, with particular emphasis on the α-Bi$_2$Mo$_3$O$_{12}$ phase. The activation energy and partial pressure dependencies for both reactions are the same, leading to the conclusion that the rate-limiting step is the same.[6,7,8,9] Both experimental and theoretical studies have identified this step to be the abstraction of a hydrogen atom from the terminal methyl group to produce a physisorbed allyl radical.[10,11,12,13,14] Isotopic labeling studies have shown that the oxygen atoms involved in propene oxidation come from the catalyst surface and not from adsorbed O$_2$, which only serves to reoxidize the catalyst.[15,16,] The elementary steps by which allyl radicals are converted to acrolein or acrylonitrile have been the subject of a number of studies.[7,17,18,19,20,21]

Considerable effort has been devoted to identifying the characteristics of a mixed metal oxide that make it active for propene oxidation and ammoxidation. While much is known about the structure and electronic properties of bismuth molybdates, the reason why Bi$_2$Mo$_3$O$_{12}$ is particularly active remains a subject of discussion.[14,22,23,24,25] The crystal structure of Bi$_2$Mo$_3$O$_{12}$ is related to that of the tetragonal mineral scheelite (CaWO$_4$), but with a monoclinic distortion due to the vacancies that result from the replacement of Ca^{2+} with Bi^{3+} (Bi$_{2/3}$φ$_{1/3}$MoO$_4$ where φ is a vacancy).[26] The flexibility of the scheelite structure enables $_{the}$ synthesis of many single-phase, solid-solution tri- and tetra-metal oxides, and has therefore formed the basis for much of this

work.[27] However, the scheelite structure alone is insufficient for high activity. For example, lead molybdate $PbMoO_4$ crystallizes as a pure scheelite,[28] but is essentially inactive for propene oxidation and ammoxidation.[29] Complete substitution of the Pb^{2+}, e.g. in $Na_{0.5}Bi_{0.5}MoO_4$, produces a similarly inactive material. However, the activity of these materials increases substantially upon addition of a small amount of Bi^{3+}, with the concurrent addition of vacancies, to form $Pb_{1-3x}Bi_{2x}\varphi_x MoO_4$ ($0 < x \leq 0.07$) or $Na_{0.5-3x}Bi_{0.5+x}\varphi_{2x}MoO_4$ ($0 < x \leq 0.17$).[27,30] These findings have led to the conclusion that cation vacancies are required for catalysis and that somehow vacancy sites are responsible for propene activation. It notable, however, that bismuth addition and vacancy formation occur simultaneously. To decouple the effects of these two parameters, additional experiments have been performed with $Pb_{1-3x}La_{2x}\varphi_x MoO_4$, in which defects are introduced, but not Bi^{3+} cations.[21] The latter system shows no catalytic activity for $0 \leq x \leq 0.04$, suggesting that both Bi^{3+} cations and vacancies together are required for a molybdate catalyst to exhibit high catalytic activity. This hypothesis is further supported by observations that europium molybdate[31] and cerium or lanthanum molybdate,[32] which also crystallize in scheelite-derived structures containing trivalent cations, but with different orderings of cation vacancies, exhibit lower catalytic activities than $Bi_2Mo_3O_{12}$.

Scheelite structures in which molybdenum is partially or completely replaced with another transition metal (i.e., Fe, V, Ga, W) have also been investigated.[33,34] The activation energy of these catalysts for propene oxidation to acrolein correlates very well with the electronic band gap measured by UV-Visible Spectroscopy at reaction temperature or calculated with Density Functional Theory (DFT).[22] This correlation was found to be a consequence of the electronic structure of the transition state for H abstraction from propene, which was found to involve a singlet-triplet spin crossing where molybdenyl oxo is rehybridized (Mo=O → •Mo–O•) so that it can accept the hydrogen atom removed from the methyl group of propene.[19,38] The band gap is a measure of the singlet-triplet excitation energy, and therefore correlates to the activation energy for a metal oxo to abstract a hydrogen atom from propene. In these catalysts, the chemistry is presumed to occur on oxygen atoms associated with the redox active metal – molybdenum or its replacement transition metal – and not on oxygen atoms associated with the redox inactive bismuth. This hypothesis is supported by both experimental and theoretical investigation, *vide infra.*

Previous work has shown that while both Bi_2O_3 and MoO_3 are essentially inactive for propene oxidation to acrolein or ammoxidation to acrylonitrile, Bi_2O_3 is able to activate propene and produce a small amount of hexadiene,[35] and molybdenum oxide is able to convert allyl radicals generated *in situ* to acrolein.[36] These findings have led to the longstanding hypothesis that oxygen atoms bound to bismuth are responsible for propene activation to generate allyl radical, while oxygen atoms bound to molybdenum, presumably as molybdenyl oxo groups, are responsible for the conversion of allyl radical to acrolein.[37] However, recent XANES studies have shown that this interpretation is not correct. Exposure of $Bi_2Mo_3O_{12}$ to pure propene at 713 K for 24 h results in the reduction of molybdenum from the 6+ to the 4+ oxidation state, but bismuth remains in the 3+ oxidation state.[18] Supporting DFT calculations[19,38] have led us to

conclude that oxygen atoms bound to molybdenum atoms perform all of the chemistry in $Bi_2Mo_3O_{12}$. Therefore, the question of why bismuth is necessary for catalysis remains unanswered.

Our recent theoretical work has shown that Bi^{3+} cations electronically perturb the neighboring surface molybdenyl oxo groups and, in doing so, enhance the activity of these sites for propene activation via abstraction of a hydrogen atom from the methyl group of adsorbed propene.[19] The influence of the Bi^{3+} cations was attributed to electronic repulsion between the bismuth lone pair and an oxygen 2p lone pair, which destabilizes the Mo=O singlet state, and from back donation from the •Mo–O• π* orbital to the bismuth 6p orbital, which stabilizes the triplet state. The combination of these electronic effects leads to a lower singlet → triplet excitation energy, and thus lowers the transition-state barrier for hydrogen abstraction from propene. However, the magnitude of this effect is estimated to be only ~3 kcal/mol, which is not enough to explain the overall difference in activity between $Bi_2Mo_3O_{12}$ and other molybdenum-oxide-based materials.

The preceding discussion demonstrates that both the composition and structure of mixed metal oxides play an important role in defining the activity of such materials for propene oxidation and ammoxidation. The aim of the present investigation is use DFT calculations to identify the extent to which specific geometric and electronic properties contribute to the activation energy for propene activation. We have focused our investigation on oxides containing molybdenum as the only redox-active metal, thereby allowing us to directly compare the effects of crystal structure, Mo coordination, and the identity of additional elements. The four metal oxides investigated are MoO_3, $Bi_2Mo_3O_{12}$, $PbMoO_4$, and a mixed Pb/Bi molybdate derived from $PbMoO_4$. Together, these different materials represent a range of molybdenum coordination environments (asymmetric 6-, distorted 5-, symmetric 4-, and distorted 4-coordinate), modifying elements (none, Bi, Pb, and both Bi and Pb), and associations between the molybdenum and the modifying element.

2. Methods

2.1 Slab model calculations

All calculations were performed using the Vienna *Ab initio* Simulation Package (VASP) version 5.3.5 using the PBE[39] and M06-L[40] functionals. Calculation parameters were based on those detailed in our previous investigation of functionals for modeling properties of reducible transition metal oxides.[38] Plane wave basis sets[41] were used to model valence electrons and projector augmented wave (PAW) functions[42] were used to model the core electrons. The PAW cores were designed for a plane wave cutoff energy of 400 eV and this cutoff was used for all calculations. Energies were converged with a Gaussian energy smearing of 0.05 eV. In all cases, a converged PBE wave function was used as the initial guess for the final M06-L calculation,

since the M06-L functional performs poorly with the default random number initial guess of the wave function.

The atomic positions for bulk $Bi_8Mo_{12}O_{48}$, $Pb_4Mo_4O_{16}$ and Mo_4O_{12} were taken from literature.[26,28,43] The total energy for each literature crystal structure with respect to the gamma k-point mesh was converged to within 0.5 meV/atom. Bulk $Bi_8Mo_{12}O_{48}$ required 3x2x2 k-points, bulk $Pb_4Mo_4O_{16}$ 4x4x2 k-points, and bulk Mo_4O_{12} 6x2x6 k-points. Using these k-point grids, the atomic positions of each structure were then allowed to relax at a series of fixed volumes. The Burch-Murnaghan Equation of State[44] was used to fit the data of energy versus volume and calculate the cell volume with the minimum energy. The atoms were then allowed to relax at this fixed minimum energy volume until the total energy converged to within 0.1 meV. The optimized cell volume for was found to be 2.3% larger than the experimental value $Bi_8Mo_{12}O_{48}$, 1.6% smaller for $Pb_4Mo_4O_{16}$, , and 4.8% smaller for Mo_4O_{12}.

Both alpha bismuth molybdate and molybdenum trioxide have one crystallographic axis along which there are four layers, with each pair of layers strongly bound together and weaker bonds between the paired layers, and only strong bonds between atoms in the other two crystallographic directions. Cleaving the crystal between the weakly bonded layer pairs is, therefore, the most obvious way to produce a surface with the lowest energy. The resulting surface is the (010) surface for both alpha bismuth molybdate and molybdenum trioxide. Lead molybdate also has four layers in the direction perpendicular to the (001) plane, which, because of crystallographic naming conventions, is the pure scheelite plane that is equivalent to the (010) plane in the distorted scheelite alpha bismuth molybdate. Therefore, for consistency in comparison with alpha bismuth molybdate, we used the (001) surface of lead molybdate, which is also the principal plane observed experimentally after cooling a $PbMoO_4$ melt.[45] The optimized bulk structures were cleaved to create the relevant surface plane terminated with a full complement of oxygen atoms and 14 Å of vacuum space was added above the atoms to create a surface. The top two layers were allowed to relax to a convergence of 0.5 meV, while the bottom two layers were fixed in their bulk positions to simulate the bulk oxide below the surface.

The crystallographic unit cells of both lead molybdate and molybdenum oxide only contain one molybdenum atom in each layer, which, because of the periodic boundary conditions, results in the effective reduction of every surface molybdenum atom upon attachment of only one hydrogen atom. To avoid this, for both materials, multiple unit cells were combined to make a supercell that was used to model the oxide surface. Two unit cells were combined to represent $Pb_8Mo_8O_{32}$, which has two surface Mo atoms and two surface Pb atoms. The resulting (001) surface plane is a 59.4 $Å^2$ square that needed 3x3x1 k-points to yield converged energies. Four unit cells were combined to create $Mo_{16}O_{48}$, which has four Mo atoms on the (010) surface forming an almost square surface also with area 59.4 $Å^2$. Calculations on this slab were performed at 3x1x3 k-points. For comparison, $Bi_8Mo_{12}O_{48}$ has three surface Mo atoms, two surface Bi atoms, and has a rhombohedral surface with an area of 83.9 $Å^2$. Slab calculations on this (010) surface employed 3x1x2 k-points. The Minnesota family of functionals requires a fine integration grid to provide accurate energies,[46] therefore an integration grid of 1 point per each

~0.085Å in each crystallographic direction was used (90x288x144 for $Bi_8Mo_{12}O_{48}$, 90x90x300 for $Pb_8Mo_8O_{32}$, and 90x324x90 for $Mo_{16}O_{48}$). We defined the number of bands explicitly to account for all of the electron pairs in each bulk surface plus an additional ~20% of empty valence bands (240 bands for $Bi_8Mo_{12}O_{48}$, 168 for $Pb_8Mo_8O_{32}$ and 240 for $Mo_{16}O_{48}$). The added bands are essential in order to include all of the unoccupied d orbital states on each Mo in the calculation, so that the band gap and conduction band states (including the LUMO) are properly described.

We also generated a mixed bismuth/lead material with the unit cell $Pb_5Bi_2Mo_8O_{32}$. According to the phase diagram for $Pb_{1-3x}Bi_{2x}\varphi_xMoO_4$, a single phase scheelite material can exist up to x ≈ 0.15, though only at specific temperatures (i.e. only ~970 K for x ≈ 0.15).[47] Above x ≈ 0.15 or at other temperatures, this material will separate into a mixed scheelite and $Bi_2Mo_3O_{12}$. Our model compound $Pb_5Bi_2Mo_8O_{32}$ (x = 0.125), would be difficult to maintain in a single-phase solid solution; however, it is known to exist[47] and it is the only mixed Pb/Bi molybdate that can be easily generated from the pure scheelite lead molybdate without requiring a computationally infeasible number of atoms in the unit cell. $Pb_5Bi_2Mo_8O_{32}$ was made by replacing three lead atoms in the bulk $Pb_8Mo_8O_{32}$ with two bismuth atoms and one vacancy. One bismuth atom and one lead atom were placed at what would become the surface, one lead and the vacancy were placed in the layer below, and finally one lead atom and the last bismuth atom were placed in the layer below the vacancy. Bulk $Pb_5Bi_2Mo_8O_{32}$ required 3x3x2 k-points (crystallographic axes the same as lead molybdate). The optimal cell volume was found by allowing the atoms to relax with a series of fixed tetragonal cell volumes and fitting the volume versus energy with the Burch-Murnaghan Equation of State to find the optimal cell volume. The experimentally-measured cell volume of $Pb_{0.64}Bi_{0.24}MoO_4$, which is very similar to our model compound ($Pb_{0.625}Bi_{0.25}MoO_4$), is 2.5% smaller than that of $PbMoO_4$,[47] since bismuth cations have a smaller radius than lead cations. In excellent agreement with these experimental results, we calculated the DFT optimized cell volume of $Pb_5Bi_2Mo_8O_{32}$ to be 2.5% smaller than the DFT optimized cell volume of $PbMoO_4$. It should be noted that no monoclinic distortion has been observed experimentally for any single-phase mixed Pb/Bi material,[47] so we fixed our model compound $Pb_5Bi_2Mo_8O_{32}$ to have tetragonal symmetry while changing the volume and optimizing the atom positions. Once the bulk $Pb_5Bi_2Mo_8O_{32}$ was optimized, the (001) surface was generated and optimized in the same way as $Pb_8Mo_8O_{32}$ (see above).

Finally, we tested substituted bismuth molybdate structures where one bismuth atom was replaced by one atom of a different element in order to determine the effect of that atom. For these structures, the optimized surface of $Bi_8Mo_{12}O_{48}$ was used as the starting structure, and then the entire surface was allowed to relax to within 0.5 meV with the relevant surface bismuth atom replaced by another element. Since lead has a different oxidation state than bismuth (2+ versus 3+), a hydrogen atom was also included in the former case in order to balance the charge (i.e., $PbHBi_7Mo_{12}O_{48}$). The other elements tested were all in the 3+ oxidation state (Sb, B, La).

2.2 Cluster model calculations

In order to examine the molecular orbitals around molybdenum for different bonding configurations, we carried out model cluster calculations using quantum chemical methods contained in the Q-Chem software package, version 4.2.3.[48] The Def2-TZVPD effective core potential and valence basis set,[49] obtained from the EMSL basis set exchange,[50] was used for molybdenum and the 6-311++G(3df,3pd) basis set was used for oxygen, hydrogen and carbon. The M06-L exchange-correlation functional[40] was employed to obtain the final cluster and orbital energies presented here. The results were also compared to calculations with the PBE functional[39] and with the ωB97X functional, both with and without dispersion (ωB97X-D),[51] and verified to show the same trends. Molecular orbitals were extracted using MolDen,[52] and electron density plots prepared with Vesta.[53]

A 4-coordinate $MoO_2(OH)_2$ cluster and a 5-coordinate $MoO_2(OH)_2$-$O(CH_3)_2$ cluster, where in the later case the dimethyl ether (DME) is orientated such that the oxygen is pointing towards the molybdenum to mimic a fifth coordination site, were individually optimized both with and without an added hydrogen. For both clusters, the same torsional angle constraint on both side hydroxyl groups (116.4° for O_{Cis}-Mo-O-H) was used to prevent the hydrogen atoms from engaging in spurious hydrogen bonding with the oxo groups, since those hydrogen atoms are merely there to terminate the cluster. In order to extract the molecular orbital energies for the optimized clusters after hydrogen addition, the geometry was frozen, the hydrogen removed, and the orbitals calculated in the spin singlet state. For the plots of energy versus Mo-O_δ distance, the cluster was allowed optimize with the constraint that the Mo-O_δ distance remained fixed.

DME was chosen to mimic the fifth coordination site because it provides a 2-coordinate oxygen moiety that is small and does not add obfuscating hydrogen bonding effects. DME is admittedly not a perfect model of the Bi–O–Mo arrangement that is the fifth coordination site in $Bi_2Mo_3O_{12}$, but, by using DME, we are able to isolate the effect of bringing an additional oxygen coordination close to the molybdenum without significantly perturbing the rest of the molybdate cluster in any way. For this reason, we do not attempt to directly compare the results of the cluster calculations and the slab calculations, but merely extend the findings from the cluster calculations to explain what we observe in the slab calculations.

3. Results and discussion

3.1 Key energy parameters

We propose that an active catalyst for propene oxidation and ammoxidation must have (1) an active oxygen atom for hydrogen abstraction and (2) a favorable propene adsorption site near the active oxygen atom. In order to probe these features for $Bi_2Mo_3O_{12}$, $PbMoO_4$, $Bi_2Pb_5Mo_8O_{32}$ and MoO_3, we will reference the energies shown in Figure 3.1, so that for each material, zero relative energy is the bare oxidized surface plus propene in the gas phase.

$\Delta E_{ads,C3H6}$ is the energy change upon propene adsorption on the oxidized surface and will always be a negative number. ΔE_{rxn} is the overall energy of reaction to go from adsorbed propene to adsorbed allyl radical and a hydrogen atom added to a Mo=O group. This hydrogen abstraction process has an activation barrier, shown in grey in Figure 3.1. The transition-state energy is designated as ΔE_{TS}. At the high temperature required for propene oxidation and ammoxidation (~ 600-700 K), entropy dominates adsorption, and the catalyst resting state is the bare oxidized surface plus gas-phase propene. Therefore, as indicated by $E_{a,app}$ in Figure 3.1, the apparent activation energy for hydrogen abstraction from propene will be the energy difference between the transition state and the bare oxidized surface with propene in the gas phase.

We have previously calculated the activation barrier for hydrogen abstraction from propene adsorbed on $Bi_2Mo_3O_{12}$ to be $\Delta E_{TS} = 38.8$ kcal/mol.[17] This reaction occurs via a singlet-triplet spin-crossing transition state that is only 7.6 kcal/mol above the final state. In the final state, the allyl radical is weakly adsorbed on the oxide surface and has a geometry and energy that are quite similar to those of the transition state. Since determination of the transition state is computationally very intensive, in part due to the slow convergence characteristics of calculations done using the M06-L functional, we chose to compare the properties of different oxides on the basis of the structure and energy of the final state attained after hydrogen abstraction from propene and to use this energy as a measure of the relative apparent activation energies for hydrogen abstraction from propene on different oxides. We note that the energy of the final state is clearly a lower bound on the apparent activation energy, since the transition state must be higher in energy than the energy of the final state. As will be shown below, calculation of this lower bound is sufficient for comparing the catalytic activity of different molybdate phases.

Another metric we will use is the Hydrogen Attachment Energy (HAE), which is a measure of the hydrogen abstraction ability of various surface oxygen atoms. The HAE is defined as the energy difference between an all-electron-paired bare catalyst surface plus a gas phase hydrogen atom (with a single electron) and the catalyst surface with the hydrogen atom attached to a surface oxygen and thus one unpaired electron, as in Eqn (1).

$$HAE = E_{H-surf} - (E_{surf} + E_H) \tag{1}$$

Figure 3.1 demonstrates that the energy of the final state is the sum of HAE, the bond dissociation energy of a hydrogen on the methyl group of propene E_{C-H}, and the adsorption energy for the allyl radical $\Delta E_{ads,C3H5}^{=}$. Since E_{C-H} it is independent of the catalyst and $\Delta E_{ads,C3H5}^{=}$ is expected to be similar in magnitude to the propene adsorption energy $\Delta E_{ads,C3H6}$, we will use the HAE to determine the most active surface oxygen atom on each material.

There is precedent in the literature for using hydrogen attachment energy as an approximation for C-H bond activation activity, specifically in the area of methane activation. For example, high-level theory calculations reported by Kwapien et al.[54] demonstrate a good correlation between the hydrogen attachment energy and apparent activation barrier for hydrogen abstraction from both H_2 and CH_4 by metal oxide clusters containing 2-7 metal atoms, as do additional gas phase methane activation calculations by other researchers.[55] Additionally,

previous work in our own group modeling $Bi_2Mo_3O_{12}$ with a less accurate density functional showed that the surface oxygen atom with the lowest HAE had the lowest reaction barrier for hydrogen abstraction from propene, though the reaction barriers for the less active surface oxygen atoms did not track with the HAE.[19] Therefore, though the HAE is not a perfect representation, because of its significantly lower computational requirements, calculations of the HAE provide a reasonable starting point for investigating the activity of a material for C-H bond activation.
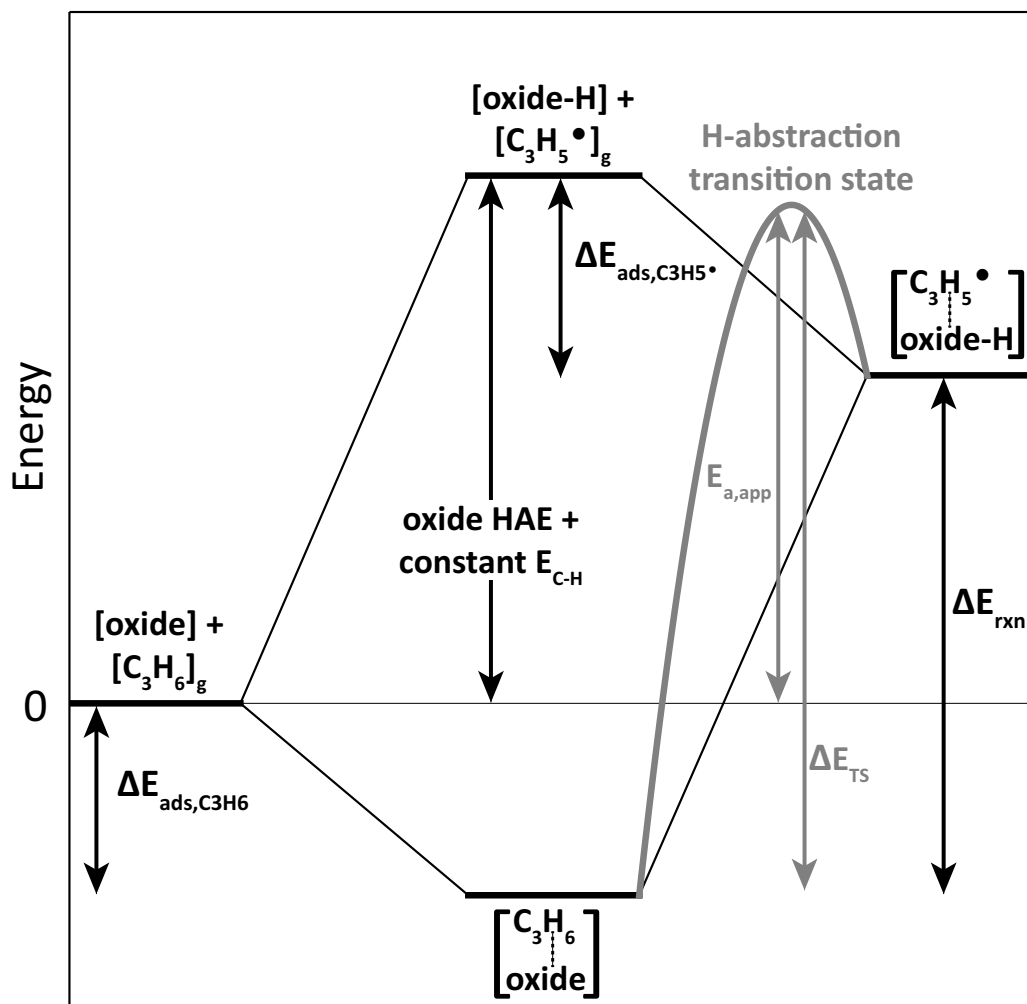

Fig. 3.1 Diagram depicting the various calculated energy values used throughout this paper.

3.2 Types of surface oxygen atoms

As presented in Table 3.1, there are different types of oxygen atoms on the surface of the oxides studied, which can be grouped into four general categories. The first type, O_α, is a pure molybdenum-oxygen double bond with a bond length less than or equal to 1.70 Å. The second type, O_β, is an oxygen atom doubly bonded to Mo that is electronically perturbed by a neighboring atom (X), resulting in a slightly longer Mo-O distance, between 1.70 and 1.76 Å. The third type, O_γ, has two single bonds to two different atoms (Mo and X), resulting in a

molybdenum-oxygen distance of 1.76-2.00 Å. Finally, the fourth type, O_δ, has two single bonds to two atoms and is also loosely coordinated to a nearby molybdenum atom at a distance of 2.00-2.40 Å. Beyond a Mo-O distance of 2.40 Å, there is no specific interaction between the two atoms.
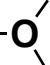
Oxygen Name	Mo–O distance (d) range [Å]	Depiction	Description
O_α	≤ 1.70	**Mo═O**	Pure double bond
O_β	1.70 < d < 1.76	**Mo═O----X**	Electronic perturbation by X
O_γ	1.76 ≤ d < 2.00	**Mo—O—X**	Two single bonds
O_δ	2.00 ≤ d < 2.40	**Mo----O**	Loose coordination

Table 3.1. Types of surface oxygen atoms.

3.3 Hydrogen addition to oxide surfaces

In the following subsections, we present the HAE (Table 3.2) and the surface geometry before and after hydrogen addition for each of the four metal oxide materials (Figs. 2-7). These data can be used to identify what geometries lead to a low HAE. As will be shown, increased coordination of molybdenum 6+ cations by oxygen anions significantly lowers the value of the HAE. We also find that the ability of the surface to distort upon hydrogen addition and therefore coordinate molybdenum with an additional bulk oxygen atom positioned *trans* to the oxygen atom to which the hydrogen was added is crucial for achieving a favorable HAE.

Material	Type of Surface Oxygen	HAE (kcal/mol) Full surface relaxation *[hydroxyl relaxation only]*
$Bi_2Mo_3O_{12}$	O_α	-52.9 *[-45.8]*
	O_β	**-58.3 *[-47.2]***
	O_γ	-45.5
$PbMoO_4$	O_β	-44.0
$Bi_2Pb_5Mo_8O_{32}$	O_β	-44.7
	O_β'	**-47.6 *[-40.3]***
	O_β"	-43.4
	O_γ	-43.9
MoO_3	**O_α**	**-58.2 *[-54.8]***
	O_β	-63.2 *[-36.1]*

Table 3.2. Hydrogen addition energy (HAE) to every type of surface oxygen for the four tested materials.
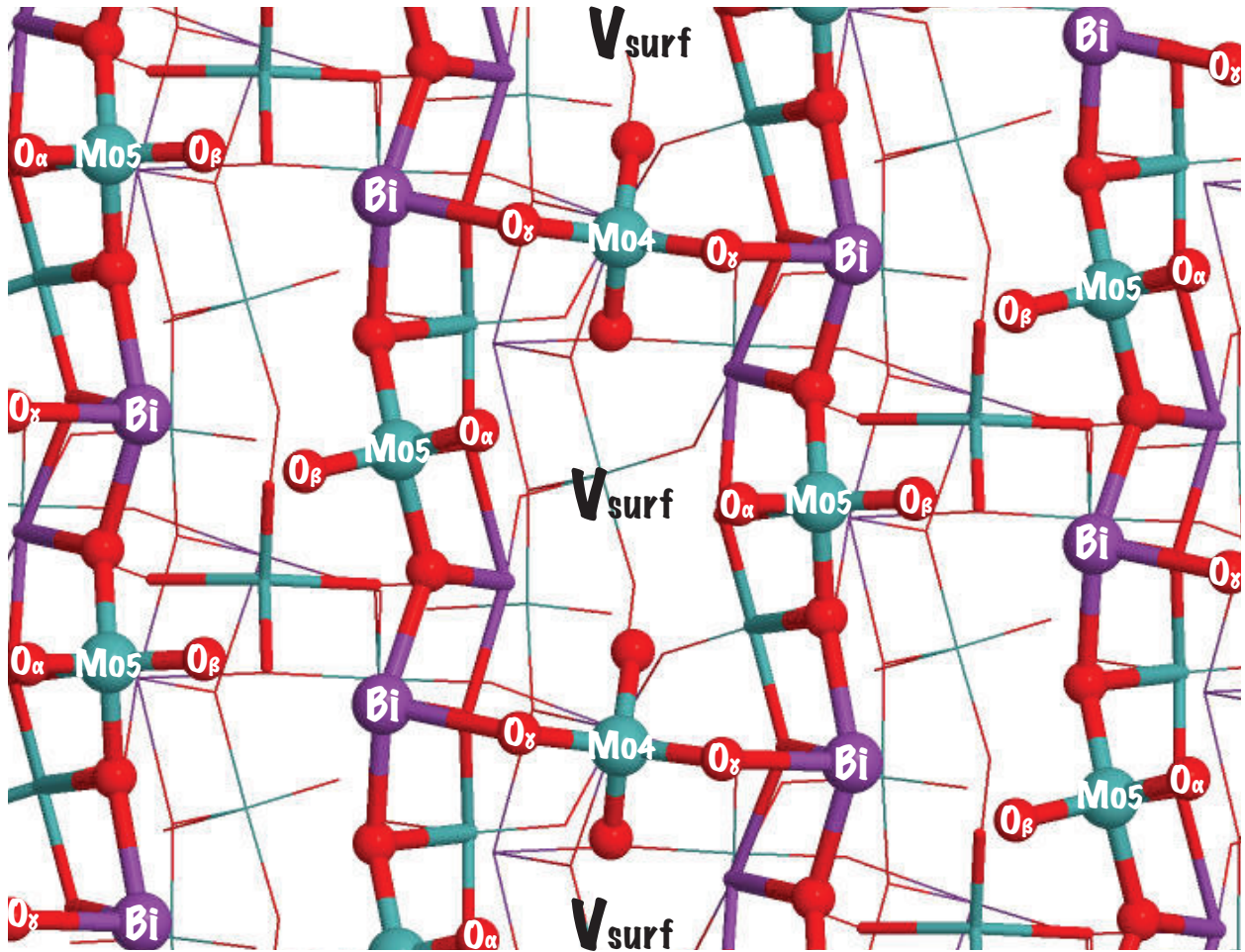
3.3.1 Alpha bismuth molybdate

Fig. 3.2 Top down view of $Bi_2Mo_3O_{12}$, where Mo atoms are turquoise, Bi are purple, and O are red, and the location of surface cation vacancies are indicated by V_{surf}. Surface atoms are identified in white (see Table 1 for explanation of oxygen types).

A top-down view of the lowest energy (010) surface of $Bi_2Mo_3O_{12}$ is shown in Figure 3. 2 with the ordered cation vacancies indicated with "V_{surf}" and a side view is shown in Figure 3.3a. The pseudo-5-coordination of molybdenum and asymmetrical 8-coordination of bismuth in bulk $Bi_2Mo_3O_{12}$ result in two general types of surface molybdenum atoms and three types of surface oxygen atoms. Two thirds of the surface molybdenum atoms are 5-coordinate (Mo_5), formally doubly bonded to two oxygen atoms at the surface (1 O_α and 1 O_β), singly bonded to two oxygen atoms within the surface that connect to neighboring metal atoms, and loosely coordinated to a fifth oxygen atom located beneath the molybdenum (O_δ) that is singly bound to two subsurface metal atoms. The O_α is a pure molybdenyl oxo on the cation vacancy side, while the O_β is electronically perturbed by the neighboring Bi^{3+} cation. As shown in Figure 3.3a, surface Bi^{3+} cations are bonded (Bi-O distance 2.1-2.4Å) to four oxygen atoms on one side of

itself and coordinated (Bi-O distance 2.5-3.0Å) to two oxygen atoms on its other side, one of which is the surface O_β, but are missing two additional coordinated oxygen atoms they would have in the bulk. The remaining one third of the molybdenum atoms are 4-coordinate (Mo_4), with two singly bonded surface oxygen atoms connected to neighboring metal atoms (O_γ) and two doubly bonded oxygen atoms located below the surface. In the bulk, these Mo_4 atoms would have a fifth loosely coordinated oxygen atom, which is absent at the surface.

Figure 3.3b illustrates the geometry at Mo_5 after addition of a hydrogen atom to O_β, Figure 3.3c the geometry after addition a hydrogen atom to O_α, and Figure 3.3d the geometry at Mo_4 after addition to O_γ. We observe that the addition of hydrogen atom to the bismuth perturbed molybdenyl oxo O_β, causes the molybdenum atom to sink into the catalyst (Fig. 3.3b). This movement results in the formation of a full single bond between the molybdenum and the oxygen (O_δ) *trans* to the position where the hydrogen atom is added, which was previously only loosely coordinated to molybdenum. Similar movement is observed after hydrogen atom addition to the pure molybdenyl oxo, O_α. Again, the molybdenum atom attempts to coordinate with a bulk oxygen atom *trans* to where hydrogen is added; however, that oxygen starts 2.91 Å away from the molybdenum and is therefore only able to achieve a final distance of 2.39 Å after significant surface deformation. Table 3.2 shows that hydrogen addition to O_β is favored by 5.4 kcal/mol over O_α. By adding a hydrogen atom to either O_α and O_β and only allowing the hydroxyl group to relax while forcing the rest of the atoms to remain in their optimized oxidized surface positions (see bracketed numbers in Table 3.2), we determined that the more favorable value of HAE for hydrogen addition to O_β is mostly due to the ability of the surface to relax to a final geometry with lower energy.

Hydrogen addition to O_γ is significantly less favorable than addition to either O_α or O_β, as can be seen from Table 3.2. In contrast to H addition at O_α or O_β, which results in replacement of a Mo=O π bond by an O-H σ bond, H addition at O_γ involves replacement of a Bi-O σ bond by an O-H σ bond, which is less exothermic. After addition to O_γ, the molybdenum it is bound to barely moves and remains purely 4-coordinate, while the bismuth that O_γ is also bound to moves significantly to break the Bi-O_γ bond. In moving away from O_γ, the already under-coordinated bismuth becomes even more under-coordinated, which is also energetically unfavorable.
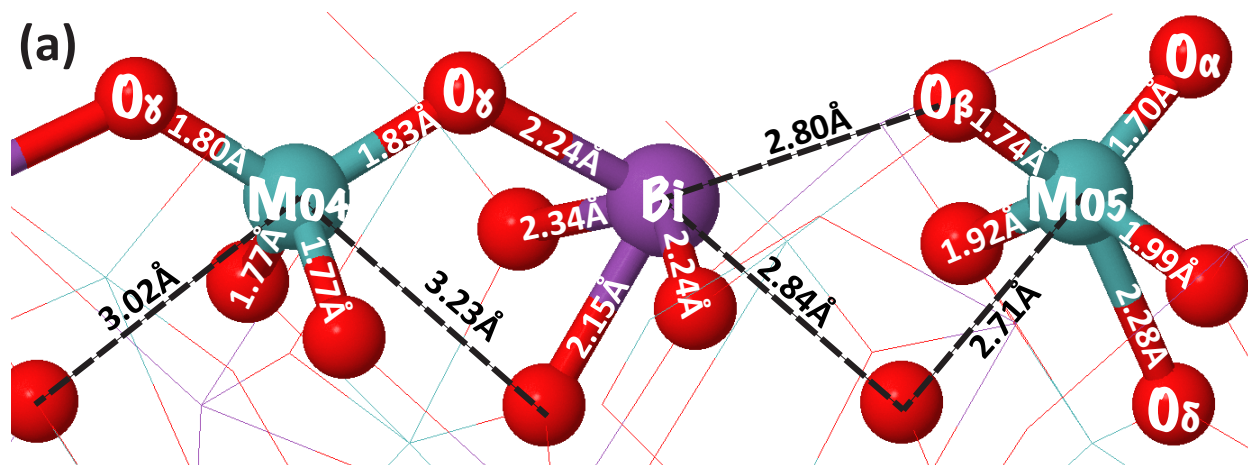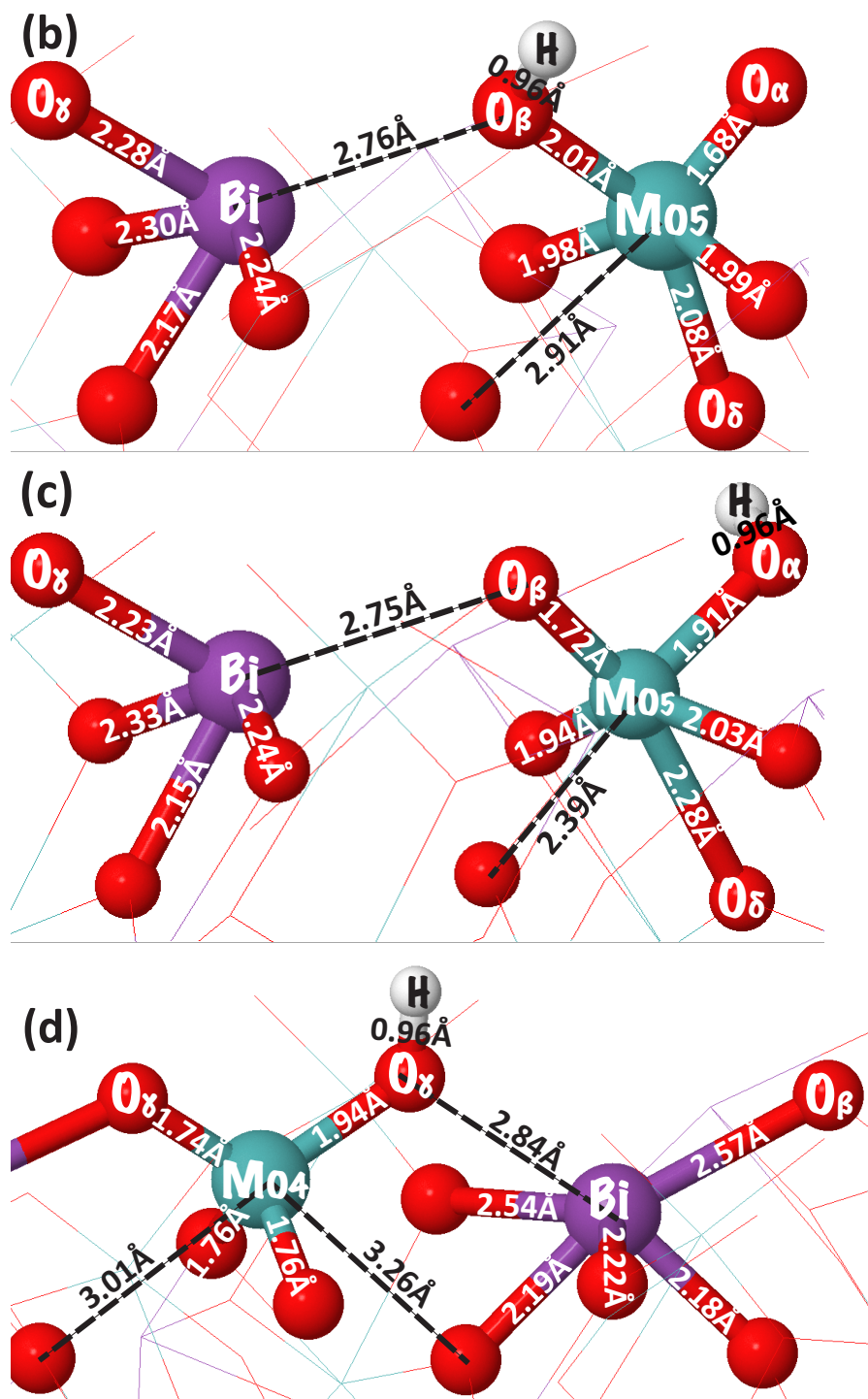
Fig. 3.3 (a) Side view of optimized (010) surface of $Bi_2Mo_3O_{12}$ showing the three distinct types of surface oxygen atoms and the two distinct types of surface molybdenum atoms. (b) After addition of a hydrogen atom to O_β. (c) After addition of a hydrogen atom to O_α. (d) After addition of a hydrogen atom to O_γ. Relevant distances in Å are indicated on the bond or with a dashed line between atoms.

The calculation of a lower barrier for propene activation at O_β vs O_α has been attributed previously to the influence of a neighboring Bi^{3+} cation on the O_β site.[19] The importance of this effect was investigated in greater detail in the present study. Structures were generated in which one surface Bi^{3+} cation in $Bi_2Mo_3O_{12}$ was replaced by another metal cation X, and the surface was allowed to relax. The rest of the $Bi_2Mo_3O_{12}$ structure was fixed in order to isolate the effect of the perturbing element on hydrogen addition to O_β. In addition to Bi^{3+}, which is known to form a stereochemically active lone pair,[56,57] we also investigated the effects of B^{3+}, La^{3+}, Pb^{2+} plus H^+, and Sb^{3+}. The HAE values and X-O_β distances are given in Table 3.3, and structural diagrams are given in Appendix B Figure B.1. The values of the HAE are found to vary only slightly, despite significant differences in the X-O_β distance, the size of the X cation, the coordination geometry of X, the existence of a stereochemically active lone pair on X, and the oxidation state of X. Substitution of B^{3+} is especially telling, as this cation is too small and too far away to have any interaction with O_β, yet the HAE is only 3 kcal/mol higher in energy than that for the native $Bi_2Mo_3O_{12}$. Therefore, it appears that the favorable molybdenum coordination is the principal cause for the low HAE of O_β in $Bi_2Mo_3O_{12}$, and the electronic perturbation by a nearby asymmetrically coordinated cation is only a secondary effect.

Perturbing Element (X)	HAE to O_β [kcal/mol]	X-O_β on oxidized surface [Å]
Bi^{3+}	-58.3	2.80
B^{3+}	-55.5	3.95
La^{3+}	-59.9	2.50
$Pb^{2+} + H^+$	-59.4	2.79
Sb^{3+}	-56.7	3.01

Table 3.3. Hydrogen Attachment Energy (HAE) and X-O_β distance on the oxidized surface for different perturbing elements (X) replacing one surface Bi^{3+} in the (010) surface of $Bi_2Mo_3O_{12}$.

3.3.2 Lead molybdate

Molybdenum atoms in bulk $PbMoO_4$ are tetrahedrally coordinated to four oxygen atoms located at 1.77 Å, and the lead atoms fill the voids between eight tetrahedral units. On the optimized surface, the molybdenum atoms remain symmetric, but move slightly closer to the surface. Per molybdenum, this results in two singly bonded oxygen atoms below the surface and two equivalent doubly bonded oxygen atoms at the surface (O_β) that are electronically perturbed by nearby surface lead atoms, each of which is bound to four subsurface oxygen atoms.

Addition of a hydrogen atom to any of the equivalent surface O_β oxygen atoms distorts the oxygen out of the surface and away from the neighboring lead atom (see Fig. 3.4b). Similarly to what was observed in $Bi_2Mo_3O_{12}$ after hydrogen addition, the molybdenum atom relaxes back towards the next nearest oxygen atom that is *trans* to the oxygen atom where the hydrogen was added. However, since the molybdenum was not initially close to this atom, after surface optimization it is still 2.67 Å away. As seen in Table 3.2, addition of a hydrogen atom to O_β of

PbMoO$_4$ is much less favorable than addition to either O$_\alpha$ or O$_\beta$ of Bi$_2$Mo$_3$O$_{12}$. We attribute this to the inability of the 4-coordinate Mo in PbMoO$_4$ to form a strong association with another oxygen atom upon addition of the hydrogen atom, as explored further below.
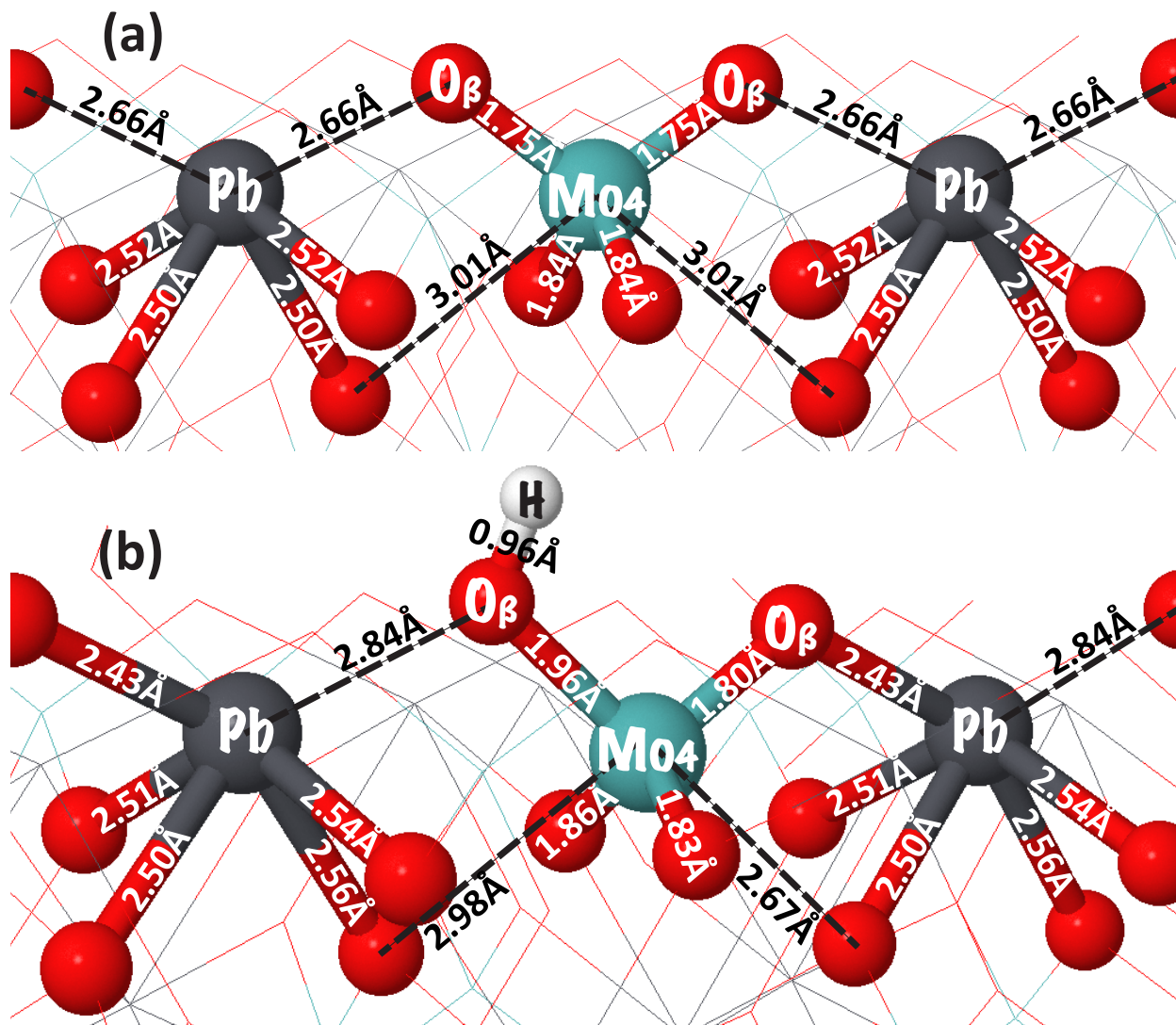

Fig. 3.4 (a) Side view of the fully oxidized surface of PbMoO$_4$. (b) The same view after hydrogen addition to one of the equivalent O$_\beta$ atoms. Relevant distances in Å are indicated on the bond or with a dashed line between atoms.
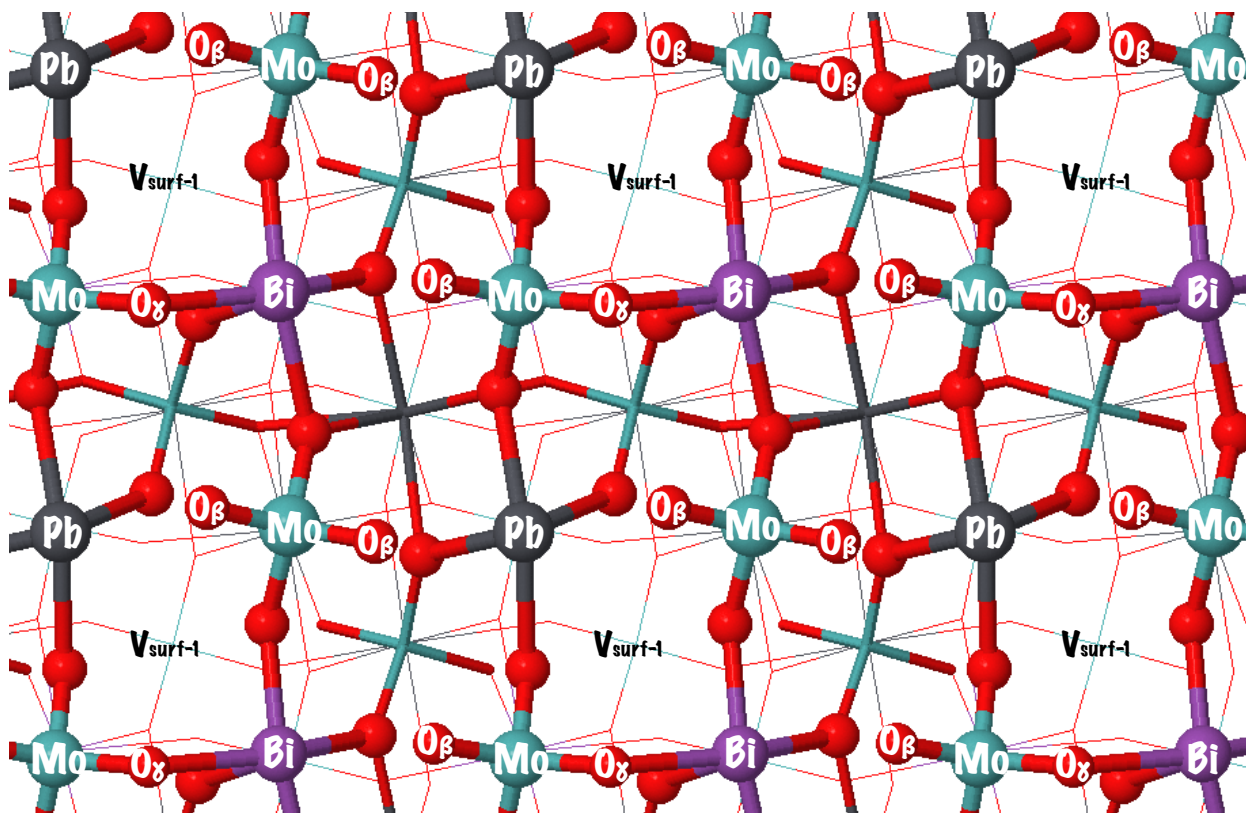
3.3.3 Bismuth/lead mixed molybdate

Fig. 3.5 Top down view of $Bi_2Pb_5Mo_8O_{32}$, where Mo atoms are turquoise, Bi are purple, Pb are grey, and O are red, and the location of cation vacancies one layer below the surface are indicated by V_{surf-1}. Surface atoms are identified in white (see Table 3.1 for explanation of oxygen types).

We built a mixed bismuth lead molybdate with the formula $Bi_2Pb_5\varphi_1Mo_8O_{12}$ (φ = cation vacancy) to explore the effect of distorting the pure scheelite $PbMoO_4$. As shown in Figure 3.5, this material contains 1:1 ratio of bismuth to lead at the surface, with alternating rows of molybdenum/lead and molybdenum/bismuth. The lattice contains 50% cation vacancies in the layer below the surface (indicated in Fig. 3.5 by V_{surf-1}), a 1:1 ratio of bismuth to lead in the layer below that, and a full complement of lead cations in the bottom most layer. Note that, since no monoclinic distortion was observed spectroscopically in mixed bismuth lead molybdates with similar concentrations,[47] we constrained the $Bi_2Pb_5\varphi_1Mo_8O_{12}$ to remain in a tetragonal unit cell similar to that of the parent $PbMoO_4$.

Figure 3.6a shows a side view of both a lead-molybdenum row and a bismuth-molybdenum row at the surface of $Bi_2Pb_5Mo_8O_{12}$. The surface molybdenum atoms are 4-coordinate, though somewhat distorted from the symmetric tetrahedra observed in the parent $PbMoO_4$. Both bismuth and lead are observed to have an asymmetrical coordination at the surface, with bismuth bonded to five oxygen atoms and lead to four. However, since lead is a

larger cation than bismuth, it has significantly longer bonds to its neighboring oxygen atoms and thus ends up modifying the neighboring molybdate unit differently than does bismuth. Molybdenum atoms in the lead row have two doubly bonded surface oxygen atoms that are both electronically perturbed by neighboring lead atoms, but are not equivalent and are therefore designated O_β' and O_β". Molybdenum atoms in the bismuth row have a single bond to a surface bridging oxygen atom also bound to bismuth (O_γ) and one doubly bonded oxygen atom electronically perturbed by a neighboring bismuth atom (O_β).

The HAE values for all four types of surface oxygen atoms are given in Table 3.2 and the geometry for the lowest energy O_β' in Figure 3.6b (geometries for the remaining structures are in Appendix B Fig. B.2). Upon hydrogen addition to O_β', the surface undergoes significant geometric distortion such that the molybdenum draws 0.6 Å nearer to an oxygen atom *trans* to O_β' and thus is able to loosely coordinate with it. Even though the molybdenum environment in the lead row of $Bi_2Pb_5Mo_8O_{12}$ starts very similar to the molybdenum environment in $PbMoO_4$, the additional flexibility in the former crystal, due to the introduction of vacancies and the different ionic radii of Bi^{3+} and Pb^{2+}, allows the molybdenum to move and therefore adopt a more favorable conformation upon hydrogen addition. The importance of the geometric distortion with hydrogen addition is obvious from the 7 kcal/mol difference in HAE between hydroxyl relaxation only and full surface relaxation. The HAE value for addition to O_β' is similar to the hydroxyl-relaxation-only HAE for addition to O_β of $Bi_2Mo_3O_{12}$, which without surface relaxation has a similar geometry to the geometry attained after full surface relaxation of hydrogen addition to O_β'.
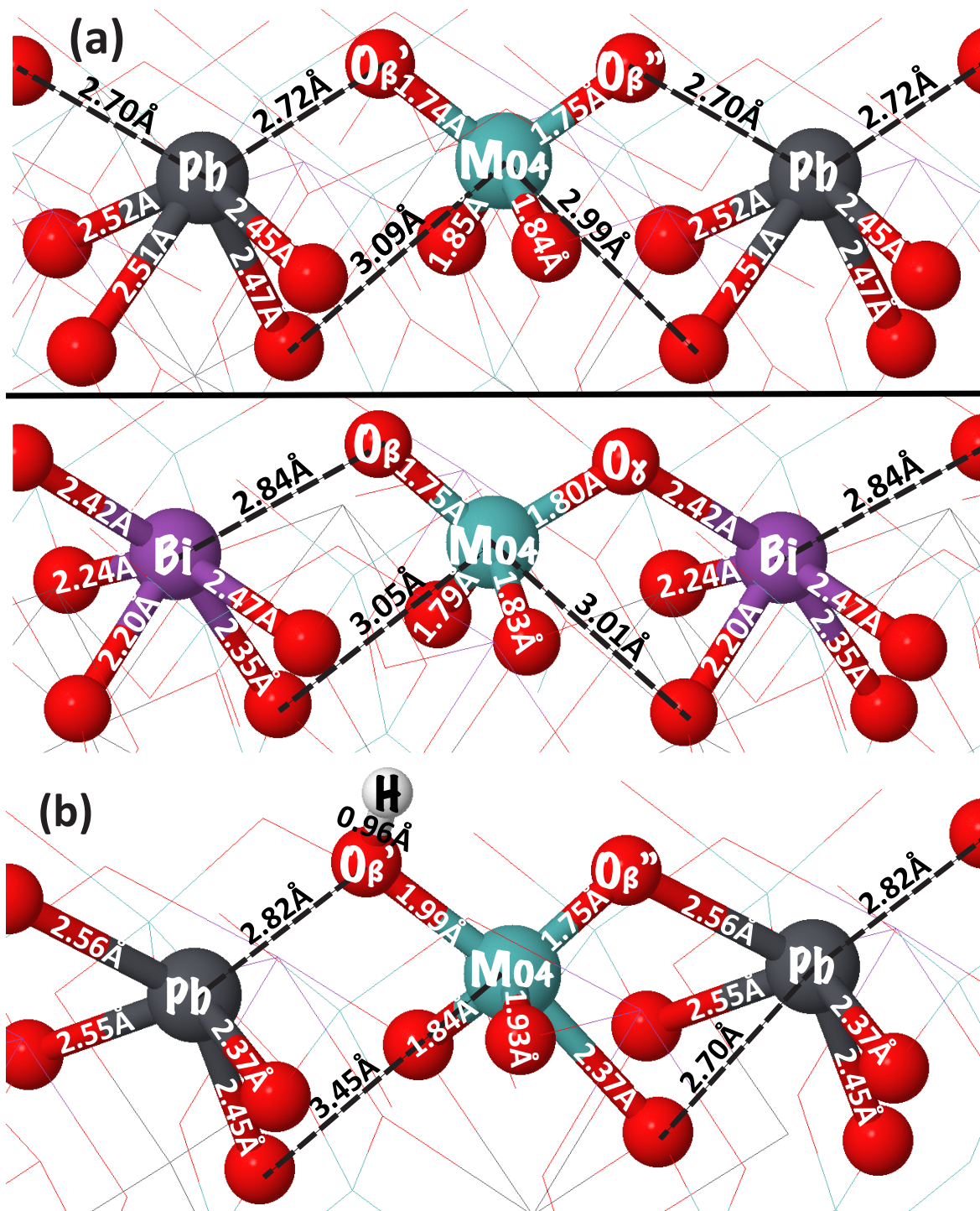
Fig. 3.6 (a) Side view of both a Pb row (top) and a Bi row (bottom) on the fully oxidized surface of $Bi_2Pb_5Mo_8O_{32}$ showing the four different types of surface oxygen atoms (b) Pb row after one hydrogen addition to O_β'. Relevant distances in Å are indicated on the bond or with a dashed line between atoms.

3.3.4 Molybdenum trioxide

Molybdenum trioxide, MoO_3, has a completely different structure than the pure and distorted scheelite mixed-metal oxides discussed above. In the bulk, molybdenum atoms have an octahedral geometry, with two doubly bound oxygen atoms, two singly bound oxygen atoms, and two loosely coordinated oxygen atoms. This remains true for the fully oxidized surface (Fig. 3.7a), which is terminated by pure doubly bonded oxygen atoms protruding out of the surface (O_α). The other doubly bonded oxygen (O_β) is in the surface plane and is loosely coordinated to neighboring molybdenum and thus electronically perturbed by it. Each surface molybdenum atom is loosely coordinated to a sixth oxygen underneath it (O_δ) that is doubly bonded to the molybdenum one layer below the surface. These equivalent 6-coordinate molybdenum surface units are located at the vertices of a ~3.9 Å square grid.

As shown in Figure 3.7b, upon hydrogen addition to the protruding O_α, the molybdenum atom it is bound to sinks into the surface of the catalyst, resulting in a 0.24 Å shorter bond to the O_δ beneath the surface. This action leaves each molybdenum atom with a planar double bond to O_β, and partial or single bonds to the five remaining surrounding oxygen atoms, including the O_α where the hydrogen was added. The energy for hydrogen addition is -58.2 kcal/mol (see Table 3.2), the same as the energy for hydrogen addition to O_β of $Bi_2Mo_3O_{12}$. However, the former has a much more negative HAE when the surface is frozen and only the hydroxyl group is allowed to relax (bracketed numbers in Table 3.2). Therefore, the O_α on the 6-coordinate molybdenum of MoO_3 is the better intrinsic hydrogen addition site, but the conformational flexibility in $Bi_2Mo_3O_{12}$ allows that O_β to achieve a similar HAE.

In Figure 3.7c, we present the optimized geometry after hydrogen addition to O_β, which has the lowest HAE by 5 kcal/mol of any oxygen we tested. However, since we are using a square unit cell with 4 surface molybdenum atoms, some of this ability to rearrange and thus attain a low energy is an artifact of the periodic boundary conditions. The actual HAE for a single hydrogen atom at this position if there were no periodicity should be significantly higher than the value we calculate, reflected in the very high HAE for hydrogen addition when only the hydroxyl is allowed to relax. Additionally, O_β will not be accessible to propene, since propene is too large to fit between the O_α atoms that protrude from the surface without experiencing large repulsive interactions with the aforementioned oxygen atoms. Therefore, because it should not be physically relevant and our calculations likely over estimate its HAE significantly, we do not consider propene reaction at O_β, only at O_α.
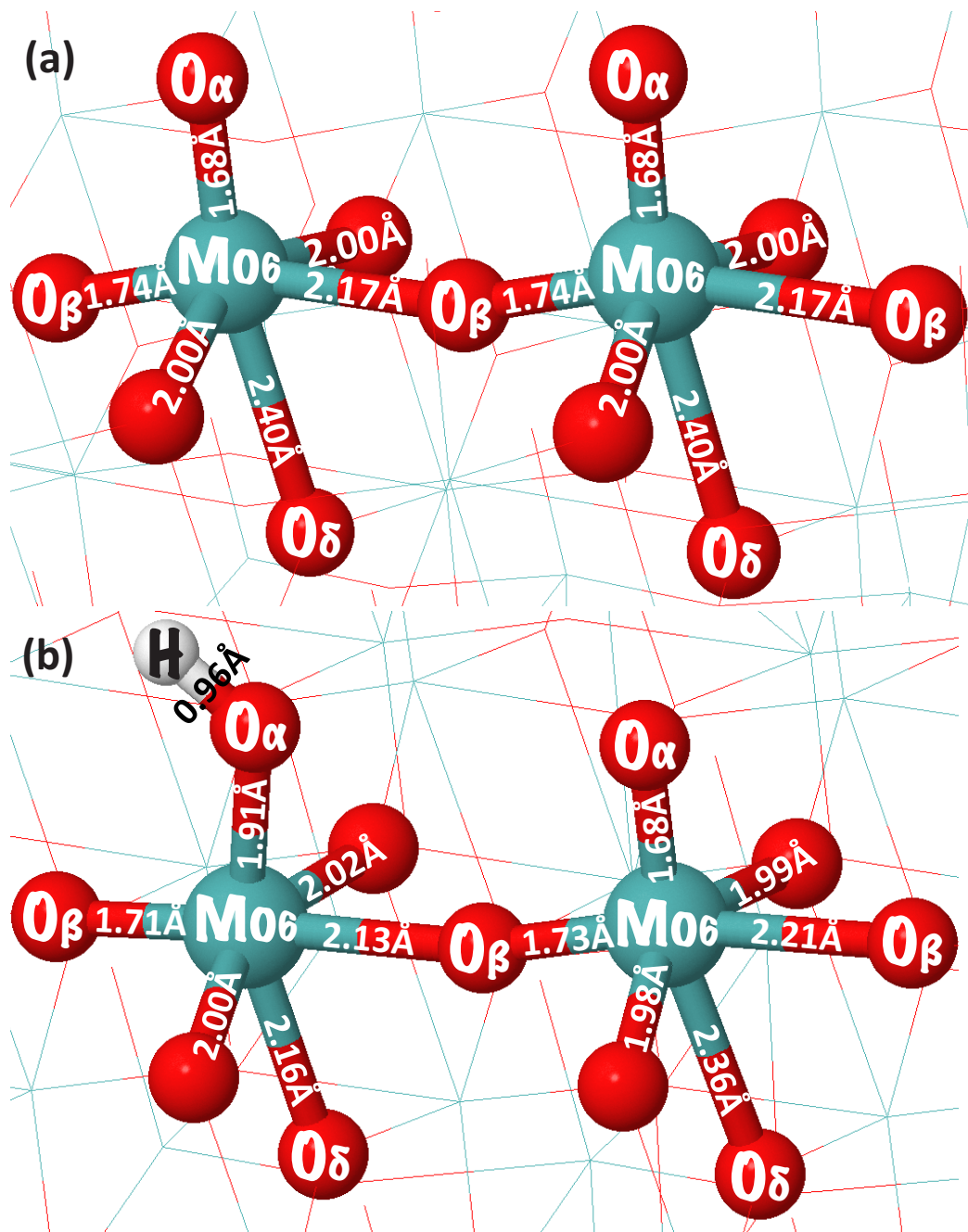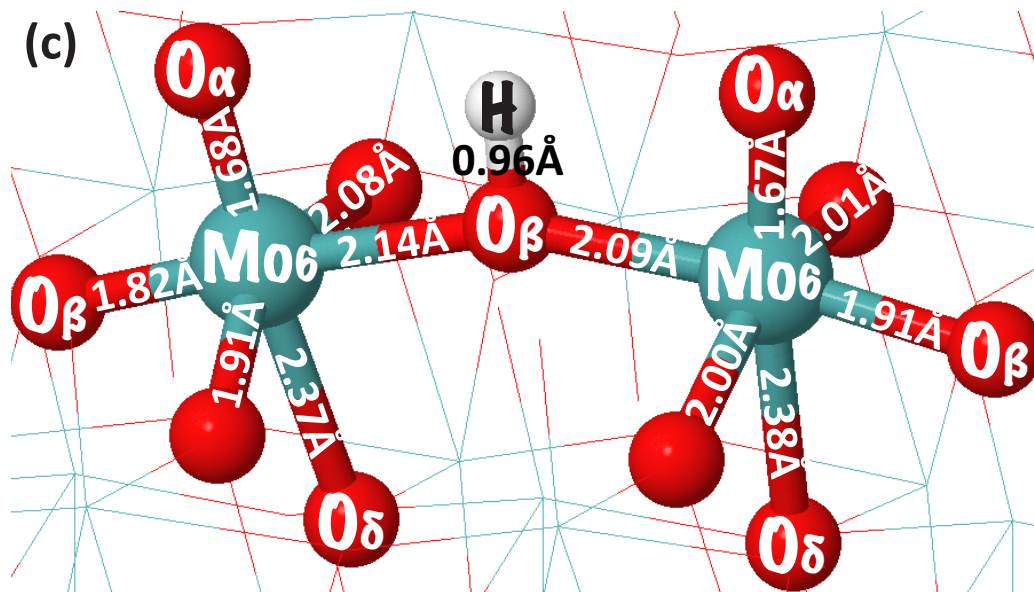
Fig. 3.7 (a) Side view of the fully oxidized surface of MoO_3. (b) The same view after hydrogen addition to one of the equivalent O_α atoms. (c) The same view after hydrogen addition to one of the equivalent O_β atoms. Relevant distances in Å are indicated on the bond

3.4 Molecular orbital analysis

In this section representative molybdenum cluster calculations are used to develop a deeper understanding for why oxo groups on 5-coordinate molybdenum atoms have a more negative energy for hydrogen addition than do 4-coordinate molybdenum atoms. For this analysis a 4-coordinate molybdenum unit $MoO_2(OH)_2$ is allowed to interact with a molecule of dimethyl ether (DME = $O(CH_3)_2$) to ultimately form a 5-coordinate unit $MoO_2(OH)_2$-$O(CH_3)_2$. The oxygen atom of DME, O_δ, is oriented so that it interacts with the molybdenum via its oxygen atom as shown in Figure 3.8. The orientation of DME relative to the $MoO_2(OH)_2$ fragment is not constrained geometrically and is defined by the lowest energy configuration. Interaction of DME with $MoO_2(OH)_2$ results in two distinct molybdenyl oxo groups, one cis to the DME (O_{Cis}) and one *trans* to the DME (O_{Tr}), as noted in Figure 9. The 4-coordinate cluster is representative of the molybdenum coordination environment in $PbMoO_4$, while the 5-coordinate cluster is representative of the molybdenum coordination environment in $Bi_2Mo_3O_{12}$.

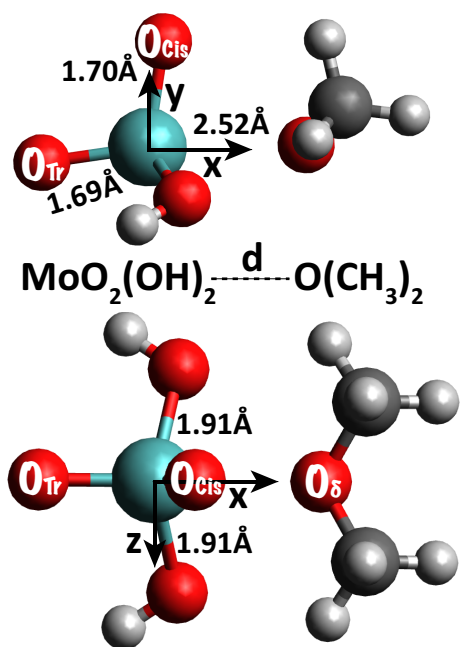Fig. 3.8 Two views (top: xy plane, bottom: xz plane) of the 5-coordinate $MoO_2(OH)_2$-$O(CH_3)_2$ model cluster used to analyze the frontier molecular orbitals. The 4-coordinate cluster is the molybdate unit optimized without the $O(CH_3)_2$ molecule.

Figure 3.9 shows how the system energy changes as the DME moves from infinity towards the 4-coordinate molybdate cluster to create a 5-coordinate molybdate cluster, both for the cases of no addition and addition of a hydrogen atom to O_{Tr}. As can be seen in Figure 3.8, the length of a molybdenum-oxygen double bond is ~1.7 Å and that of a single bond ~1.9 Å. Figure 3.9 therefore depicts the range of Mo-O_δ distances between a full single bond and no interaction. For distances greater than ~ 3.0 Å, the relative energies of the cluster before and after hydrogen addition are similar, and in both cases the energy decrease relative to the 4-coordinate cluster is mainly due to non-specific van der Waals type interactions between the molybdate unit and the DME. However, for distances less than ~ 3.0Å, we observe mixing between orbitals centered on the molybdate unit and orbitals centered on O_δ of DME, indicative of a specific interaction between the two (see below).

For the $MoO_2(OH)_2$-$O(CH_3)_2$ cluster with Mo-O_δ distances < 3.0Å, repulsion between electrons on O_δ and electrons on the $MoO_2(OH)_2$ unit results in the energy profile reaching a minimum and then increasing sharply. However, after hydrogen addition to the O_{Tr} oxygen atom of the $MoO_2(OH)_2$-$O(CH_3)_2$ cluster, interaction between O_δ and the molybdate is favorable, resulting in a 11 kcal/mol decrease in the relative energy as the Mo-O_δ distance decreases from 3.0 Å to 2.2 Å. Note that the curves in Figure 3.9 are shown on the same scale for ease of comparison, but on an absolute energy scale would be offset by the HAE of the reference 4-coordinate molybdate cluster, -39.6 kcal/mol. Therefore, as indicated on the plot, the energy difference between the two curves is the ΔHAE relative to the reference compound. By

considering the ΔHAE, it is clear that the HAE decreases monotonically from -39.6 kcal/mol with decreasing Mo-O_δ distance, since the cluster after hydrogen addition is always more stabilized by the presence of DME than is the cluster before hydrogen addition.
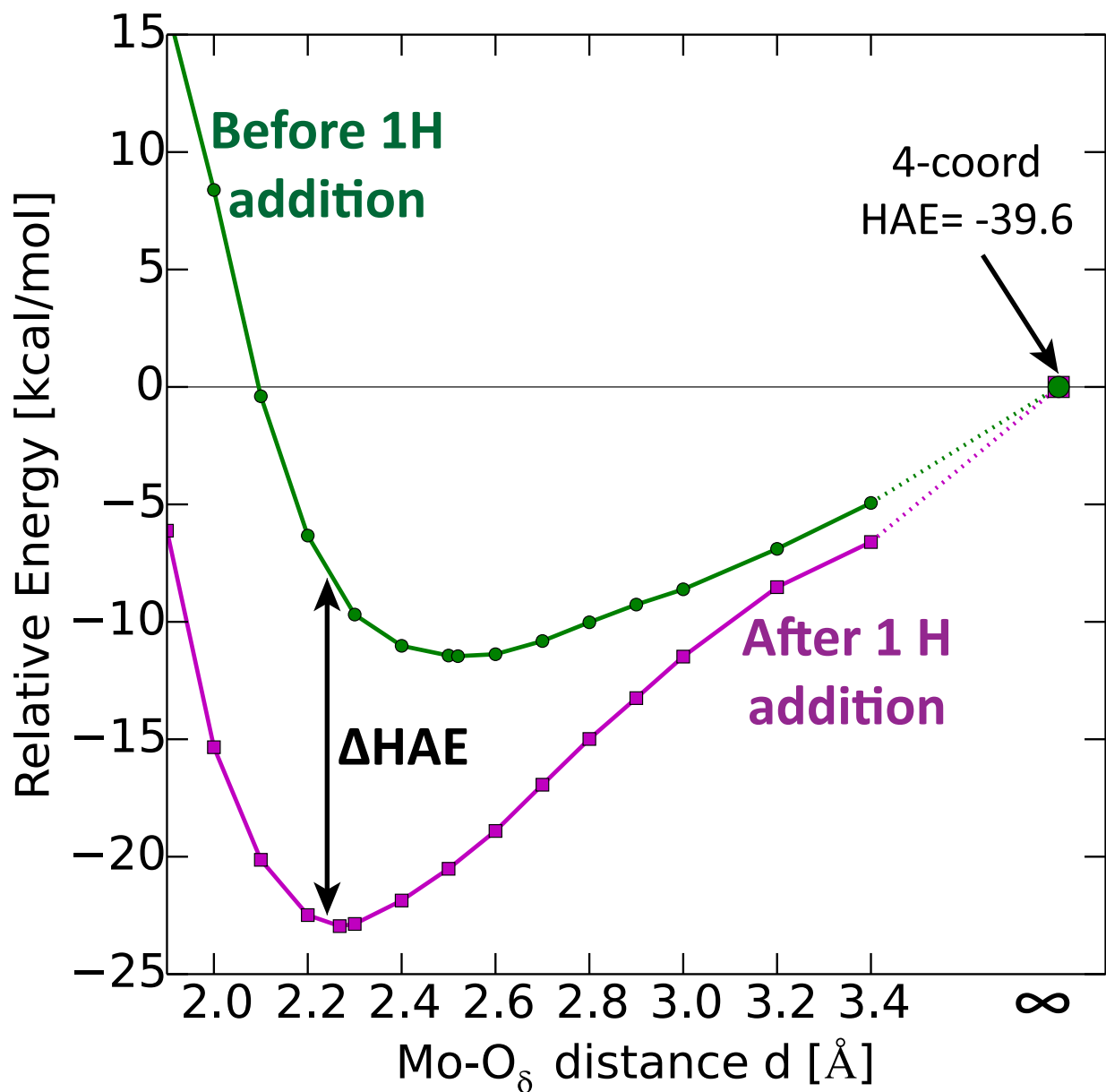
Fig. 3.9 Energy for the 5-coordinate molybdate cluster both before and after hydrogen addition as a function of Mo-O_δ distance. For each case, the plotted energy is relative to the energy of the 4-coordinate molybdate cluster before or after hydrogen addition, respectively, plus the energy of DME.

To further elucidate why the approach of DME to Mo has different effects on the cluster before and after hydrogen addition, we applied the Born-Haber cycle approach summarized in

Figure 3.10a and explained in greater detail in our previous work.[22] In this approach, the HAE can be represented as the sum of three components: (1) the energy (E_{Geom}) to move the atoms from their initial positions prior to hydrogen addition to their final positions after addition, (2) the energy (E_{Hyb}) to rehybridize the molybdenum-oxygen double bond from the singlet spin state to the triplet spin state with the atom positions held constant in their final positions, and (3) the energy (E_{OH}) to bring a hydrogen radical from infinity and add it to the cluster, which already has the atoms in their final positions, thereby forming a spin-doublet molybdenum hydroxyl group. Figure 3.10b illustrates how the values of these three components change with Mo-O_δ distance. The component with the largest change upon coordination with DME is E_{Hyb}, followed by E_{Geom}, and finally E_{OH}.
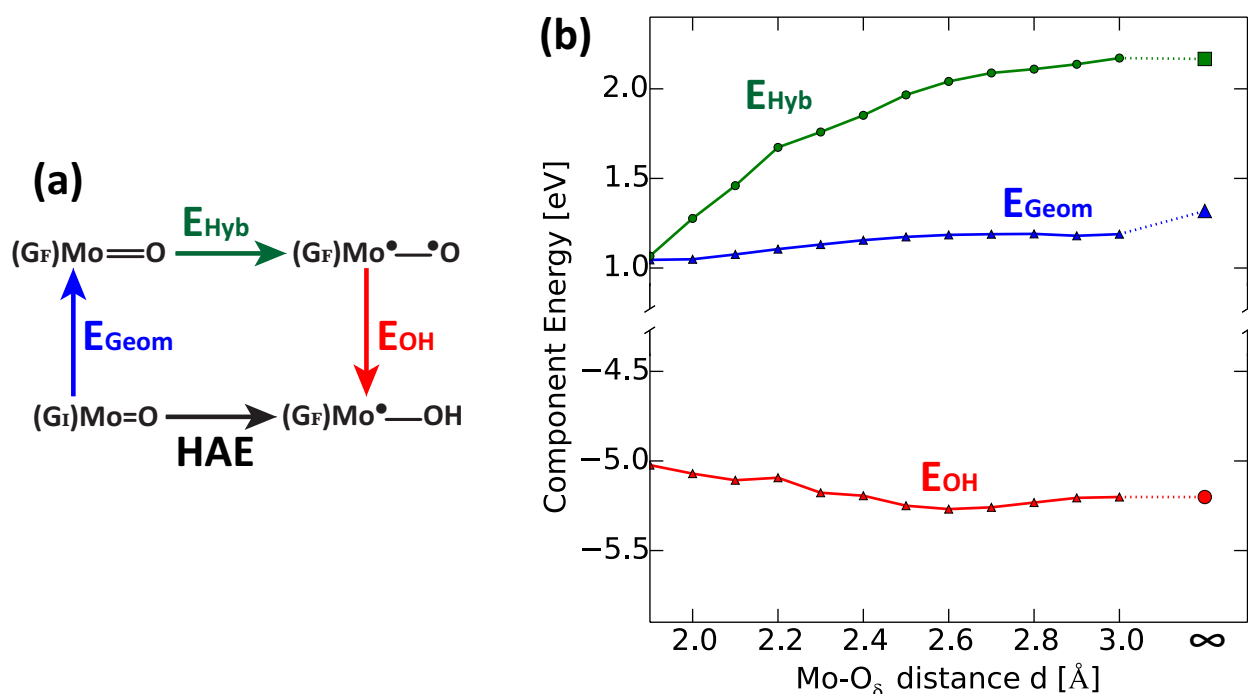

Fig. 3.10 (a) HAE decomposition into components E_{Geom}, E_{Hyb}, and E_{OH}. (b) Plot of these components versus Mo-O_δ distance.

E_{Hyb}, is directly related to the energy difference between the relevant highest occupied molecular orbital (HOMO) and the relevant lowest unoccupied molecular orbital (LUMO). In Figure 3.11, we show the energy of the frontier molecular orbitals as a function of Mo-O_δ distance. There are 5 specific molecular orbitals that are important, labeled A, B', B'' C, and D. Electron density plots for these 5 types are shown on the right of Figure 3.11. Molecular orbital type A is comprised mainly of O_{Tr} p_y and O_{Cis} p_x lone pair orbitals and is the HOMO for the 4-coordinate molybdate cluster. Molecular orbital type C is comprised mainly of O_δ p_x and is the HOMO for DME. Molecular orbital type B' and type B'' are both hybrid molecular orbitals that result from mixing types A and C as the Mo-O_δ distance decreases. Note that, at d=2.9Å (see Fig. 3.11), B' and B'' appear very similar, but they diverge in both character and energy as d

decreases. Type B' always has more type A character and is always higher in energy than type B", which has more type C character. Type B' is therefore the HOMO for the 5-coordinate cluster at Mo-O_δ distances ≤2.9 Å and is higher in energy than the molybdate HOMO (A) because of orbital mixing with the p orbital on the approaching O_δ. Finally, orbital type D is a π anti-bonding orbital between Mo d_{xz} and O_{Tr} p_z and is the LUMO for both 4- and 5-coordinate molybdate clusters. Figure 3.11 identifies the HOMO-LUMO energy differences for two relevant species: the isolated 4-coordinate molybdate (2.88 eV) and a 5-coordinate molybdate with Mo-O_δ distance 2.27 Å (2.47 eV).
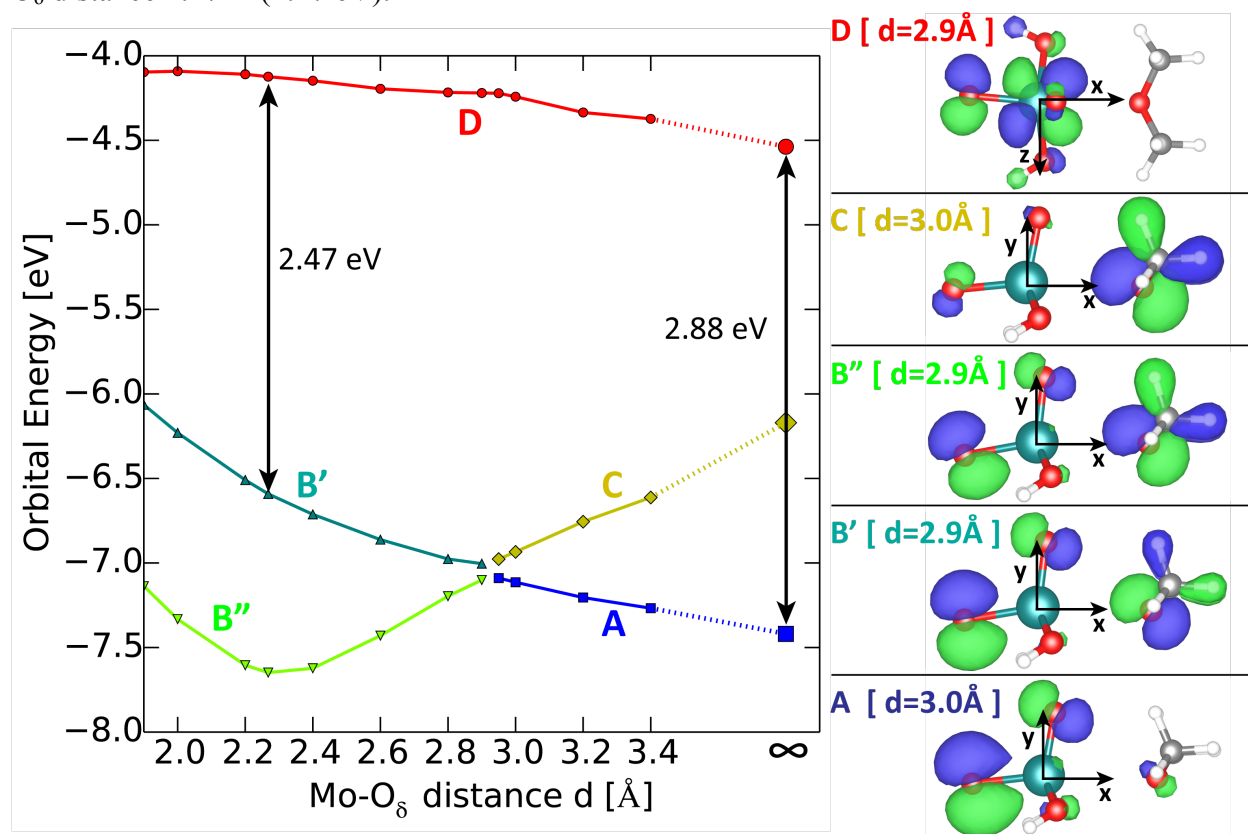

Fig. 3.11 Highest occupied molecular orbital (HOMO) and lowest unoccupied molecular orbital (LUMO) energies as a function of the distance from the oxygen atom in DME (O_δ) to the molybdenum atom in the $MoO_2(OH)_2$ cluster. These calculations are for geometries optimized after hydrogen addition to the oxygen *trans* to the DME (O_{Tr}), then frozen in place, the hydrogen removed and the orbital energies calculated in the singlet state. The orbital pictures shown on the right are for d = 2.27 Å. d = ∞ is for the optimized 4-coordinate $MoO_2(OH)_2$ cluster.

It is evident from Figure 3.11 that orbital mixing between the higher energy O_δ p_x (C) molecular orbital and the lower energy O_{Tr} p_y plus O_{Cis} p_x (A) molecular orbital results in two combined molecular orbitals (B' and B") that have intermediate energy. Importantly, the combined orbital B' that is the HOMO for the 5-coordinate cluster (with d ≤2.9 Å) is higher in energy than that of the unmixed orbital (A) that is the HOMO for the 4-coordinate cluster, and increases in energy with decreasing Mo-O_δ distance. The LUMO also increases slightly in

energy as DME is brought towards the molybdate, but the influence is much weaker than for the HOMO, and therefore the HOMO-LUMO gap decreases monotonically with decreasing distance. The HOMO-LUMO gap is directly related to E_{Hyb}, which, as shown in Figure 3.10, is the component of the HAE that changes most significantly with Mo-O$_\delta$ distance. Therefore, addition of a fifth oxygen to the molybdate coordination sphere (Mo-O$_\delta \leq 2.9$ Å) results in a more negative HAE because of orbital mixing between the molybdate cluster and the additional oxygen.

We further note that the same orbital mixing effect is observed in the cluster before hydrogen addition. Again, the mixed type B' cluster HOMO increases in energy with decreasing distance. In doing so, it raises the energy of the cluster itself. This explains why the interaction energy between DME and the molybdate prior to hydrogen addition reaches a minimum and then increases in energy as DME enters the coordination sphere (see Fig. 3.9).

Up to this point in the discussion of the cluster calculations, we have only considered hydrogen addition to O$_{Tr}$, the oxygen that is *trans* to the DME. For hydrogen addition to O$_{Cis}$ with d=2.392Å (the optimal Mo-O$_\delta$ distance after H addition to O$_{Cis}$), $E_{Geom} = 1.06$ eV, $E_{Hyb} =$ 2.28 eV, and $E_{OH} = -4.92$ eV. These sum to give an HAE of -36.4 kcal/mol, which is slightly less negative than the HAE for the 4-coordinate molybdate cluster (-39.6 kcal/mol), and significantly less negative than the HAE for addition to O$_{Tr}$ at the same Mo-O$_\delta$ distance (-50.4 kcal/mol). During H addition to either O$_{Tr}$ or O$_{Cis}$, an electron is promoted from the type B' HOMO to the type D LUMO. However, when H is added to O$_{Tr}$ the Mo=O$_{Tr}$ bond lengthens (1.694Å $\rightarrow$ 1.930Å), while when H is added to O$_{Cis}$, the Mo=O$_{Cis}$ bond lengthens (1.699Å $\rightarrow$ 1.925Å). Lengthening either bond increases the energy of the type B' HOMO and decreases the energy of the type D LUMO, however to different extents for O$_{Tr}$ and O$_{Cis}$. As shown in Appendix B, Figure B.3 for a fixed Mo-O$_\delta$ distance d=2.392Å, lengthening the Mo=O$_{Tr}$ bond to its optimal length after H addition results in an overall lower HOMO-LUMO gap than does lengthening the Mo-O$_{Cis}$ bond to its optimal length after H addition. This is due to a larger decrease in the LUMO energy for stretching the Mo=O$_{Tr}$ bond, which has more π anti-bonding overlap between the Mo d$_{xz}$ orbital and the O$_{Tr}$ p$_z$ orbital than between the Mo d$_{xz}$ orbital and the O$_{Cis}$ p$_z$ orbital (see Fig. 3.11 type D orbital depiction). Since the E_{Hyb} is calculated after Mo=O bond lengthening, the E_{Hyb} of addition to O$_{Tr}$ is lower than the E_{Hyb} of addition to O$_{Cis}$. In addition, as also shown in Figure B.3, the type B' HOMO is higher in energy after lengthening O$_{Cis}$ its final length than after lengthening O$_{Tr}$ to its final length. Since the H electron goes into this type B' orbital in order to form the O-H bond (after one electron is promoted from the type B' HOMO to the type D LUMO in the rehybridization step), a higher energy type B' orbital results in a less favorable O-H bond. Therefore, the less negative E_{OH} and more positive E_{Hyb} of addition to O$_{Cis}$ relative to addition to O$_{Tr}$ are both due to the different effects on the orbital energies upon stretching Mo=O$_{Cis}$ and stretching Mo=O$_{Tr}$, and sum to result in a less negative HAE.

By extracting the components of the HAE for hydrogen addition to O$_{Cis}$, we determined that E_{Hyb} is 2.28 eV in this case, which is higher than the value for the 4-coordinate molybdate, 2.17 eV. This high value of E_{Hyb} is a result of promotion of an electron from the mixed type B'

HOMO to a LUMO that not only has significant π anti-bonding between Mo d_{xz} and O_{Tr} p_z, but that also has substantial π anti-bonding between Mo d_{xz} and O_{Cis} p_z.

We have also considered a 6-coordinate molybdate cluster where the primary $MoO_2(OH)_2$ unit is coordinated with two DME molecules, one on each side such that the doubly bound oxygen atoms are essentially equivalent. The HAE on the 6-coordinate cluster optimized before and after hydrogen addition is -49.8 kcal/mol, which is close to the HAE for a 5-coordinate cluster optimized before and after hydrogen addition (-51.1 kcal/mol). This result is consistent with findings discussed in the previous paragraph, namely that adding an oxygen donor to the coordination sphere in a position *trans* to a molybdenyl oxo renders the HAE on that oxo significantly more negative, but has little impact on the HAE of the oxo that is cis to the additional oxygen. Therefore, since both molybdenyl oxo groups in the 6-coordinate cluster have donor oxygen atoms in a *trans* positions, both exhibit low HAE values similar to that of O_{Tr} in the 5-coordinate cluster.

The insights gained from the cluster calculations help to explain what is observed before and after hydrogen addition to the surface of bulk molybates presented in Section 3.4. As mentioned there, upon hydrogen addition, molybdenum always relaxes towards the closest oxygen that is *trans* to the location of the oxygen atom to which the hydrogen was added. This change can be understand in the context of the cluster calculations by recalling that the presence of an additional oxygen atom in the coordination sphere around Mo is energetically unfavorable before hydrogen addition, but energetically favorable after hydrogen addition.

Because of the energetic penalty for introducing an additional oxygen atom into the coordination sphere of molybdenum, bulk mixed metal molybdates would be expected to always form low-energy 4-coordinate MoO_4^{2-} units spaced between charge compensating cations. Indeed, most mixed metal molybdates, including $PbMoO_4$, $La_2Mo_3O_{12}$, $Ce_2Mo_3O_{12}$ and $Eu_2Mo_3O_{12}$, exhibit only 4-coordinate molybdenum atoms, even when vacancies are present that distort the scheelite structure. Since these materials have molybdenum in its most favorable coordination environment, they will have much higher HAE values than materials that have additional oxygen atoms in the molybdenum coordination sphere. In all of the structures listed above, the next closest oxygen atom to any molybdenum atom (after its 4 coordinated oxygen atoms) is at least 2.9 Å away, and therefore would require significant structural distortion upon hydrogen addition in order to achieve a substantial decrease in HAE. In the case of $PbMoO_4$, such structural distortion must not be energetically feasible, since, in the optimized geometry after hydrogen addition (Fig. 3.4b), the molybdenum is still 4-coordinate and the HAE is only -44.0 kcal/mol. However, in the case of $Bi_2Pb_5Mo_8O_{32}$, the vacancies that result from replacing Pb^{2+} with Bi^{3+} allow for more distortion, and therefore, after addition to O_β', the molybdenum is able to coordinate slightly with a bulk oxygen, thereby making the HAE more negative by 4 kcal/mol relative to $PbMoO_4$ O_β.

By contrast, $Bi_2Mo_3O_{12}$ has exclusively 5-coordinate molybdenum units in the bulk crystal, two thirds of which remain 5-coordinate on the (010) surface. We also note that β-$Bi_2Mo_2O_9$ and γ-Bi_2MoO_6, which have propene oxidation activities similar to that of α-

Bi$_2$Mo$_3$O$_{12}$,[4,5] have molybdenum atoms in the bulk that have more than 4 oxygen atoms in their coordination sphere. It is less obvious what surface structures these materials present, but at least some of the surface molybdenum atoms are likely to retain their high coordination number. As shown by the molecular orbital analysis presented above, locating an additional oxygen atom *trans* to the oxygen to which the hydrogen atom is added and close to the molybdenum atom allows for orbital mixing that increases the energy of the HOMO. This results in more highly coordinated Mo cations that are higher in energy, but also have a more negative HAE. As mentioned above, 5- and 6-coordinate molybdenum clusters have comparable HAE values for the oxo group(s) *trans* to a coordinated oxygen atom, therefore metal oxide materials with more highly coordinated molybdenum atoms should exhibit similar HAE values that are higher than those of materials with only 4-coordinate molybdenum atoms. We note that, indeed, Bi$_2$Mo$_3$O$_{12}$ O$_\beta$, which is *trans* to an oxygen on a 5-coordinate Mo, and MoO$_3$ O$_\alpha$, which is *trans* to a oxygen on a 6-coordinate Mo, have identical HAEs. Addition to O$_\alpha$ of Bi$_2$Mo$_3$O$_{12}$ results in a quasi-6-coordinate Mo after optimization, but the Mo distance from the oxygen *trans* to O$_\alpha$ is significantly further than in the former cases, resulting in a somewhat less favorable HAE.

From this analysis, we discover that an important role of bismuth in making bismuth molybdates active catalysts for propene oxidation and ammoxidation is to force Mo^{6+} cations into a higher energy, higher coordination configuration, thereby facilitating acceptance of a hydrogen atom from propene by a Mo=O group.

3.5 Reaction of propene

In this section, we consider the effect of propene adsorption to an oxidized surface and the reaction energy to move one hydrogen atom from the methyl group of adsorbed propene to the most active surface oxygen atom. In every case, the physisorbed propene is oriented such that one of the hydrogen atoms on the methyl group is pointed toward the oxygen atom that will accept the H atom resulting from the cleavage of a C-H bond. For all materials, the final distance between the H and O atom that will abstract it is in the range of 2.2-2.5 Å. Reference will be made to the ΔE_{ads} values listed in Table 3.5 and to the energy levels depicted in Figure 3.12. In the discussion below, the initial state for each material is a bare oxidized surface and propene in the gas phase (the zero energy reference point) and the final state is the surface with one hydrogen atom added to the oxygen atom indicated in Table 3.5 and a physisorbed allyl radical.

3.5.1 Propene adsorption

As mentioned in Section 3.3.1, bismuth cations on the surface of Bi$_2$Mo$_3$O$_{12}$ are under-coordinated compared to their desired coordination in the bulk. Because of this, they are good sites for adsorbing gas-phase molecules that can donate electron density via a dative type bond to Bi^{3+}. From DFT calculation results, we have recently reported that surface bismuth cations on the (010) surface of Bi$_2$Mo$_3$O$_{12}$ can favorably adsorb both ammonia, via σ-donation from the lone pair on nitrogen, and propene, via donation of π electron density from the carbon-carbon double bond.[6,17] Additionally, this is a good adsorption site because the bismuth cations are close to the

surface and there is space on either side where the methyl group of propene can sit without encountering repulsive interactions with surface oxygen anions. The calculated the energy for propene adsorption at this site is -11.5 kcal/mol and the distance between the bismuth cation and the midpoint of the carbon-carbon double bond is 3.33 Å, with the double bond situated directly above the bismuth cation. Since the acceptor 6p orbitals on bismuth are large and diffuse, propene can be situated anywhere within a ~2x2 Å square parallel to the surface at a distance of 3-3.5Å above Bi^{3+} and maintain a $\Delta E_{ads,C3H6} < -10$ kcal/mol. As a consequence, the entropy loss upon adsorption is not as large as it would be for a more localized mode of adsorption.

Similarly, propene can adsorb above Pb^{2+} on the surface of $PbMoO_4$, since these cations are also under-coordinated compared to the environment in the bulk. However, these sites are less favorable for propene adsorption than the Bi^{3+} sites in $Bi_2Mo_3O_{12}$ by 4 kcal/mol (see Table 3.5). This difference is attributable to the fact that the lead cations in lead molybdate are not as close to the surface as the bismuth cations are in bismuth molybdate, and the former material has more surface oxygen anions at shorter distances that interact repulsively with the adsorbed propene. Additionally, the lower charge on the lead cations results in them being weaker Lewis acids than bismuth cations.

The mixed bismuth/lead molybdate has stronger propene adsorption sites than the pure lead molybdate, with adsorption energies comparable to those on $Bi_2Mo_3O_{12}$ (see Table 3.4). For this material, the propene adsorbs over surface Bi^{3+} cations one row over from the most active O_β', which is in the Pb^{2+} row. This orientation is very similar to the orientation in $Bi_2Mo_3O_{12}$ and is a favorable geometry for hydrogen abstraction.

Finally, propene adsorption on molybdenum trioxide is not favorable, as is obvious from the very low calculated energy of adsorption of -1.8 kcal/mol. This is because the surface of MoO_3 is covered by oxygen O_α anions, whose lone pair will have repulsive interactions with propene. Propene is too large (approximately 3 Å x 4 Å) to fit in the spaces of the 3.9 Å x 3.9 Å surface O_α atom grid, further reducing the ability of propene to adsorb effectively. Unlike the scheelite mixed-metal molybdates, MoO_3 does not have under-coordinated surface cations with which propene can interact favorably.

3.5.2 Hydrogen abstraction from propene

Figure 3.12 displays the relevant energy parameters for the most active surface oxygen on the four different metal oxide surfaces studied. The energy of the final state, allyl radical adsorbed over a surface with one hydrogen atom added to a Mo=O group, relative to the zero energy reference state of bare oxidized surface with propene in the gas phase is a measure of the ability of the catalyst to activate propene. As discussed in the Introduction, the energy of this final state is a lower bound on the apparent activation energy. For $Bi_2Mo_3O_{12}$, the only material for which we have calculated the full reaction barrier, the transition state is only 7.6 kcal/mol above the final state.[17,38] Given what we know from the Born-Haber cycle decomposition of the transition state energy,[22] we expect that the combination of HAE and propene adsorption captures the major components of the transition state, and therefore we expect that the other

materials have actual transition state energies that are similarly close in energy to the final state. However, regardless of the difference between the two, the transition state cannot be lower in energy than the final state.
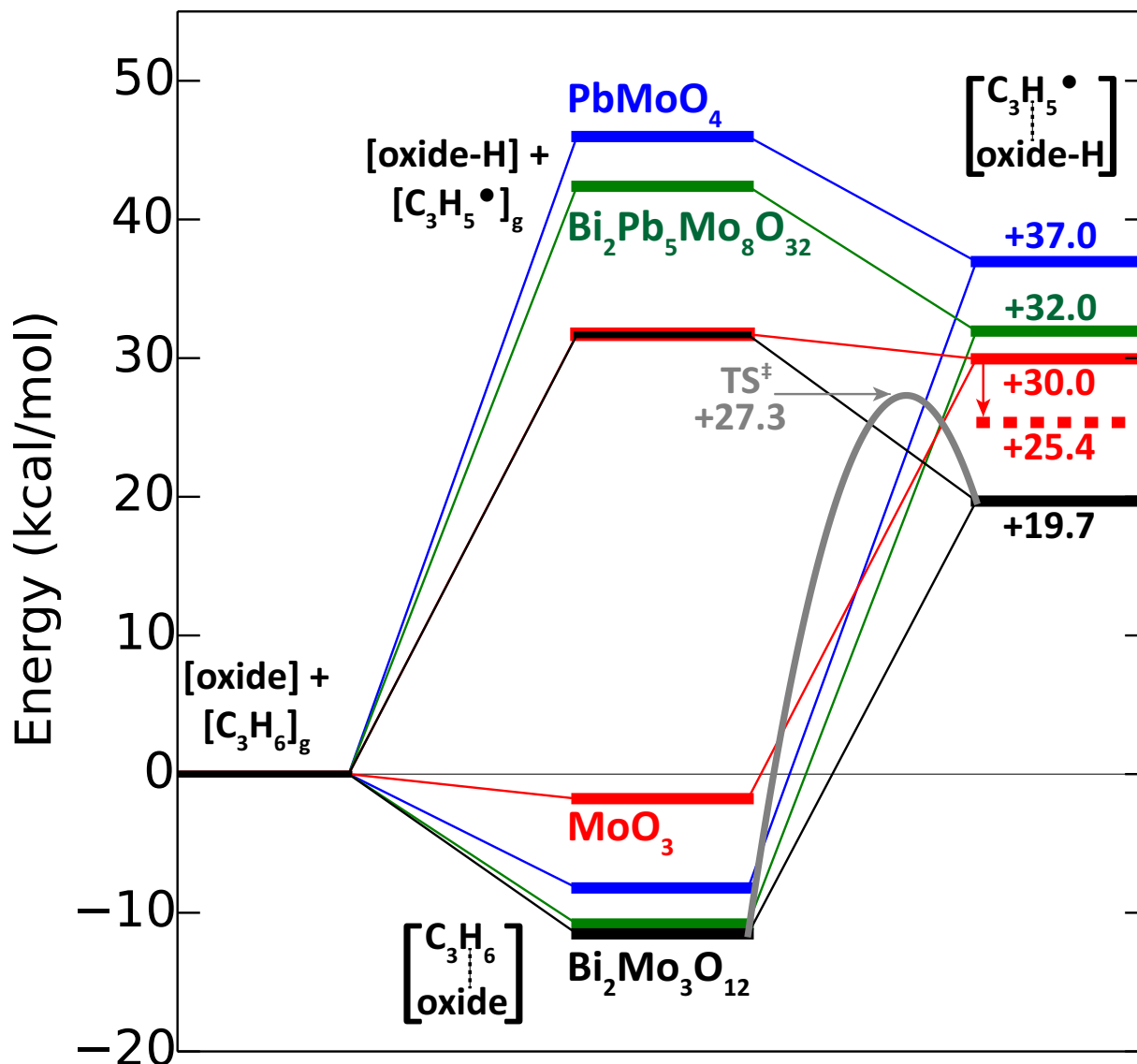

Fig. 3.12 Relevant energy values for first hydrogen abstraction from propene. Normalization point for all materials is a bare oxidized surface plus propene in the gas phase. Full reaction barrier through the transition state shown only for $Bi_2Mo_3O_{12}$. The two final state values for MoO_3 are shown, one for $\Delta E_{ads,C3H5}^{=} = \Delta E_{ads,C3H6}$ (solid line) and one for calculated $\Delta E_{ads,C3H5}^{=}$ (dashed line). The appropriate comparison between materials is the energy of the final state indicated with a solid line.

Material & Surface Oxygen	$\Delta E_{ads,C3H6}$ on oxidized surface [kcal/mol]	$\Delta E_{ads,C3H5}^=$ on 1-H surface [kcal/mol]
$Bi_2Mo_3O_{12}$ [O_β]	-11.5	-12.0
$PbMoO_4$ [O_β]	-8.2	-9.0
$Bi_2Pb_5Mo_8O_{32}$ [O_β']	-10.3	-10.4
MoO_3 [O_α]	-1.8	-6.4

Table 3.5. Propene adsorption energy on an oxidized surface ($\Delta E_{ads,C3H6}$) and allyl adsorption energy on a one hydrogen added surface ($\Delta E_{ads,C3H5}^=$) for each of the four tested materials.

Figure 3.12 demonstrates that $Bi_2Mo_3O_{12}$ is a good catalyst for propene activation because it has a low energy for propene adsorption near the most active oxygen, which itself has a low HAE. Together, these effects combine to give a final state energy of 19.7 kcal/mol, the lowest of any material examined in this study. Additionally, as is apparent from Figure 3.2, propene adsorbed to a surface bismuth cation is within reach of three O_β atoms, and this configuration enhances the probability of hydrogen abstraction. Moreover, the character of the Bi orbitals allows for favorable dative interaction between propene and bismuth to be partially maintained in the transition state, which should help stabilize the allyl radical as it forms.[17]

The next lowest final state energy is for MoO_3. Most studies have found MoO_3 to be inactive;[36,37] however, there have been some reports of measurable propene conversion to acrolein at higher temperatures.[58] One study has investigated the role of the exposed surface plane for epitaxial MoO_3 deposited on graphene, and observed that the higher the concentration of the lowest energy (010) plane, the lower the production of acrolein.[58] Our results are consistent with these conflicting reports. For a fully oxidized surface exposing only the (010) surface plane, we would not expect significant propene oxidation because the final state energy for hydrogen abstraction by O_α is too high (see Figure 3.12 and additional details below). However, the higher energy surface planes will expose a few of the highly active O_β atoms that are inaccessible on the (010) surface, and additionally, if the catalyst is not fully oxidized under working conditions, propene may be able to adsorb favorably at any under-coordinated surface molybdenum sites and then undergo reaction. Both of these influences could lead to some measurable propene oxidation activity. However, under O_2-rich conditions, the surface of MoO_3 is expected to remain oxidized, with few to no propene adsorption sites and, therefore, to be lower in activity relative to $Bi_2Mo_3O_{12}$.

While the O_β sites on MoO_3 remain inaccessible to gas phase propene, the O_α sites have a favorable HAE equal to that of O_β sites on $Bi_2Mo_3O_{12}$. The 9 kcal/mol difference in propene adsorption energy between these two materials with equal HAE should translate to a MoO_3 final state with an energy 9 kcal/mol above that of $Bi_2Mo_3O_{12}$. However, as is clear from Table 3.5, the adsorption of allyl radical is 5 kcal/mol lower in energy than the adsorption of propene. The

stronger allyl adsorption on MoO_3 is due to coordination with a surface O_α, resulting in stabilization of the polarizable allyl radical by oxygen. This phenomenon is not observed for the other materials, which have allyl adsorption energies approximately equal to that of propene and for which insertion of the allyl radical into a Mo=O bond occurs as a separate step.[17,21] Since the allyl is formed in the transition state, this additional allyl stabilization only occurs after the transition state, making it irrelevant to the reaction barrier for hydrogen abstraction from propene. Therefore, the final state for MoO_3 that is more comparable to that for the other oxides is for an allyl radical adsorption energy approximately equal to that of propene. Making this adjustment leads to final-state energy of +30.0 kcal/mol for MoO_3 (the solid line in Fig. 3.12). Therefore, MoO_3 is expected to be considerably less active than $Bi_2Mo_3O_{12}$, since the lower bound on its transition-state energy is 3 kcal/mol higher than the calculated transition-state energy for $Bi_2Mo_3O_{12}$, and the actual transition state energy will be even higher. Thus, MoO_3 is a poor catalyst for the activation of propene not because it has inactive oxygen atoms, but because it does not adsorb propene so that it can interact with the active oxygen atoms.

$PbMoO_4$ is clearly inactive for propene activation because of both unfavorable hydrogen addition sites and moderately weak propene adsorption sites. The calculated final state energy of +37.5 kcal/mol (Fig. 3.12) is consistent with experimental reports that this material does not catalyze propene oxidation.[29]

Finally, the mixed bismuth lead molybdate shows a final state energy between those for pure lead molybdate and pure bismuth molybdate. The experimental results show an activity closer to $Bi_2Mo_3O_{12}$ than we predict from our DFT calculations;[27] however, it is not known what the bismuth to lead ratio is on the surface of a mixed molybdate or where the vacancies occur and if they are distributed randomly or in an ordered manner; therefore, we do not know how close our model is to the observed structure. Nevertheless, this material allows us to explore the effect of introducing vacancies, and we do observe the correct trend moving from $PbMoO_4$ to $Bi_2Pb_5Mo_8O_{32}$.

Our analysis shows that $Bi_2Pb_5Mo_8O_{32}$ has both stronger propene adsorption sites and more negative values of the HAE than $PbMoO_4$. As mentioned above, these outcomes are both consequences of the increased flexibility of the lattice that comes from introducing vacancies and Bi^{3+} cations, which are smaller than Pb^{2+} cations. The ability of the oxide to distort in order to achieve a more desirable coordination around molybdenum, as well as the distortion already present at the oxidized surface, explains why previous studies have associated high activity for propene activation to the presence of vacancies.[21,27,30] (see Introduction). The 3+ lanthanide scheelite molybdates, which have a vacancy ordering that is different from that in $Bi_2Mo_3O_{12}$, do not show activity for propene oxidation or ammoxidation. The reason is that the lanthanides lack the stereochemically active lone pair that drives asymmetric coordination environments around bismuth and thereby enforce 5-coordinate geometries at molybdenum. Thus, despite containing cation vacancies, the lanthanide molybdates exhibit energetically preferred, but less catalytically active, 4-coordiante geometries at molybdenum. The results of the present study show why both bismuth and vacancies are required for an active molybdate-based catalyst, since together they

induce higher molybdenum coordination in the oxidized state and provide the conformational flexibility required to further increase molybdenum coordination when a hydrogen atom is transferred to a Mo=O bond in the rate-limiting step of propene oxidation or ammoxidation.

4. Conclusions

Four different metal oxides containing molybdenum ($Bi_2Mo_3O_{12}$, $PbMoO_4$, $Bi_2Pb_5Mo_8O_{32}$, and MoO_3) have been analyzed with the objective of explaining their relative catalytic activity for propene oxidation and ammoxidation. This analysis is predicated on the assumption that the key step governing the ability of a catalyst to activate propene is the abstraction of a hydrogen atom from the methyl group of adsorbed propene to form a Mo-OH group and a physisorbed allyl radical. We find that a low reaction barrier for hydrogen atom abstraction requires a favorable site for propene adsorption that is proximate to a surface oxygen atom that has a low hydrogen adsorption energy (HAE).

Favorable propene adsorption occurs on under-coordinated surface metal cations via dative interaction between the π bond of propene and the metal cation. This interaction can be offset by repulsive interactions between propene and surface oxygen anions. Of the oxides examined, the strongest adsorption of propene occurs on Bi^{3+} present at the surface of $Bi_2Mo_3O_{12}$, because these cations are situated close to the surface and the nearest neighboring oxygen anions are far enough away to have only a limited repulsive effect. Pb^{2+} in $PbMoO_4$ is not as favorable for propene adsorption as Bi^{3+}, since it is located slightly deeper in the surface and, hence, repulsive interactions with the neighboring oxygen anions play a larger role in reducing the adsorption energy. The least favorable energy of adsorption occurs for MoO_3 because this oxide has no under-coordinated cations at its surface, only protruding oxygen anions.

The second requirement for good catalyst activity is a surface oxygen atom with a high HAE. From observations of the geometric changes in the metal oxide surface upon hydrogen addition and additional detailed molecular orbital investigation of the influence of individual effects, we conclude that the most important structural property is a highly-coordinated molybdenum atom at the oxide surface. Molecular orbital analysis reveals that the presence of an oxygen atom *trans* to the oxo group to which a hydrogen is added increases the energy of the highest occupied molecular orbital, thereby reducing the energy required to rehybridize the molybdenum oxygen double bond from the singlet state to the triplet state. The energy for rehybridization is the energy component that has the strongest influence on the overall HAE, consistent with our previous work demonstrating that band gap correlates well with apparent activation energy.[22] The present investigation has revealed that greater than 4-coordinate molybdenum atoms are energetically disfavored, but are needed to achieve a low HAE.

In the absence of surface molybdenum atoms that are coordinated with more than four oxygen atoms, surface conformational flexibility can allow for a partial increase in oxygen coordination upon hydrogen addition. Evidence for this was observed in the case of $Bi_2Pb_5Mo_8O_{32}$, for which the surface has 4-coordinate molybdenum atoms that have a geometry

very similar to that in $PbMoO_4$. However, the HAE for the lowest energy oxygen in the former structure is 4 kcal/mol more negative than that for the later structure. The introduction of asymmetric Bi^{3+} in the surface layer of the parent structure and vacancies one layer below the surface give the mixed material the conformational flexibility to achieve favorable, higher molybdenum coordination after hydrogen addition. However, the molybdenum in $Bi_2Pb_5Mo_8O_{32}$ is not able to move as close to an additional oxygen atom in the final state as in the case of $Bi_2Mo_3O_{12}$. $Bi_2Pb_5Mo_8O_{32}$ also lacks the initial state destabilization that contributes to the more favorable value of HAE for $Bi_2Mo_3O_{12}$.

Finally, we have explored the ability of cations in metal molybdates to perturb the electronic properties of nearby Mo=O groups, a process that we had previously suggested was crucial for high activity.[19] Substitution of a surface Bi^{3+} in $Bi_2Mo_3O_{12}$ with $Pb^{2+}+H^+$, La^{3+} or Sb^{3+} demonstrated that other cations are able to have a similar electronic perturation effect as bismuth on the neighboring molybdenyl oxo. However, the presence of one of these cations only makes the HAE more negative by 3 kcal/mol relative to substitution of a surface Bi^{3+} in $Bi_2Mo_3O_{12}$ with B^{3+}, which does not have any interaction with the oxo. Therefore, the more critical role of bismuth is to force molybdenum into the 5-coordinate geometry that is significantly more active for abstracting a hydrogen from propene.

References

Introduction

[1] R.K. Grasselli, Top. Catal. 21 (2002) 79-88.

[2] D. Arntz, A. Fischer, M. Höpp, S. Jacobi, J. Sauer, T. Ohara, T. Sato, N. Shimizu, H. Schwind, In Ullmann's Encyclopedia of Industrial Chemistry Wiley-VCH, Weinheim, Germany, 2012.

[3] J.F. Brazdil, Acrylonitrile, Ullmann's Encyclopedia of Industrial Chemistry, Wiley-VCH, Weinheim, 2007.

[4] J.D. Idol, U.S. Patent 2,904,580 (1959).

[5] T.P. Snyder, C.G. Hill, Cat. Rev. 31 (1989) 43-95.

[6] J.F. Brazdil, Catal. Sci. Technol. 5 (2015) 3452-3458.

[7] R.K. Grasselli, J. Chem Ed. (1986) 63, 216.

[8] C.R. Adams, T.J. Jennings, J. Catal. (1963) 2, 63-68.

[9] J.L. Callahan, R.K. Grasselli, E.C. Milberger, H.A. Strecker, Ind. Eng. Chem. Prod. Res. Dev. (1970) 9, 134-142.

Chapter 1

[0] R.B. Licht, D. A.T. Vogt, Bell, J. Catal. (2016) 339, 228-241.

[1] J.D. Idol, U.S. Patent 2,904,580 (1959).

[2] J.F. Brazdil, Acrylonitrile, Ullmann's Encyclopedia of Industrial Chemistry, Wiley-VCH, Weinheim, 2007.

[3] R.K. Grasselli, Top. Catal. 21 (2002) 79-88.

[4] M. Egashira, K. Matsuo, S. Kagawa, T. Seiyama. J. Catal. 58 (1979) 409-418.

[5] W. Ueda, K. Asakawa, C.-L. Chen, Y. Moro-Oka, T. Ikawa, J. Catal. 101 (1986) 360-368.

[6] A.B. Getsoian, Z. Zhai, A.T. Bell, J. Am. Chem. Soc. 136 (2014) 13684-13697.

[7] J.F. Brazdil, L.C. Glaeser, R.K. Grasselli, J. Phys. Chem. 87 (1983) 5485-5491.

[8] B. Grzybowska, J. Haber, J. Janas, J. Catal. 49 (1977) 150-163.

[9] J.D. Burrington, R.K. Grasselli, J. Catal. 59 (1979) 79-99.

[10] H.E. Swift, J.E. Bozik, J.A. Ondrey J. Catal. 21 (1971) 212-224.

[11] C.R. Adams, T.J. Jennings, J. Catal. 3 (1964) 549-558.

[12] L.D. Krenze, G.W. Keulks, J. Catal. 61 (1980) 316-325.

[13] J. Haber, B. Grzybowska, J. Catal. 28 (1973) 489-505.

[14] J.D. Burrington, C.T. Kartisek, R.K. Grasselli, J. Catal. 81 (1983) 489-498.

[15] T.A. Hanna, Coord. Chem. Rev. 248 (2004) 429-440.

[16] A.B. Getsoian, V. Shapovalov, A.T. Bell, J. Phys. Chem. C 117 (2013) 7123-7137.

[17] C.C. McCain, G. Gough, G.W. Godin, Nature 198 (1963) 989-990.

[18] W.M.H Sachtler, N.K. DeBoer, Proceedings 3rd International Congress on Catalysis, 1 (1965) 252.

[19] J.D. Burrington, C.T. Kartisek, R.K. Grasselli, J. Org. Chem. 46 (1981) 1877-1882.

[20] P. Mars, D.W. van Krevelen, Chem. Eng. Sci. 3 (1954) 41-59.

[21] G.W. Keulks, J. Catal. 19 (1970) 232-235.

[22] T.P. Snyder, C.G. Hill, Cat. Rev. 31 (1989) 43-95.

[23] J.M. Peacock, A.J. Parker, P.G. Ashmore, J.A. Hockney, J. Catal. 15 (1969) 398-406.

[24] C. R. Adams, H.H. Voge, C.Z. Morgan, W.E. Armstrong, J. Catal. 3 (1964) 379-386.

[25] G.W. Keulks, L.D. Krenze, Proceedings 6th International Congress on Catalysis p. 806 (1976).

[26] Z. Zhai, A.B. Getsoian, A.T. Bell, J. Catal. 308 (2013) 25-36.

[27] J.L. Callahan, R.K. Grasselli, E.C. Milberger, H.A. Strecker, Ing. Eng. Chem. Prod. Res. Dev. 2 (1970) 134-142.

[28] R.D. Wragg, P.G. Ashmore, J.A. Hockey, J. Catal. 31 (1973) 293-303.

[29] I.K. Kolchin, S.S. Bobkov, L. Ya. Margolia, Neftekhimiya 4 (1964) 301-307.

[30] C.R. Adams, T.J. Jennings, J. Catal. 2 (1963) 63-68.

[31] K. Aykan, J. Catal. 12 (1968) 281-290.

[32] J. D. Burrington, C.T. Kartisek, R.K. Grasselli, J. Catal. 66 (1980) 347-367.

[33] J.D. Burrington, C.T. Kartisek, R.K. Grasselli, J. Catal. 87 (1984) 363-380.

[34] Y.H. Jang, W.A. Goddard III, J. Phys. Chem. B 106 (2002) 5997-6013.

[35] Y. Du, A.L. Rheingold, E.A. Maatta, J. Am. Chem. Soc. 114 (1992) 345-346.

[36] H.H. Fox, K.B. Yap, J. Robbins, S. Cai, R.R. Schrock, Inorg. Chem. 31 (1992) 2287-2289.

[37] G. Hogarth, I. Richards, Transition Met. Chem. 35 (2010) 111-115.

[38] S. Pudar, J. Oxgaard, K. Chenoweth, A.C.T. van Duin, W.A. Goddard III, J. Phys. Chem. C 111 (2007) 16405-16415.

[39] S. Pudar, J. Oxgaard, W.A. Goddard III, J. Phys. Chem. C 114 (2010) 15678-15694.

[40] I. Matsuura, J. Catal. 33 (1974) 420-433.

[41] M.T. Le, W.J.M. Van Well, I. Van Driessche, S. Hoste, Appl. Catal. A, Gen. 267 (2004) 227-243.

[42] F. Theobald, A. Laarif, Mat. Res. Bull. 20 (1985) 653-665.

[43] S. Grimme, Chem. Eur. J. 18 (2012) 9955-9964.

[44] B.A. De Moor, M.-F. Reyniers, G. B. Marin, Phys. Chem. Chem. Phys. 11 (2009) 2939-2958.

[45] A.B. Getsoian, A.T. Bell, J. Phys. Chem. C 117 (2013) 25562-25578.

[46] J. D. Burrington, C.T. Kartisek, R.K. Grasselli, J. Catal. 75 (1982) 225-232.

[47] J. D. Burrington, C.T. Kartisek, R.K. Grasselli, J. Catal. 63 (1980) 235-254.

[48] L. Lietti, G. Ramis, G. Busca, F. Bregani, P. Forzatti, Catal. Today 61 (2000) 187-195.

Chapter 2

[0] R.B. Licht, A.T. Bell, ACS Catalysis, *submitted Aug. 2016.*

[1] R.K. Grasselli, Top. Catal. (2002) 21, 79-88.

[2] D. Arntz, A. Fischer, M. Höpp, S. Jacobi, J. Sauer, T. Ohara, T. Sato, N. Shimizu, H. Schwind, In Ullmann's Encyclopedia of Industrial Chemistry Wiley-VCH, Weinheim, Germany, 2012.

[3] J.F. Brazdil, In Ullmann's Encyclopedia of Industrial Chemistry Wiley-VCH, Weinheim, Germany, 2012.

[4] R.B. Licht, D. A.T. Vogt, Bell, J. Catal. (2016) 339, 228-241.

[5] R.D. Wragg, P.G. Ashmore, Hockey, J.A. J. Catal. (1973) 31, 293-303.

[6] I.K. Kolchin, S.S. Bobkov, Margolia, L.Y. Neftekhimiya (1964) 4, 301-307.

[7] Z. Zhai, A.B. Getsoian, A.T. Bell, J. Catal. (2013) 308, 25-36.

[8] J.L. Callahan, R.K. Grasselli, E.C. Milberger, H.A. Strecker, Ind. Eng. Chem. Prod. Res. Dev. (1970) 9, 134-142.

[9] C.R. Adams, T.J. Jennings, J. Catal. (1963) 2, 63-68.

[10] C.R. Adams, T.J. Jennings, J. Catal. (1964) 3, 549-558.

[11] L.D. Krenze, G.W. Keulks, J. Catal. (1980) 61, 316-325.

[12] C.C. McCain, G. Gough, G.W. Godin, Nature (1963) 198, 989-990.

[13] J.D. Burrington, C.T. Kartisek, R.K. Grasselli, J. Org. Chem. (1981) 46, 1877-1882.

[14] W.M.H. Sachtler, N.K. DeBoer, In Proceedings 3rd International Congress on Catalysis (1965) Vol. 1, p 252.

[15] Y. Zhao, D.G. Truhlar, J. Chem. Phys. (2006) 125 194101-194118.

[16] A.B. Getsoian, A.T. Bell, J. Phys. Chem. C, (2013) 117 25562-25578.

[17] A.B. Getsoian, V Shapovalov, Bell, A.T. J. Phys. Chem. C (2013) 117 7123-7137.

[18] J. Haber, D. J. Grzybowska, Catal. (1973) 28, 489-505.

[19] T.A. Hanna, Coord. Chem. Rev. (2004) 248, 429-440.

[20] J.D. Burrington, C.T. Kartisek, R.K. Grasselli, J. Catal. (1983) 81, 489-498.

[21] G.W. Keulks, J. Catal. (1970) 19, 232-235.

[22] T.P. Snyder, C.G. Hill, Catal. Rev. (1989) 31, 43-95.

[23] S. Pudar, J. Oxgaard, K. Chenoweth, A.C.T. van Duin, W.A. Goddard III, J. Phys. Chem. C (2007) 111, 16405-16415.

[24] J.D. Burrington, C.T. Kartisek, R.K. J. Grasselli, Catal. (1984) 87, 363-380.

[25] S. Pudar, J. Oxgaard, W.A. Goddard III, J. Phys. Chem. C (2010) 114, 15678-15694.

[26] Y.H. Jang, W.A. Goddard III, J. Phys. Chem. B (2002) 106, 5997-6013.

[27] G Kresse, J. Hafner, Phys. Rev. B (1993) 47, 558-561.

[28] B. Hammer, L.B. Hansen, J.K. Nørskov, Phys. Rev. B (1999) 59, 7413-7421.

[29] G. Kresse, J. Furthmüller, Phys. Rev. B (1996) 54, 11169-11186.

[30] P.E. Blochl, Phys. Rev. B (1994) 50, 17953-17979.

[31] G. Kresse, D. Joubert, Phys. Rev. B (1999) 59, 1758-1775.

[32] F. Theobald, A. Laarif, A.W. Hewat, Mat. Res. Bull. (1985) 20, 653-665.

[33] V.G. Tyuterev, N. Vast, Comput. Mater. Sci. (2006) 38, 350-353.

[34] S.E. Wheeler, K.N. J. Houk, Chem. Theory Comput. (2010) 6, 395-404.

[35] G. Henkelman, H. J. Jonsson, Chem. Phys. (2000) 113, 9978-9985.

[36] M.D. Carducci, C. Brown, E.L. Solomon, J.H. Enemark, J. Am. Chem. Soc. (1994) 116, 11856-11868.

[37] G. Henkelman, H. Jonsson, J. Chem. Phys. (2000) 113, 9901-9904.

[38] Y. Shao, et al. Mol. Phys. (2015) 113, 184-215.

[39] L.D. Krenzke, G.W. Keulks, J. Catal. (1980) 61, 316-325.

[40] R.D. Wragg, P.G. Ashmore, J.A. Hockey, J. Catal. (1973) 28, 337.

[41] G.W. Keulks, L.D. Krenzke, T.M. Notermann, Adv. Catal. (1978) 27, 183-225.

[42] J.F. Brazdil, D.D. Suresh, R.K. Grasselli, J. Catal. (1980) 66, 347-367.

[43] G.W. Keulks, J. Catal. 1970, 19, 232-235.

[44] A.W. Sleight, W.J. Linn, Annals N.Y. Acad. Sci (1976) 22-44.

[45] Z. Zhai, Wang, X. R.B. Licht, A.T. Bell, J. Catal. (2015) 325, 87-100.

[46] L. Stradella, G. Z. Vogliolo, Phys. Chem. (1973) 137, 99-110.

Chapter 3

[0] R.B. Licht, A. Getsoian, A.T. Bell, J. Phys. Chem. C, *submitted Sept. 2016.*

[1] Brazdil, J.F. In *Ullmann's Encyclopedia of Industrial Chemistry*; Wiley-VCH: Weinheim, Germany, 2012.

[2] R.K. Grasselli, Top. Catal. 21 (2002) 79-88.

[3] J.F. Brazdil, Catal. Sci. Technol. 5 (2015) 3452-3458.

[4] R.K. Grasselli, J.D. Burrington, J.F. Brazdil, Farad. Disc. 72 (1981) 203-223

[5] I. Matsuura, R. Schut, K. Hirakawa, J. Catal. 63 (1980) 152-166.

[6] R.B. Licht, D. Vogt, A.T. Bell, J. Catal. 339 (2016) 228-241.

[7] J.L. Callahan, R.K. Grasselli, E.C. Milberger, H.A. Strecker, Ind. Eng. Chem. Prod. Res. Dev. 9 (1970) 134-142.

[8] R.D. Wragg, P.G. Ashmore, J.A. Hockey, J. Catal. 31 (1973) 293-303.

[9] Kolchin, I.K.; Bobkov, S.S.; Margolia, L.Y. Neftekhimiya 4 (1964) 301-307.

[10] C.R. Adams, T.J. Jennings, J. Catal. 2 (1963) 63-68.

[11] C.R. Adams, H.H. Voge, C.Z. Morgan, W.E. Armstrong, J. Catal. 3 (1964) 379-386.

[12] C.C. McCain, G. Gough, G.W. Godin, Nature 198 (1963) 989-990.

[13] L.D. Krenze, G.W. Keulks, J. Catal. 61 (1980) 316-325.

[14] Burrington, J.D.; Kartisek, C.T.; Grasselli, R.K. J. Org. Chem. 46 (1981) 1877-1882.

[15] J.M. Peacock, A.J. Parker, P.G. Ashmore, J.A. Hockney, J. Catal. 15 (1969) 398-406.

[16] G.W. Keulks, J. Catal. 19 (1970) 232-235.

[17] R.B. Licht, A.T. Bell, *Submitted to ACS Catalysis.*

[18] Z. Zhai, A. Getsoian, A.T. Bell, J. Catal. 308 (2013) 25-36.

[19] A. Getsoian, V. Shapovalov, A.T. Bell, J. Phys. Chem. C 117 (2013) 7123-7137.

[20] Pudar, S.; Oxgaard, J.; Goddard III, W.A. J. Phys. Chem. C 114 (2010)15678-15694.

[21] J.D. Burrington, C.T. Kartisek, R.K. Grasselli, J. Catal. 81 (1983) 489-498.

[22] A. Getsoian, Z. Zhai, A.T. Bell, J. Am. Chem. Soc. 136 (2014) 13684-13697.

[23] T.P. Snyder, C.G. Hill, Catal. Rev. 31 (1989) 43-95.

[24] T.A. Hanna, Coord. Chem. Rev. 248 (2004) 429-440.

[25] J.F. Brazdil, L.C. Glaeser, R.K. Grasselli, J. Catal. 81 (1983) 142-146.

[26] F. Theobald, A. Laarif, A.W. Hewat, Mat. Res. Bull. 20 (1985) 653-665.

[27] A.W. Sleight, W.J. Linn, Annals N.Y. Acad. Sci (1976) 22-44.

[28] J. Leciejewicz, Z. Kristallogr. 121 (1965) 158.

[29] K. Aykan, A.W. Sleight, D.B. Rogers, J. Catal. 29 (1973) 185-187

[30] K. Aykan, D. Halvorson, A.W. Sleight, D.B. Rogers, J. Catal. 35 (1974) 401-406.

[31] K. Boulahya, M. Parras, J.M. Gonzalez Calbet, Eur. J. Inorg. Chem. 5 (2005) 967-970.

[32] W. Jeitschko, Acta Cryst. B 29 (1973) 2074-2081.

[33] W. Ueda, K. Asakawa, C.L. Chen, Y. Moro-Oka, T. Ikawa, J. Catal. 101 (1986) 360-368.

[34] A.W. Sleight, W. Jeitchko, Mater. Res. Bull. 9 (1974) 951-954.

[35] H.E. Swift, J.E. Bozik, J.A. Ondrey, J. Catal. 21 (1971) 212-214.

[36] B. Grzybowska, J. Haber, J. Janas, J. Catal. 49 (1977) 150-163.

[37] J.D. Burrington, R.K. Grasselli, J. Catal. 59 (1979) 79-99.

[38] A. Getsoian, A.T. Bell, J. Phys. Chem. C 117 (2013) 25562-25578.

[39] B. Hammer, L.B. Hansen, J.K. Nørskov, Phys. Rev. B 59 (1999) 7413-7421.

[40] Y. Zhao, D.G. Truhlar, J. Chem. Phys. 125 (2006) 194101.

[41] G. Kresse, J. Furthmüller, Phys. Rev. B 54 (1996) 11169.

[42] P.E. Blochl, Phys. Rev. B 50 (1994) 17953.

[43] L. Kihlborg, Arkiv. Kemi 21 (1963) 357.

[44] V.G. Tyuterev, N. Vast, Comput. Mater. Sci. 38 (2006) 350-353.

[45] H.C. Zeng, L.C. Lin, J. Mater. Res., 13 (1998) 1426-1429.

[46] S.E. Wheeler, K.N. Houk, J. Chem. Theory Comput. 6 (2010) 395-404.

[47] A.W. Sleight, K. Aykan, D.B. Rogers, J. Solid State Chem., 13 (1975) 231-236.

[48] Y. Shao et al. Mol. Phys. 113 (2015) 184-215.

[49] D. Andrae, U. Haeussermann, M. Dolg, H. Stoll, H. Preuss, Theor. Chim. Acta 77 (1990) 123-141.

[50] K.L. Schuchardt, B.T. Didier, T. Elsethagen, L. Sun, V. Gurumoorthi, J. Chase, J. Li, T.L. Windus, J. Chem. Inf. Model 47 (2007) 1045-1052.

[51] J.-D. Chai, M. Head-Gordon, J. Chem. Phys. 128 (2010) 084106.

[52] G. Schaftenaar, J.H. Noordik, J. Comput.-Aided Mol. Design 14 (2000) 123-134.

[53] K. Momma, F. Izumi, J. Appl. Crystallogr. 44 (2011) 1272-1276.

[54] K. Kwapien, M. Sierka, J. Dobler, J. Sauer, Chem. Cat. Chem. 2 (2010) 819-826.

[55] M. Y. Sinev, Z.T. Fattakhova, V.I. Lomonosov, Y.A. Gordienko, J. Nat. Gas Chem. 18 (2009) 273-287.

[56] R.A. Wheeler, P.N.V. Pavan Kumar, J. Am. Chem. Soc. 114 (1992) 4776-4784.

[57] A. Walsh, W.G. Watson, D.G. Payne, R.G. Egdell, J. Guo, P.-A. Glans, T. Learmonth,

K.E. Smith, Phys. Rev. B 73 (2006) 235104.

[58] J.-C. Volta, M. Forissier, F. Theobald, T.P. Pham, Royal Soc. Chem. (1981) 225-233.

Appendix A

[1] I. Matsuura, J. Catal. 33 (1974) 420-433.

[2] S. Grimme, Chem. Eur. J. 18 (2012) 9955-9964.

[3] F. Theobald, A. Laarif, Mat. Res. Bull. 20 (1985) 653-665.

[4] M.T. Le, W.J.M. Van Well, I. Van Driessche, S. Hoste, Appl. Catal. A, Gen. 267 (2004) 227-243.

Appendix A

1. GC Calibration

The response of the GC to gaseous products was calibrated with pure components fed through the MFCs and diluted in helium to varying degrees. Most liquid products were calibrated by bubbling helium through the pure liquid submerged in a recirculating chiller at temperatures between 260 K and 283 K and then diluting the resultant vapor with helium before feeding it into the GC. The vapor pressure of the liquid at the bath temperature was calculated using the Antoine Equation parameters found in the NIST database.[1] Mole fractions of the liquid products were varied by changing the bath temperature and the ratio of flow rates of helium through the bubbler and diluent helium.

HCN was calibrated by bubbling reactor effluent at standard catalyst conditions into a caustic iodide solution and titrating the solution with 0.01M $AgNO_3$. One mole of Ag^+ reacts initially with 2 moles of CN^- to create a soluble product. Once all the CN^- is consumed, Ag^+ reacts with I^- forming insoluble AgI that turns the solution light brown and cloudy. The mole fraction of HCN in the effluent was calculated by dividing the number of moles of HCN dissolved in the caustic iodide (twice the number of moles of $AgNO_3$ added before the solution became cloudy) by the bubbling time and the total molar flow rate. This mole fraction was compared to the difference in GC FID peak area for HCN between pure reactor effluent and effluent after bubbling through the caustic iodide. Mole fractions of HCN were varied by changing the total flow rate through the catalyst bed and the bubbling time.

2. Active site model

A $(O=Mo=O)_2Bi_2O_{10}H_{10}$ active site model representative of part of the (010) surface of $Bi_2Mo_3O_{12}$ was used to estimate heats of ammonia adsorption at different sites. The model was built by individually optimizing a $Mo^{6+}(O)_2(OH)_2(OH_2)$ cluster and a $Bi^{3+}(OH)_3$ cluster, then combining two of each cluster by removing one H and ½ O from every cluster to create the bridging O bond. The clusters were aligned to have the distances and angles between the key Bi, Mo and O atoms found in the VASP optimized (010) surface of $Bi_2Mo_3O_{12}$ detailed by Getsoian *et al.*[2] Once built, the H atoms were fixed to constrain the model, and the remaining Bi, Mo and O atoms were allowed to relax to their optimal positions. Figure SI 1 shows a top-down view of both the cluster, optimized in Q-Chem with fixed H positions, and the relevant moiety on the (010) surface, previously optimized in VASP with fixed lower layers and relaxed surface layers.

Note the similar atomic configurations in both depictions, even after the constrained optimization of the model cluster.

Once the model was built and optimized, ammonia was brought in to see where it might adsorb. The only favorable interaction found was for ammonia over a Bi^{3+} ion, oriented such that the lone pair on ammonia donated electron density to the bismuth. We observed that the NH_3 can be moved substantially (anywhere in the ~ 2Å x 2Å square above Bi^{3+}) without affecting the binding energy significantly, likely because the orbitals on Bi are very large and diffuse. Therefore, we use the assumption of Marin *et al.* that loosely adsorbed molecules can rotate in 3-D and translate in 2-D in order to estimate the entropy loss upon adsorption and thus the free energy of adsorption.[3] The enthalpy and entropy corrections for this model were calculated using the Grimme Rigid Rotor Harmonic Oscillator method.[4]
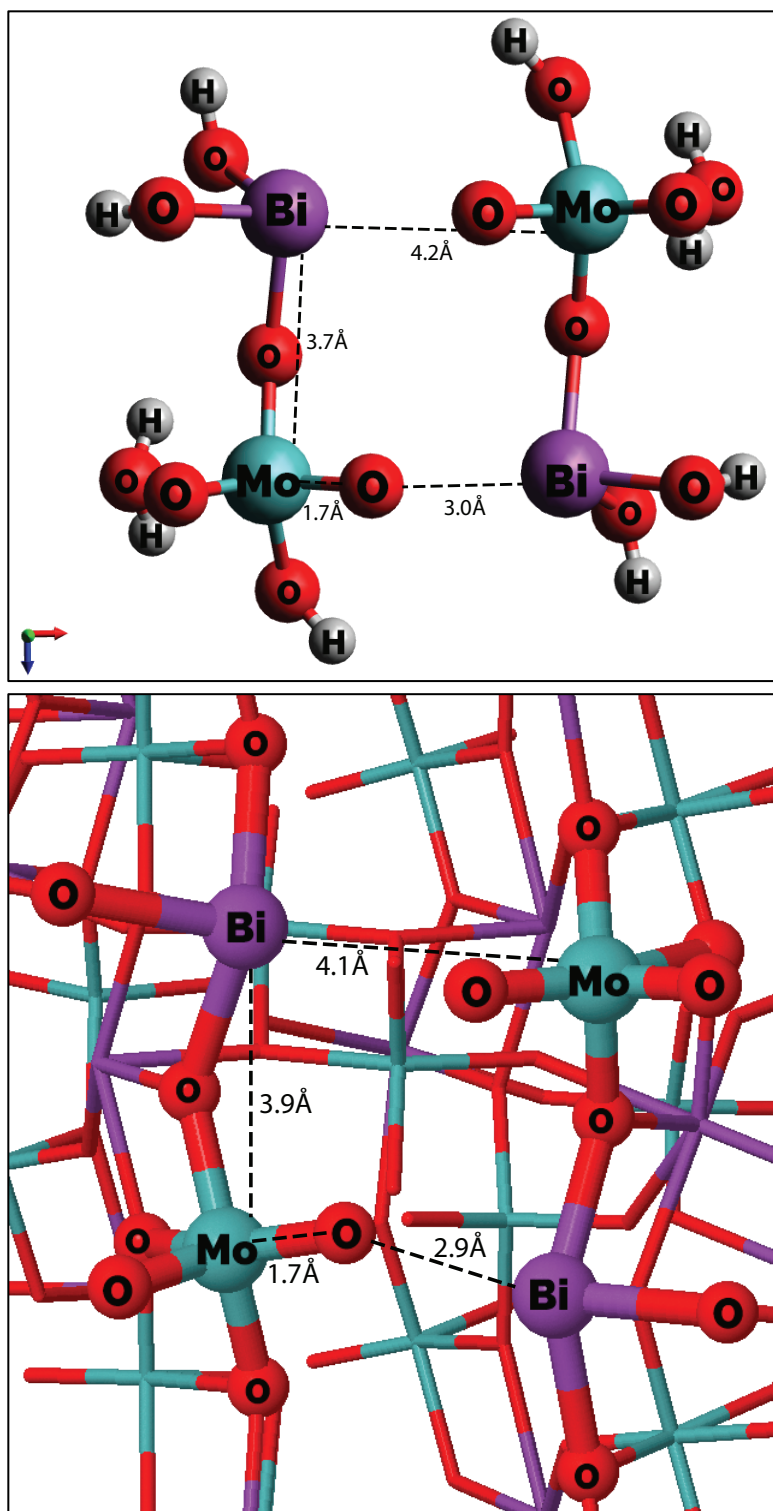
Fig. A.1 (top) Top-down view of the $Mo_2Bi_2O_{14}H_{10}$ cluster. (bottom) Top-down view of the optimized (010) surface of $Bi_2Mo_3O_{12}$ from Getsoian *et al.*[2]
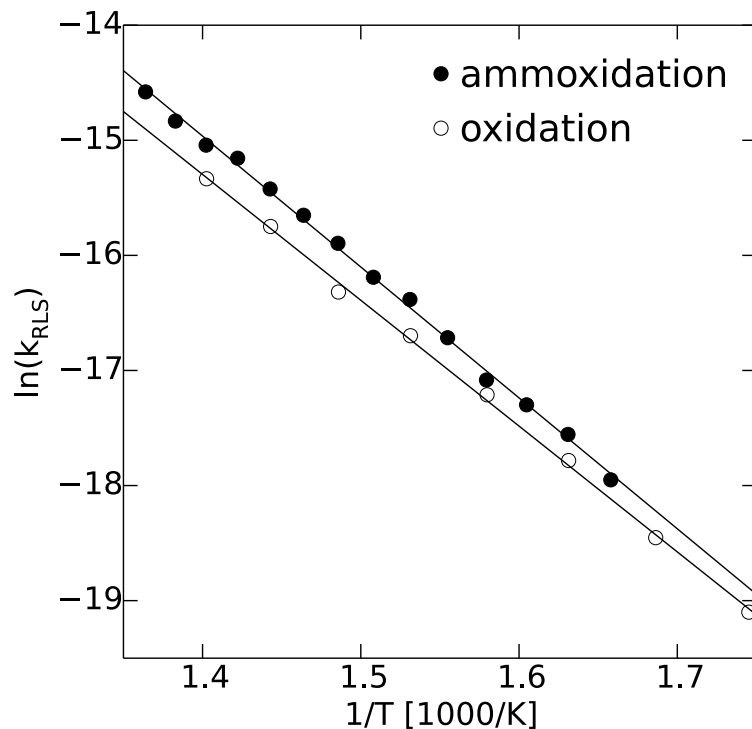
3. Arrhenius Plot

Fig. A.2 Arrhenius plot of k_{RLS} (Eqn. 3) for both propene ammoxidation (filled symbols) and propene oxidation (empty symbols). Ammoxidation $E_a = 22.4$ kcal/mol, temperature range 603 – 733 K, $P_{C3H6} = 7.6$ kPa, $P_{O2} = 15.1$ kPa, $P_{NH3} = 7.8$ kPa. Oxidation $E_a = 21.7$ kcal/mol, temperature range 573 – 713 K, $P_{C3H6} = 17$ kPa, $P_{O2} = 17$ kPa.

4. Description of the reaction network model

The inputs to the reactor model were the partial pressures of propene, ammonia, oxygen and water, the reactor temperature, the experimentally observed pressure upstream of the reactor, and the experimentally observed conversion. The temperature was used to calculate the values of all rate parameters (k_{RLS}, k_{ACON}, k_{N2}, k_{H2O}, α, β, γ, δ, and ε) from the Arrhenius parameters. The total pressure and partial pressures were used in the ideal gas law to calculate the total molar flow rate of each component (C_3H_6, NH_3, O_2, H_2O, and He) entering the reactor, always assuming the total volumetric flow rate was 100 mL/min at 298 K. We assumed a linear pressure drop through the catalyst bed from the experimentally measured pressure upstream of the reactor (generally ~120 kPa) to essentially atmospheric pressure downstream of the reactor (102 kPa). The experimentally observed conversion was used with the k_{RLS} to determine the catalyst surface area needed in the simulated reactor bed to attain said conversion (SA_{max}). In this way, the model always reflected what was observed experimentally, instead of containing artefacts due to experimental fluctuations that led to variable observed conversions.

106

The reactor model was built in Python using the scipy.integrate.odeint function to integrate the molar flow rate (F_x) of each component across the simulated catalyst surface area from 0 to SA_{max}. At each point, the partial pressure of each component x was calculated by dividing the molar flow rate of x over the total molar flow rate at that point. In this way, changes in total molar flow rate due to fragmentation reactions were accounted for. The differential molar rate expressions dF_x/dSA for all reactants and products (C_3H_6, NH_3, O_2, H_2O, ACN, ACO, NBP, OBP, He) were then calculated using the rate coefficients calculated from the Arrhenius parameters and partial pressures at that point, assuming a 1-D, well-mixed, simulated catalyst bed. The differential rate expressions were then fed into the odeint python function as indicated below. The C- and N- selectivities to each product group were calculated using the final molar flow rate of all compounds at the end of the simulated catalyst bed with surface area SA_{max}.

```
dFC3H6dSA = -kRLS*PC3H6

dFACOdSA = 0.94*kRLS*PC3H6(1/(1+alpha*PNH3)/(1+beta*PO2**0.5) +
alpha*PNH3*gamma*PH2O/(1+alpha*PNH3)/(1+gamma*PH2O+delta*PNH3+epsilon*
PO2**0.5)) - kACON*PACO*PNH3

dFACNdSA = 0.94*kRLS*PC3H6*alpha*PNH3/(1+alpha*PNH3)/(1+gamma*PH2O
+delta*PNH3+epsilon*PO2**0.5) + kACON*PACO*PNH3

dFNBPdSA = 0.94*kRLS*PC3H6*alpha*PNH3*(epsilon*PO2**0.5+delta*PNH3)/
(1+alpha*PNH3)/(1+gamma*PH2O+delta*PNH3+epsilon*PO2**0.5)

dFOBPdSA = 0.94*kRLS*PC3H6*beta*PO2**0.5/(1+alpha*PNH3)/
(1+beta*PO2**0.5) + 0.06*kRLS*PC3H6

dFN2dSA = kN2*PNH3/(1+kH2O*PH2O)

dFNH3dSA = -dFACNdSA - 7/3*dFNBPdSA - 2*dFN2dSA

dFO2dSA = -1.5*dFACNdSA -dFACOdSA - 7/3*dFNBPdSA - 10/3*dFOBPdSA -
3/2*dFN2dSA

dFH2OdSA = 3*dFACNdSA + dFACOdSA + 14/3*dFNBPdSA + 7/3*dFOBPdSA +
3*dFN2dSA

dFHedSA = 0
```
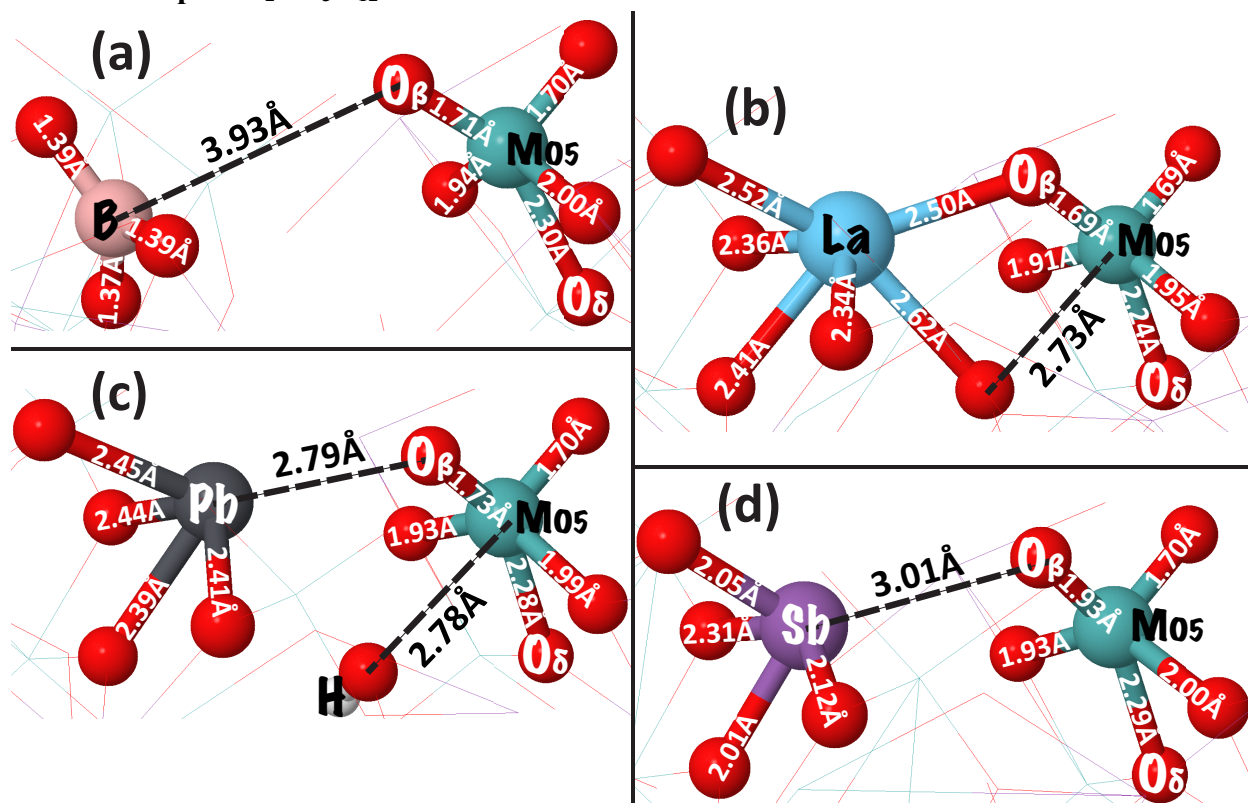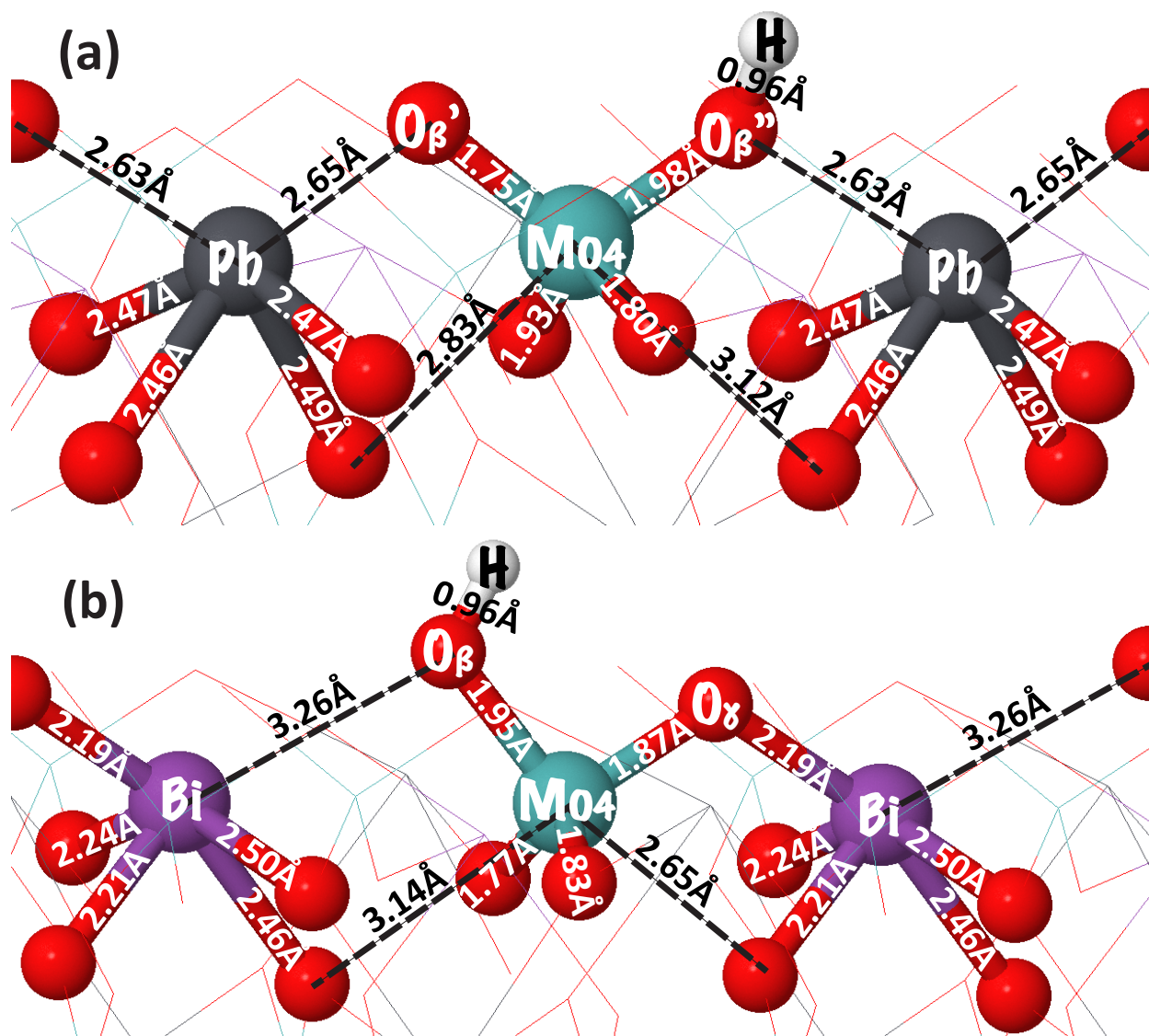
Appendix B

1. Cation doped Bi₂Mo₃O₁₂

Fig. B.1 Structures of cation doped $Bi_2Mo_3O_{12}$, where one surface Bi^{3+} is replaced with (a) B^{3+} (b) La^{3+} (c) Pb^{2+} plus H^+ and (d) Sb^{3+}.
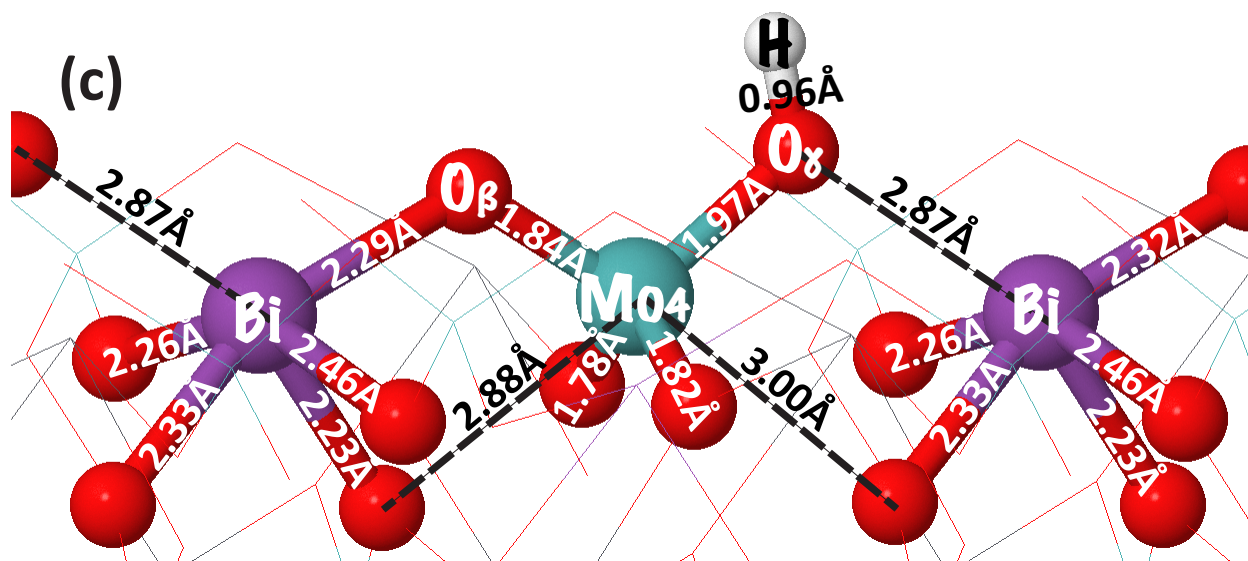
2. Surface hydrogen addition on Bi₂Pb₅Mo₈O₃₂

Fig. B.2 (a) Side view of a Pb row on the surface of $Bi_2Pb_5Mo_8O_{32}$ after hydrogen addition to O_β". (b) Side view of a Bi row after hydrogen addition to O_β. (b) Side view of a Bi row after hydrogen addition to O_γ. Relevant distances in Å are indicated on the bond or with a dashed line between atoms.

Addition of a hydrogen atom to O_β", the other surface oxygen in the Pb row, is not as favorable as addition to O_β'. Though they appear almost equivalent on the oxidized surface, as they are in $PbMoO_4$, the geometric distortion in $Bi_2Pb_5Mo_8O_{12}$ allows Mo to approach much closer to an oxygen trans to where the hydrogen is added when it is added to O_β' than when it is added to O_β".

The second most favorable site for a hydrogen addition to $Bi_2Pb_5Mo_8O_{12}$ is O_β, with an HAE comparable to that of $PbMoO_4$. The distances between Bi, O_β, and Mo are similar to those of the O_β site in $Bi_2Mo_3O_{12}$, but the HAE is almost 15 kcal/mol higher. The biggest difference between the two structures is that, unlike $Bi_2Mo_3O_{12}$, $Bi_2Pb_5Mo_8O_{12}$, has no loosely coordinated oxygen atom trans to the O_β with which the molybdenum can bind when it loses the pi bond to O_β. Even after geometry distortion during optimization, the next closest oxygen atom in the mixed molybdate is 2.65 Å away, which is not close enough to have any significantly coordination with the molybdenum. Finally, hydrogen addition to O_γ of $Bi_2Pb_5Mo_8O_{12}$ is not favorable, with both a geometry and an HAE similar to that of addition to O_γ in $Bi_2Mo_3O_{12}$.

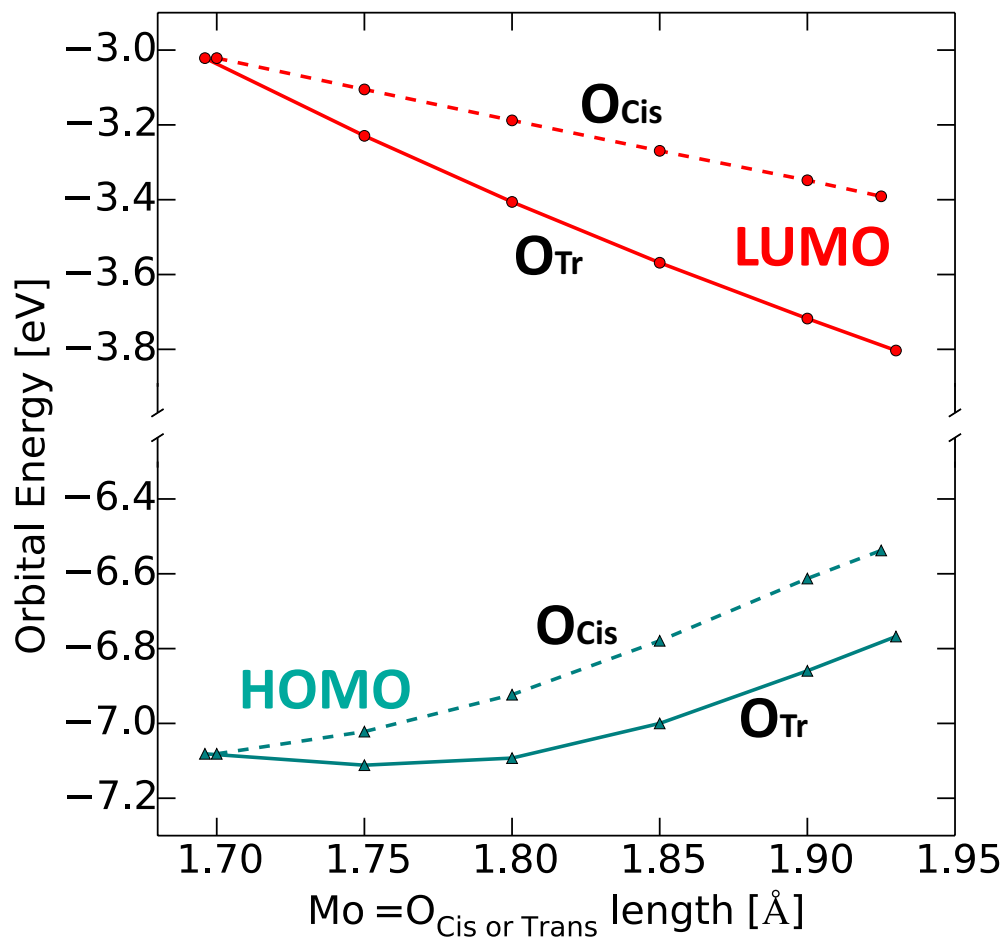## 3. Hydrogen addition to O_{Cis}

Fig. B.3 HOMO and LUMO energies as Mo=O bond length is stretched from its optimized distance before H addition to its optimized distance after H addition for both O_{Tr} (solid curve) and O_{Cis} (dashed curve). Mo-O_δ distance is constrained at 2.392Å and either Mo-O_{Tr} or Mo-O_{Cis} is constrained to the distance plotted, but the atoms are allowed to geometry relax within the side –OH group torsional angle constraint used for all clusters.